Molecular-beam epitaxy growth and structural characterization of semiconductor–ferromagnet heterostructures by grazing incidence x-ray diffraction

DISSERTATION

zur Erlangung des akademischen Grades
doctor rerum naturalium
(Dr. rer. nat.)
im Fach Physik

eingereicht an der
Mathematisch-Naturwissenschaftlichen Fakultät I
Humboldt-Universität zu Berlin

von
Herr M. Tech. M. Sc. Dillip Kumar Satapathy
geboren am 10. 07. 1978 in Nayagarh, Orissa, Indien

Präsident der Humboldt-Universität zu Berlin:
Prof. Dr. Hans Jürgen Prömel (in Vertretung)

Dekan der Mathematisch-Naturwissenschaftlichen Fakultät I:
Prof. Thomas Buckhout, PhD

Gutachter:

1. Prof. Dr. Klaus H. Ploog
2. Prof. Dr. W. T. Masselink
3. Prof. Dr. A. D. Wieck

eingereicht am: 29. September 2005
Tag der mündlichen Prüfung: 19. Dezember 2005

Zusammenfassung

Die Integration von Halbleitern mit ferromagnetischen Metallen ist von Bedeutung für die Entwicklung spinbasierter elektronischer Bauelemente. Diese Arbeit untersucht das Wachstum des Metalls MnAs auf dem Halbleiter GaAs. Die MnAs-Filme werden auf GaAs mittels der Molekularstrahlepitaxie (MBE) abgeschieden. Wir untersuchen die Entwicklung der Gitterfehlanpassung, der Schichtmorphologie und der Grenzflächenstruktur während des Wachstums. Dazu wird *In situ*-Röntgenbeugung unter streifendem Einfall (GID) mit Synchrotronstrahlung in Echtzeit während des Wachstums eingesetzt. Zusätzliche Reflektions-Hochenergieelektronenbeugungs- (RHEED)-Azimutalmessungen werden verwendet, um die Keimbildung an der Grenzfläche zu untersuchen.

Die RHEED-Messungen offenbaren vier unterschiedliche Abschnitte während der Nukleation. Nach einer kohärenten Absorption von Mn-Adatomen für Bedeckungen $\leq 0{,}3$ monolayer (ML) beobachten wir Strukturen, die den Atomabstand zwischen Mn und As im Volumenkristall aufweisen, aber beliebig orientiert sind. Dieser Abstand entspricht weder dem Substrates noch dem des epitaktischen Films. Aus dieser beliebig orientierten Struktur entwickelt sich der epitaktische Film-Substrat Verbund zunächst entlang der $[1\,1\,0]$-Richtung, in der eine stärkere Bindung zwischen Film und Substrat besteht, und dann entlang der orthogonalen $[1\,\bar{1}\,0]$-Richtung bei einer nominellen Bedeckung von 2 ML.

Röntgenbeugung unter streifendem Einfall zeigt, dass das weitere Wachstum der MnAs-Schicht durch die Bildung relaxierter dreidimensionaler Inseln erfolgt, die ab einer nominellen Bedeckung von 2,5 ML an Größe zunehmen und dann zusammenwachsen bis sie einen geschlossenen Film bilden. Sehr früh beginnt sich ein Versetzungsnetzwerk an der Grenzfläche auszubilden. Dieser Prozess ist schon vor dem Schichtschluss praktisch abgeschlossen. Während des Schichtwachstums wachsen die Inseln in zwei Phasen. Bis zum Zusammenwachsen der Schicht bei etwa 20 ML nomineller Schichtdicke beobachten wir eine schnelle Größenzunahme, die danach deutlich schwächer wird. Das komplexe Verhalten der Nukleation von MnAs auf GaAs $(0\,0\,1)$ enthält also Elemente sowohl des Volmer–Weber- als auch des Stranski–Krastanov-Wachstums.

Eine modulierte Gitterfehlanpassung von im Mittel 0,66 % entlang der c-Achse und 0,54 % entlang der a-Achse ergibt sich aus der Analyse von Röntgenbeugungsmessungen entlang der entsprechenden Richtungen. Die Versetzungen sind entlang GaAs $[1\,1\,0]$ stark korreliert und ergeben ein streng periodisches Gitter, während senkrecht dazu entlang GaAs $[1\,\bar{1}\,0]$ die Modulation des Gitterparameters parallel zur Oberfläche sehr schwach ist. Die Periode der Versetzungen in a-Richtung ist $4{,}95 \pm 0{,}05$ nm; tiefenaufgelöste Messungen ergeben eine Lokalisierung an der Grenzfläche. Das periodische Versetzungsnetzwerk relaxiert die Verspannung von 7,5 % entlang der a-Richtung. Die Modulation des Gitterparameters ist auf eine Entfernung von 1,6 nm von der Grenzfläche beschränkt. Die Fehlanpassung entlang der c-Richtung wird durch die Bildung eines Koinzidenzgitters relaxiert. Die Periode dieses Koinzidenzgitters zeigt eine Passung von 4,4 MnAs-Ebenen auf 6,4 GaAs-Ebenen. Es ergibt sich dadurch eine komplexe Mehrfachperiodizität, die hauptsächlich aus einer Periode von 9 Einheitszellen besteht.

Auf GaAs $(1\,1\,3)$A bilden sich bei einer ML MnAs dreidimensionale Inseln. Dieselbe Gitterfehlanpassung von 7,5 % entlang der a-Richtung wird wiederum mittels eines periodischen Versetzungsnetzwerks abgebaut. Im Unterschied zur $(0\,0\,1)$-Oberfläche finden wir aber einen halb so langen Burgers-Vektor und damit die doppelte Versetzungsdichte. Die c-Achse des hexagonalen MnAs ist um 4 ° aus der Grenzfläche gekippt.

Schlagwörter:
Ferromagnet-Halbleiter Hybridstrukturen, Molekularstrahlepitaxie, Dünne Schichten, Beugung unter streifendem Einfall, Beugung hochenergetischer Elektronen, Periodische Versetzungsnetzwerke, Grenzfläche

Abstract

The integration of conventional semiconductors with ferromagnetic metals is important for the development of semiconductor spin based devices. The present work is devoted to the growth of the ferromagnetic metal MnAs on the semiconductor GaAs. The MnAs films are deposited on GaAs by molecular-beam epitaxy (MBE). We investigate the evolution of strain, morphology and interfacial structure during growth. *In situ* grazing incidence diffraction (GID) studies using synchrotron x-rays is carried out in real-time, during the MBE growth. In addition, reflection high-energy electron diffraction (RHEED) azimuthal scans are used to study the nucleation phase.

Four stages of the nucleation process during growth of MnAs on GaAs (0 0 1) are revealed by RHEED azimuthal scans. A coherent adsorption of the Mn adatoms during the early stage of growth [$\leq$ 0.3 monolayer (ML)] is observed. Then, randomly oriented structures with the nearest neighbor distance of MnAs form on the surface with neither the film nor the substrate periodicity. The epitaxial lock-in of the layer takes place out of this disordered phase between 1.1 ML to 2 ML in two steps: first along the [1 1 0] direction, in which there is a strong interaction between film and substrate, then in the orthogonal $[1\,\bar{1}\,0]$ direction at a nominal coverage of 2 ML.

GID shows that further growth of MnAs films proceed via the formation of relaxed islands at a nominal thickness of 2.5 ML which increase in size and finally coalesce to form a continuous film. Early on, an ordered array of misfit dislocations forms at the interface releasing the misfit strain even before complete coalescence occurs. The films are almost completely relaxed during formation. The relaxation process is thermally activated. A two stage coarsening of islands is seen. A fast increase in the island size is observed until the coalescence at about 20 ML, and a slower increase afterwards. The fascinatingly complex nucleation process of MnAs on GaAs (0 0 1) contains elements of both Volmer–Weber and Stranski–Krastanov growth.

A nonuniform strain amounting to 0.66% along the c axis and 0.54% along the a axis is demonstrated from x-ray line profile analysis. A high correlation between the defects is found along the GaAs [1 1 0] direction in comparison to the GaAs $[1\,\bar{1}\,0]$ direction. In accordance with this, an extremely periodic array of misfit dislocations with a period of 4.95±0.05 nm is found at the interface, using depth-tunable GID. The periodic array of dislocations release the misfit of 7.5% along the a direction. The inhomogeneous strain due to the periodic dislocations is confined at the interface within a layer of 1.6 nm thickness. The misfit along the c direction is released by the formation of a coincidence site lattice. A basic periodicity of the coincidence site lattice with a non-integer plane match of 4.4 MnAs planes to 6.4 GaAs planes is found at the interface along the c direction. In addition to this, a superperiod of 9 basic units exists at the interface along the c direction.

The MnAs layers grow on GaAs (1 1 3)A surface via the formation of three-dimensional islands at 1 ML coverage. The same mismatch of 7.5% along the a direction is released again by periodic misfit dislocations, but with a two times smaller Burgers vector and two times smaller spacing, compared to MnAs/GaAs (0 0 1). The c axis of the hexagonal unit cell is tilted by 4° along the growth direction.

Keywords:
Ferromagnet-semiconductor hybrid structures, Molecular beam epitaxy, Thin films, Grazing incidence diffraction, Relfection high-energy electron diffraction, Periodic dislocation array, Interface

Parts of this work have already been published

D. K. Satapathy, B. Jenichen, V. M. Kaganer, W. Braun, L. Däweritz, and K. H. Ploog '*In-situ investigation of MnAs/GaAs (0 0 1) growth and interface structure using synchrotron x-ray diffraction*', J. Vac. Sci. Technol. B. **22**, 2079 (2004).

D. K. Satapathy, B. Jenichen, W. Braun, V. M. Kaganer, L. Däweritz, K. H. Ploog '*In situ grazing incidence x-ray diffraction study of strain evolution during growth and postgrowth annealing of MnAs on GaAs (1 1 3)A*', J. Phys. D: Appl. Phys. **38**, A164 (2005).

D. K. Satapathy, V. M. Kaganer, B. Jenichen W. Braun, L. Däweritz, K. H. Ploog '*Periodic array of misfit dislocations at the MnAs/GaAs interface studied by synchrotron x-ray diffraction*', Phys. Rev. B **72**, 155303 (2005).

B. Jenichen, **D. Satapathy**, W. Braun, L. Däweritz, K. H. Ploog '*Microstructure of epitaxial MnAs films on GaAs(001) during and after the growth*', J. Appl. Phys. **96**, 6103 (2004).

B. Jenichen, **D. K. Satapathy**, W. Braun, V. M. Kaganer, L. Däweritz, and K. H. Ploog '*Structural properties of MnAs epitaxial layers on GaAs: an in situ x-ray study*', J. Phys. D: Appl. Phys. **38**, A169 (2005).

Parts of this work have either been submitted or are in preparation

Wolfgang Braun, **D. K. Satapathy**, Klaus H. Ploog '*Initial stages of MnAs/GaAs (0 0 1) epitaxy studied by RHEED azimuthal scans*' (Submitted to Surf. Sci.).

D. K. Satapathy, W. Braun, B. Jenichen, K. H. Ploog '*Reflection High energy electron diffraction and x-ray diffraction investigation of the interface structure of MnAs on GaAs (0 0 1)*' (in preparation).

V. M. Kaganar, **D. K. Satapathy**, B. Jenichen, W. Braun, K. H. Ploog '*Incommensurate heterointerface between MnAs/GaAs (0 0 1) studied by grazing incidence x-ray diffraction* ' (in preparation).

Conference Contributions

D. K. Satapathy, V. M. Kaganer, W. Braun, B. Jenichen, K. H. Ploog '*Surface and Interface of MnAs/GaAs (0 0 1) epitaxial films studied by grazing-incidence x-ray diffraction*' 8th International Conference on the Structure of surfaces, Munich, Germany 18-22 July 2005.

D. K. Satapathy, B. Jenichen, W. Braun, V. M. Kaganer, L. Daweritz, K. H. Ploog '*Interface configuration during extreme heteroepitaxy of MnAs on GaAs*' 23rd users meeting of Berliner Elektronenspeicherring-Gesellschaft für Synchrotronstrahlung (BESSY II), Berlin, Germany, December 2-3, 2004.

B. Jenichen, **D. K. Satapathy**, W. Braun, V. M. Kaganer, L. Daweritz, and K. H. Ploog '*Microstructure of MnAs epitaxial films: an in situ x-ray study*' German crystallographers union meeting, Freiburg, Germany, Dec 1-3, 2004.

D. K. Satapathy, B. Jenichen, W. Braun, V. M. Kaganer, L. Däweritz, K. H. Ploog '*MnAs on GaAs: Growth and strain evolution during the early stages of molecular-beam epitaxy growth*' 7th Biennial Conference on High Resolution X-ray Diffraction and Imaging, Pruhonice near Prague, Czech Republic, September 7-10, 2004.

B. Jenichen, **D. K. Satapathy**, W. Braun, V. M. Kaganer, L. Däweritz, and K. H. Ploog '*Structural properties of MnAs epitaxial layers on GaAs*' 7th Biennial Conference on High Resolution X-ray Diffraction and Imaging Pruhonice near Prague, Czech Republic, September 7-10, 2004.

B. Jenichen, **D. K. Satapathy**, V. M. Kaganer, W. Braun L. Däweritz, and K. H. Ploog '*In-situ Röntgenuntersuchun zur Extremen Heteroepitaxie von MnAs auf GaAs*' 12th Annual meeting of the German Union of Crystallography, Jena, Germany, March 15-19, 2004.

D. K. Satapathy, B. Jenichen, V. M. Kaganer, W. Braun, L. Däweritz, and K. H. Ploog '*In-situ investigation of MnAs/GaAs (0 0 1) growth and interface structure using synchrotron x-ray diffraction*' 31st Conference on The Physics and Chemistry of Semiconductor Interfaces, Kailua-kona, Hawaii, January 18-22, 2004.

D. K. Satapathy, W. Braun, B. Jenichen, V. M. Kaganer, X. Guo, S. Behnke, L. Däweritz, K. H. Ploog '*Growth and Interface of MnAs/GaAs (0 0 1): An in-situ grazing incidence x-ray diffraction study*' 22nd users meeting of Berliner Elektronenspeicherring-Gesellschaft für Synchrotronstrahlung (BESSY II), Berlin, Germany, December 4-5, 2003.

B. Jenichen, V. Kaganer, W. Braun, **D. K. Satapathy**, X. Guo, L. Däweritz, K. H. Ploog '*Structural Characterization of thin MnAs Epitaxial layers on GaAs by Grazing Incidence x-ray diffraction*' 10th International Conference on Defects, DRIP X, Batz-sur-Mer, France, September 29-October 2, 2003.

List of Acronyms

AFM	Atomic Force Microscopy
CCD	Charge Coupled Device
CSL	Coincidence Site Lattice
CTR	Crystal Truncation Rod
FWHM	Full Width at Half Maximum
GID	Grazing Incidence Diffraction
LEED	Low Energy Electron Diffraction
MBE	Molecular-Beam Epitaxy
ML	Monolayer
nm	Nanometer
RHEED	Reflection High-Energy Electron Diffraction
SP	Specular Plane
SQUID	Superconducting QUantum Interface Device
STM	Scanning Tunneling Microscopy
TEM	Transmission Electron Microscopy
HRTEM	High-Resolution Transmission Electron Microscopy
XRD	X-Ray Diffraction
XRR	X-Ray Reflectivity
2D	Two-dimensional
3D	Three-dimensional

Contents

Chapter 1

Introduction

One of the most exciting and useful developments in modern semiconductor electronics is the capability of engineering the band structure to produce heterostructures with novel electronic and optical properties. With the advent of advanced semiconductor growth techniques, such as molecular-beam epitaxy (MBE), much of modern compound semiconductor device development now involves semiconductor heterostructures with precise heterojunctions that combine a variety of materials. This enhanced understanding and control of quantum mechanical phenomena has led to important discoveries in condensed matter physics such as the integer and the fractional quantum Hall effects, and useful quantum devices such as quantum well lasers and high mobility transistors. On a parallel but separate track, the study of magnetic heterostructures, such as spin valves and magnetic tunnel junctions, is interesting from both theoretical and technological perspectives. Recently, the idea to combine the charge and the spin degree of freedom of electrons in a single device has spawned a new field of semiconductor spin electronics (or semiconductor spintronics) [1, 2, 3]. In order to utilize the spin degree of freedom in semiconductors, one of the first step is to develop efficient sources for spin-polarized electrons. It is widely recognized that the combination between a ferromagnetic material and a semiconductor, especially one having a large carrier spin polarization and a Curie temperature (T_c) above room temperature, may provide a rich playground for the discovery of new physical phenomena, and potentially serve as a source of spin polarized electrons [4]. This has lead to investigations of a variety of heterostructures that combine semiconductors with magnetic materials. These include paramagnetic, antiferromagnetic and ferromagnetic metal–semiconductor heterostructures. Here we focus on the MBE growth and structural characterization of heterostructures derived from a conventional III-V semiconductor (GaAs) and a ferromagnetic metal (MnAs). Electrical spin injection in MnAs/GaAs heterostructures [5] and high spin polarization of MnAs have already been demonstrated [6].

MnAs is structurally dissimilar to the III-V semiconductors in terms of its lattice parameter, crystal structure, bonding character, and thermal expansion coefficients. The heteroepitaxial growth of such a system induces a competition between anisotropic strain and defect formation. As the strain energy builds up with increasing thickness, defect formation becomes energetically more favorable, which relieves most of the built-in strain. The process of strain accumulation and its relaxation at the interface during heteroepitaxy affects the structural and the electronic properties of the layer. Moreover, the strain field at the interface may scatter and relax the spin of the electrons [7]. Hence, it is important to understand the epitaxial growth mechanisms, the strain evolution, and its distribution in the interface plane. MnAs film on GaAs substrate undergoes two structural and magnetic phase transitions while cooling from growth temperature to room temperature. Therefore, to have a clear understanding of the aforementioned phenomena an *in situ* study during growth is necessary. Although the epitaxial growth of MnAs on III-Vs has been reported a decade ago [8], and reviewed recently [9], these issues are still not fully understood. From a fundamental point of view, the understanding of epitaxial growth and interface structure of dissimilar materials is still at an early stage.

The above mentioned topics have already outlined the objectives of the present work. We are studying the epitaxial growth kinetics, the evolution of strain, the process of formation and the structure of the interface of MnAs/GaAs heterostructures. In addition to this, the effect of thermal annealing on the heterointerface is investigated. Grazing incidence x-ray diffraction (GID), and reflection high-energy electron diffraction (RHEED) are employed in this study. The measurements are performed *in situ* and in real-time during the epitaxy of MnAs on GaAs substrates. A combination of an MBE chamber and a six-circle x-ray diffractometer installed at the PHARAO beamline at BESSY (Germany) is used for the experiments.

The use of x-ray scattering to study surfaces and interfaces has been made possible by the advent of high brilliance synchrotron radiation. The scattering probe as opposed to imaging (TEM and STM) is an *indirect* method and requires careful analysis to obtain the desired information. Nevertheless, it has the advantage that it is usually nondestructive, and provides us with global statistical information about the surface or the interface and is thus ideal for studying collective behavior.

This thesis is organized as follows. A brief summary of the most important properties of GID and an introduction to the experimental techniques is given in Chapter 2. The GID study of the epitaxial growth process, its strain evolution, and the different epitaxial orientations of MnAs on GaAs (0 0 1) are discussed in Chapter 3. A detailed RHEED study reveals four different stages of growth before the epitaxial lock-in is established. The magnetic properties of ultrathin MnAs layers on GaAs (0 0 1) are discussed. The microstructure and evolution of the mosaicity during the growth of MnAs on GaAs (0 0 1) are presented in Chapter 4. Most interestingly, the twist of the MnAs islands about the surface normal decreases exponentially with increasing thickness. The interface structure of MnAs/GaAs (0 0 1) heterostructure measured by depth-tunable GID and the effect of thermal annealing on the interface structure is discussed in Chapter 5. An extremely periodic array of misfit dislocations is found along the GaAs [1 1 0] direction. The epitaxial growth, effect of thermal annealing, interface structure, and the magnetic properties of MnAs/GaAs (1 1 3)A heterostructures are discussed in Chapter 6.

Chapter 2

X-ray diffraction and experimental techniques

2.1 X-ray diffraction

X-ray diffraction (XRD) is the most important non-invasive tool for studying structural properties of matter ranging from amorphous to crystalline, since the wavelength of x-rays is comparable to interatomic distances (~ 1Å). In addition to applications in material science, x-ray diffraction is used in a variety of fields from identifying unknown materials in geology to solving the structures of large protein molecules in biology. In recent years, due to the advent of brilliant synchrotron sources, it is possible to get measurable diffraction intensity from less than one monolayer of material, which makes x-ray diffraction a surface sensitive probe. This has opened the door to a new field called surface x-ray diffraction.

X-rays interact weakly with matter. As a result multiple scattering effects can often be neglected (unlike, for example, in electron diffraction). Hence, in most of the cases, a simple quantitative analysis based on a single scattering (kinematic) approximation is possible. X-rays penetrate significant distances into the sample because of the weak interaction with matter. The tunable penetration depth of x-rays between several nanometer (nm) and several hundreds of nanometer allows a nondestructive investigation of both buried structures and surfaces. By choosing the proper scattering geometry, one can tune the penetration depth so that information is obtained either from the surface or the bulk.

According to the classical theory, the x-radiation has an electric field vector that is oscillating rapidly. If an x-ray beam is directed at a row of equally spaced atoms, then the electrons of these atoms are subjected to this field, and they experience a corresponding force and acceleration. In fact, each atom gets polarized and behaves like an oscillating dipole. These oscillating dipoles radiate both at the same frequency (elastic scattering) and at smaller frequencies (Compton modified scattering) in all possible directions [10]. The Compton scattering contributes to a diffuse background which is incoherent. The elastically scattered x-rays from a periodic array of atoms spread spherically and reinforce (constructively interfere) in certain directions to produce the zero, first, second, and higher order diffracted beams, whereas they destructively interfere along all the other directions. This analysis was first introduced by Bragg in the year 1905.

The row of atoms shown in Fig. 2.1 (a) has infinite rotational symmetry along the axes passing through it. Therefore in three dimensions the reinforcement directions of different order can be represented by the cones as demonstrated in the Fig. 2.1 (a). Similarly, for a

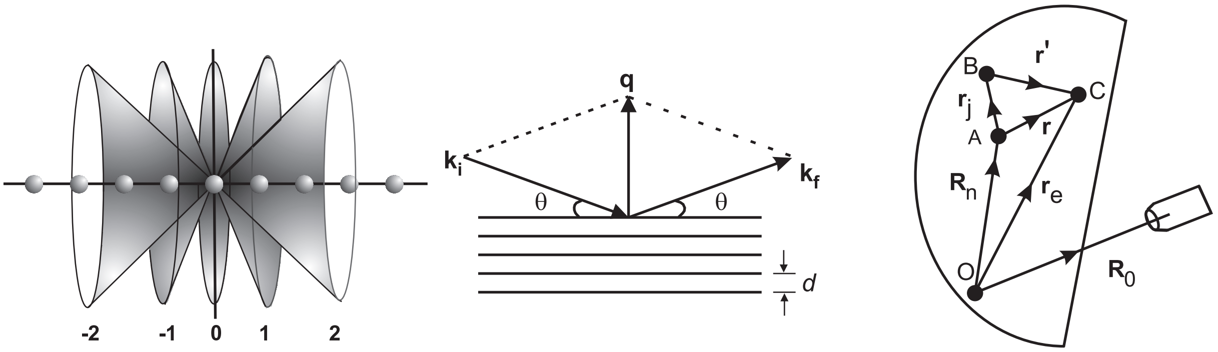

(a) (b) (c)

Figure 2.1: Schematic representation of all possible reinforcement directions of the scattered wave of different order from a one-dimensional row of atoms, where reinforcement can occur according to Bragg's law. Due to the infinite rotational symmetry of an atom, all possible directions are represented by cones. (b) Symmetric scattering geometry showing the relationship between the scattering vector $\mathbf{q}$ and the incident and outgoing $\mathbf{k}$-vectors when diffraction is occurring from planes having a spacing d. (c) Real space vectors discussed in the text are defined in the schematic. The point O is defined as the origin of the crystal, A is the origin of the $\mathrm{n^{th}}$ unit cell, B is the $\mathrm{j^{th}}$ atom of the $\mathrm{n^{th}}$ cell and C is an electron belonging to the $\mathrm{j^{th}}$ atom of the $\mathrm{n^{th}}$ cell.

two-dimensional array of equally spaced atoms the reinforcement directions of scattered waves are defined by the intersection two sets of corresponding cones oriented along the two coordinate axes.

The Bragg formulation for diffraction from periodic structures (crystals) is, in the kinematic limit, given by [11]

$$\lambda = 2\, d\, \sin\theta, \tag{2.1}$$

where θ is the Bragg reinforcement angle for incident x-rays with wavelength λ scattering off a material with a periodicity d shown in Fig. 2.1 (b).

2.1.1 Scattering of x-rays from a crystal

X-rays are mostly diffracted by the electrons in a material. Conversely, x-ray scattering from an electron is roughly three orders of magnitude greater than the scattering from a nucleus. Nuclear x-ray scattering can therefore be neglected. For a clear-cut understanding of the diffraction of x-rays from a crystal, it is useful to start from the basics of electromagnetic radiation scattering from an atom and construct an expression for the scattered intensity from the entire crystal.

Consider a crystal having the origin at O as shown in Fig. 2.1 (c). The origin of the $\mathrm{n^{th}}$ unit cell is at A, B is the $\mathrm{j^{th}}$ atom of the $\mathrm{n^{th}}$ cell and C is an electron belonging to the $\mathrm{j^{th}}$atom of the $\mathrm{n^{th}}$ cell. Within the dipole approximation the scattered amplitude from a single electron is described in terms of the incoming amplitude by the Thompson formula [11],

$$A_e\, e^{-i\, \mathbf{k_f} .\, \mathbf{r_e}} = \frac{e^2}{mc^2 R} A_0\, e^{-i\, \mathbf{k_i}\, .\, \mathbf{r_e}}\,, \tag{2.2}$$

where A_0 and A_e are the incident and scattered amplitudes, respectively. $|\mathbf{k_i}| = |\mathbf{k_f}| = 2\pi/\lambda$ are the incoming and outgoing wave vectors. $\mathbf{r_e}$ is the distance of the electron from the origin of the crystal as shown in Fig. 2.1 (c). The mass and charge of the electrons are given by m and e, c is the velocity of light and R is the distance of the measuring point (position of detector) from the scattering source. Although in reality the scattering occurs from a large number of electrons in a crystal the kinematic approximation is still valid because the ratio e^2/mc^2 is very small (3×10^{-15}). The scattered amplitude is given by:

$$A_e = A_0 \frac{e^2}{mc^2R}\, e^{i\,\mathbf{q}\,\cdot\,\mathbf{r_e}}\,, \tag{2.3}$$

where $\mathbf{q} = \mathbf{k_f} - \mathbf{k_i}$ is the scattering vector. It is defined as the difference between the outgoing and the incoming wave vector and represents the momentum transfer during scattering. The scattering of x-rays from a set of planes is schematically shown in Fig. 2.1 (b). Since the magnitude of the wave vector is $2\pi/\lambda$, the diffraction condition can be written as,

$$|q| = 2|k| \sin\frac{\theta}{2} = \frac{4\pi\,\sin\theta}{\lambda} = \frac{2\pi}{d}\,. \tag{2.4}$$

Hence, if the length of the scattering vector is equal to the inverse of the d spacing probed, then Bragg diffraction will occur. The scattering amplitude due to a single atom at the detector can be calculated by performing the volume integral of Eq. 2.3 over the electron density $\rho(\mathbf{r'})$ of the atom volume $d^3\mathbf{r'}$,

$$\begin{aligned} A_{atom} &= A_0 \frac{e^2}{mc^2R} \int_{-\infty}^{+\infty} \rho(\mathbf{r'})\, e^{\,i\,\mathbf{q}\,.\,(\mathbf{R_n} + \mathbf{r_j} + \mathbf{r'})}\, d^3\mathbf{r'} \\ &= A_0 \frac{e^2}{mc^2R}\, f(q)\, e^{i\,\mathbf{q}\,.\,(\mathbf{R_n} + \mathbf{r_j})}\,, \end{aligned} \tag{2.5}$$

where $f(q) = \int \rho(\mathbf{r'})\, e^{i\,\mathbf{q}\,\cdot\,\mathbf{r'}} d^3\mathbf{r'}$ is the atomic form factor. This is equivalent to the Fourier transform of the electron density for a single atom. $\mathbf{R}_n$ is the distance between the origin of the crystal and that of the n$^{\text{th}}$ unit cell. Since in almost all cases atoms are considered to be spherical, the atomic form factor is independent of direction, and $f(q)$ is written purely as a function of the magnitude of the momentum transfer.

To calculate the scattering amplitude due to one unit cell of the crystal let us assign separate form factors $f_j(q)$ to different atomic sites. The scattering amplitude for a unit cell containing N atoms is then given by:

$$\begin{aligned} A_{unit\,cell} &= A_0 \frac{e^2}{mc^2R} \sum_{j=1}^{N} f_j(q)\, e^{\,i\,\mathbf{q}\,.\,(\mathbf{R_n} + \mathbf{r_j})} \\ &= A_0 \frac{e^2}{mc^2R} F(\mathbf{q})\, e^{\,i\,\mathbf{q}\,.\,(\mathbf{R_n})}\,. \end{aligned} \tag{2.6}$$

Where $F(\mathbf{q})$ is the structure factor, which is expressed as a function of the atomic positions $\mathbf{r_j}$ within the unit cell,

$$F(\mathbf{q}) = \sum_{j=1}^{N} f_j(q)\, e^{\,i\,\mathbf{q}\,\cdot\,\mathbf{r_j}}\,. \tag{2.7}$$

Let us now calculate the scattered intensity due to the entire crystal which consists of N_1, N_2, N_3 unit cells along the three crystal axes. These axes are defined by the real space vectors $\mathbf{a_1}, \mathbf{a_2}, \mathbf{a_3}$ and are connected to the corresponding reciprocal lattice vectors $\mathbf{b_1}, \mathbf{b_2}, \mathbf{b_3}$ through the relations,

$$\mathbf{b_1} = 2\pi \frac{\mathbf{a_2} \times \mathbf{a_3}}{\mathbf{a_1} \, . \, (\mathbf{a_2} \times \mathbf{a_3})}, \quad \mathbf{b_2} = 2\pi \frac{\mathbf{a_3} \times \mathbf{a_1}}{\mathbf{a_1} \, . \, (\mathbf{a_2} \times \mathbf{a_3})}, \quad \mathbf{b_3} = 2\pi \frac{\mathbf{a_1} \times \mathbf{a_2}}{\mathbf{a_1} \, . \, (\mathbf{a_2} \times \mathbf{a_3})} \, . \tag{2.8}$$

The total amplitude scattered by the whole crystal is obtained by the summing over the unit cells of the crystals Eq. 2.6 [12],

$$A_s(q) = A_0 \, \frac{e^2}{mc^2 R} \, F(\mathbf{q}) \sum_{n_1=0}^{N_1-1} \sum_{n_2=0}^{N_2-1} \sum_{n_3=0}^{N_3-1} e^{\, i \, \mathbf{q} \, . (n_1 \mathbf{a_1} + n_2 \mathbf{a_2} + n_3 \mathbf{a_3})} \, . \tag{2.9}$$

Each of the three sums in Eq. 2.9 evaluates to

$$S_{N_j}(\mathbf{q} \, . \, \mathbf{a_j}) = \sum_{n_j=0}^{N_j-1} e^{\, i \, \mathbf{q} \, . n_j \mathbf{a_j}} = \frac{\exp(i\mathbf{q} \, . \, a_j N_j) - 1}{\exp(i\mathbf{q} \, . \, a_j) - 1} \, , \qquad j = 1, 2, 3 \, . \tag{2.10}$$

Since in x-ray diffraction, intensity (not the amplitude) is the measurable quantity, we have to take the square of the amplitude to obtain the diffracted intensity,

$$|S_{N_j}(\mathbf{q} \, . \, \mathbf{a_j})|^2 = \frac{\sin^2(N_j \mathbf{q} \, . \, a_j/2)}{\sin^2(\mathbf{q} \, . \, a_j/2)}, \qquad j = 1, 2, 3 \, . \tag{2.11}$$

This quantity is the well known interference slit function of N_j diffracting units. In the limit of large N, the S_N function tends to a periodic array of Dirac delta functions with a spacing of $2\pi/a$. The scattered intensity from the whole crystal is given by

$$I_s(\mathbf{q}) = A_0^2 \, \frac{e^4}{m^2 c^4 R^2} \, |F(\mathbf{q})|^2 |S_{N_1}(\mathbf{q} \, . \, \mathbf{a_1})|^2 \; |S_{N_2}(\mathbf{q} \, . \, \mathbf{a_2})|^2 \; |S_{N_3}(\mathbf{q} \, . \, \mathbf{a_3})|^2 \, . \tag{2.12}$$

The intensity is very sharply peaked when the denominator approaches to zero, i.e. $\mathbf{q} \, . \, \mathbf{a_1} = 2\pi h, \quad \mathbf{q} \, . \, \mathbf{a_2} = 2\pi k, \quad \mathbf{q} \, . \, \mathbf{a_3} = 2\pi l$ with h, k, l integers. These are called the Laue conditions of diffraction. In other words, the intensity is nonzero only if q is a integral multiple of the reciprocal lattice vectors, $\mathbf{q} = h\mathbf{b_1} + k\mathbf{b_2} + l\mathbf{b_3}$. Therefore, when the Laue conditions are fulfilled, the intensity is given by

$$I_{hkl} = \left| A_0 \, \frac{e^2}{mc^2 R} \, F(\mathbf{q}) \, N_1 \, N_2 \, N_3 \right|^2 \, . \tag{2.13}$$

Here, the structure factor is defined as,

$$F_{hkl}(\mathbf{q}) = \sum_{\text{j unit cell}} f_j(q) \exp[2\pi(hx_j + ky_j + lz_j)] \exp[-M_j] \, . \tag{2.14}$$

The sum is over all the atoms of the unit cell. M_j, x_j, y_j, z_j are the Debye-Waller factor, and fractional coordinates within the unit cell, respectively.

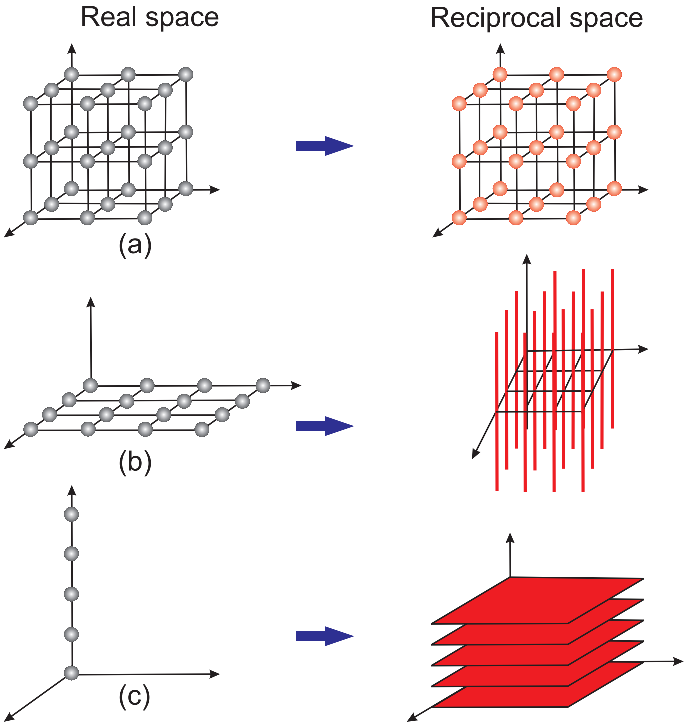

Figure 2.2: Diffraction pattern from an ideal (a) three-dimensional (b) two-dimensional (c) one-dimensional system. The distribution of intensity in reciprocal space is shown.

2.1.2 Crystal truncation rods

In the last section, we have assumed that the crystal is infinite in extent and the diffraction peaks are perfect δ functions. The diffracted intensity is confined at a point in reciprocal space as shown in Fig. 2.2 (a). However, if a two-dimensional (2D) crystal of one monolayer thickness is considered, the diffraction can be described by setting $N_3 = 1$, in Eq. 2.12. The intensity is then expressed by,

$$I_{hkl}^{2D} = \left| A_0 \, \frac{e^2}{mc^2 R} \, F(\mathbf{q}) \, N_1 \, N_2 \right|^2 . \tag{2.15}$$

The diffraction remains sharply peaked in the directions parallel to the surface, but is now independent of the $\mathbf{q} \, . \, \mathbf{a_3}$ term. Thus in three-dimensional (3D) reciprocal space, the diffraction pattern consists of a 2D lattice of rods which are sharp in both directions parallel to the surface and continuous in the direction perpendicular to the surface as shown in Fig. 2.2 (b). These rods are called "crystal truncation rod (CTR)" because they arise from the truncation of the crystal [13].

The real crystal truncated by an abrupt surface can be described by the infinite lattice multiplied by a step function describing the electron density variation as a function of z, the coordinate perpendicular to the surface [14]. Therefore, the diffraction pattern will be a superposition of the diffraction pattern from the bulk (Bragg peaks like δ functions) and diffraction rods from the 2D surface connecting these Bragg peaks. The intensity profile along these rods can be calculated by considering Eq. 2.11. Here the numerator varies rapidly with q, and always remains positive. Thus the intensity profile along the

CTR is given by

$$I_{hkl}^{CTR} = \left| A_0 \, \frac{e^2}{mc^2 R} \, F(\mathbf{q}) \, N_1 \, N_2 \right|^2 \times \frac{1}{2\sin^2(\mathbf{q} \, . \, \mathbf{a_3}/2)} \, . \tag{2.16}$$

The Bragg peak occurs when $\mathbf{q} \, . \, \mathbf{a_3} = 2\pi l$, with an integer value of l. For half-integer values of l, when successive planes scatter out of phase, there remains some intensity in between the Bragg peaks. At this valley between the two Bragg peaks, the I_{hkl}^{CTR} and I_{hkl}^{2D} have comparable magnitude of intensity, i.e. the intensity scattered by a semi-infinite lattice is of the order of the intensity scattered by a single monolayer. The modulation of intensity along the rod between the Bragg peak and valley (as function of l) is related to the z coordinate of the atoms within the unit cell of the 2D layer. In general, the intensity modulation period along the CTR gives the thickness of the distorted layer and the modulation amplitude is related to the normal atomic displacement. The thickness of the layer with inhomogeneous strains at the interface is calculated from the CTR intensity modulation in chapter 5.

2.2 Grazing incidence diffraction

Grazing incidence diffraction of x-rays is a special technique which combines diffraction at lattice planes perpendicular to the sample surface with the total external reflection of the incoming beam from the surface [12, 15, 16]. In this diffraction scheme, grazing incidence and/or grazing exit angles are used to enhance the surface sensitivity. The refractive index (n) for x-rays is given by,

$$n = 1 - \delta + i\beta, \tag{2.17}$$

where $2\delta = \sin^2 \alpha_c$ and $\beta = \mu\lambda/4\pi$, α_c is the critical angle for total external reflection and μ is the linear absorption coefficient. Typical magnitudes are $\delta \sim 10^{-5}$ and $\beta \sim 10^{-6}$, therefore, for most materials n is slightly less than unity. Hence, total external reflection of x-rays from a surface is possible if the incident angle (α_i) is small enough (typically

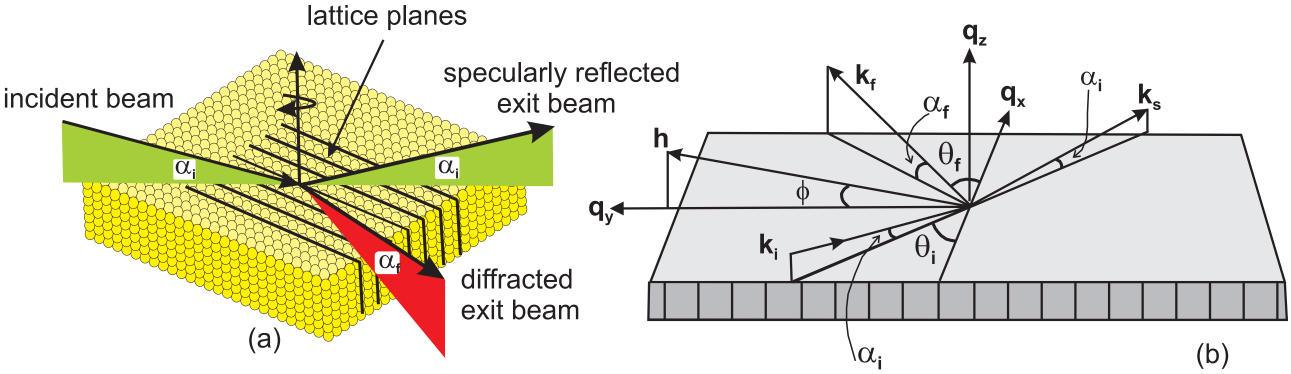

Figure 2.3: Grazing incidence diffraction geometry. All notations used in the figure are described in the text. The diffracting planes are perpendicular to the surface normal.

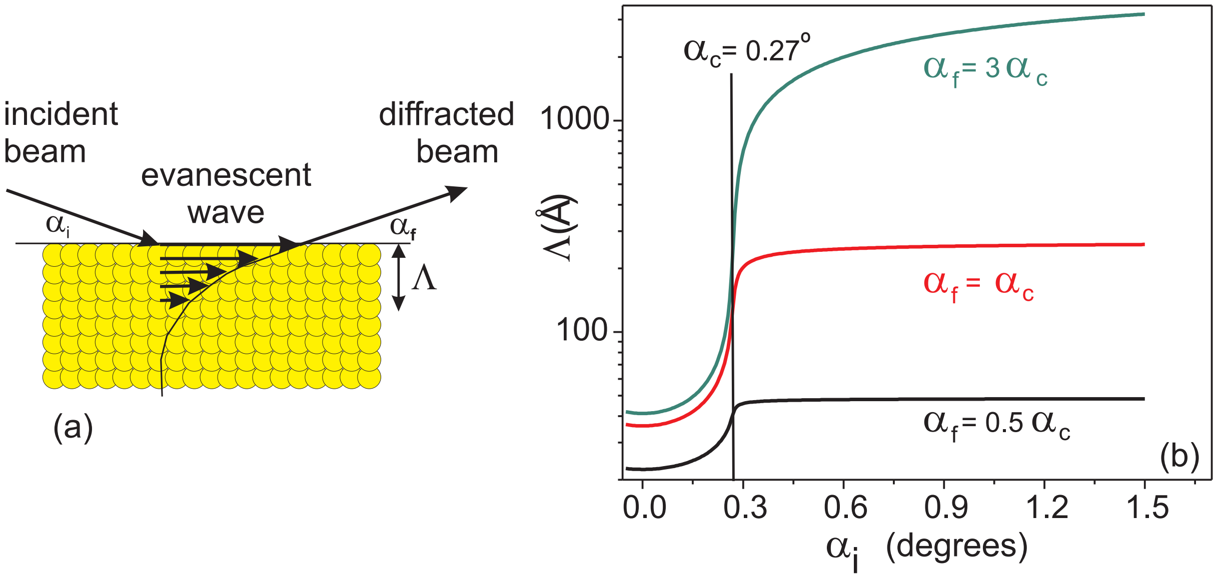

Figure 2.4: (a) Schematic representation of the rapidly vanishing evanescent wave inside the sample travelling in the $(\mathbf{q_x}, \mathbf{q_y})$ plane for the incidence angle α_i less than the critical angle α_c. (b) Variation of the penetration depth Λ as a function of the incidence angle for three different exit angles, equal to $1/2\alpha_c, \alpha_c, 3\alpha_c$, for 10 keV x-rays diffracting from MnAs.

0.05-0.5°, depending on the electron density of the sample). When α_i is less than α_c, the beam is totally reflected and only the rapidly decaying evanescent wave is present below the surface. For α_i larger than α_c the transmitted wave propagates into the sample.

The scattering geometry is shown in Figs. 2.3 (a, b). The x-ray beam with wave vector $\mathbf{k_i}$ is incident at glancing incidence angle α_i with respect to the surface and produces a specularly reflected beam $\mathbf{k_s}$. The Bragg diffraction condition for the planes perpendicular to the surface can be achieved by rotating the sample around the surface normal as shown in Fig. 2.3 (a). The scattered beam of wave vector $\mathbf{k_f}$ is detected at an angle α_f with respect to the sample surface. One might think that the diffracted wave should be directed inside the sample with a small angle, because there is no momentum transfer perpendicular to the surface (the diffraction vector is parallel to the surface). But the diffracted wave experiences the refraction and comes out of the crystal. The momentum transfer is defined by $\mathbf{q} = \mathbf{k_f} - \mathbf{k_i}$. The magnitude of momentum transfer in different directions in reciprocal space is given by,

$$\begin{aligned} q_x &= \frac{2\pi}{\lambda}(\cos\alpha_f \cos\theta_f - \cos\alpha_i \cos\theta_i), \\ q_y &= \frac{2\pi}{\lambda}(\cos\alpha_f \sin\theta_f - \cos\alpha_i \sin\theta_i), \\ q_z &= \frac{2\pi}{\lambda}(\sin\alpha_f + \sin\alpha_i)\,. \end{aligned}$$

As shown in the Fig. 2.3 (b), q_x, q_y are the parallel, and q_z the perpendicular momentum transfer with respect to the surface and commonly known as $\mathbf{q}_{\|}$ and $\mathbf{q}_{\perp}$, respectively. For a very small value of α_i and α_f the momentum transfer $\mathbf{q}$ is almost equal to $\mathbf{q}_{\|}$ and the scattering plane is nearly parallel to the surface. In a grazing incidence diffraction scheme, it is not practical to go to $\mathbf{q}_{\perp} = 0$, because this would require the incident and diffracted

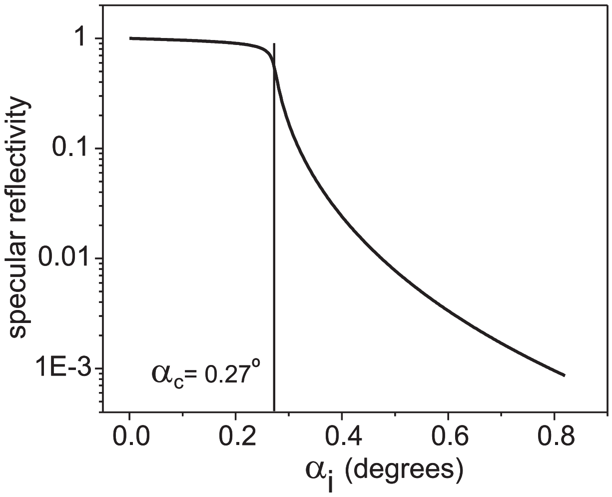

Figure 2.5: The calculated specular reflectivity curve for a MnAs surface as a function of incidence angle. The beam is almost totally reflected below the critical angle. The x-ray is energy 10 keV.

beams to be completely parallel to the surface. However, for thin films the reciprocal lattice is in the form of rods (as discussed in previous section), so the diffraction peaks can just as easily be located at slightly non-zero $\mathbf{q}_\perp$. Therefore, in practice, all in-plane reflections are measured at a value of $\mathbf{q}_\perp$ close to zero.

Penetration depth Since the refractive index of x-rays inside matter is less than 1, the perpendicular components of incident and emergent wave vectors are modified upon crossing the surface because of refraction and absorption [16, 17]. The perpendicular momentum transfer within the sample is given by,

$$\mathbf{q}'_\perp = \mathbf{k}'_{\mathbf{f}\perp} - \mathbf{k}'_{\mathbf{i}\perp} = \frac{2\pi}{\lambda}\left[\sqrt{\sin^2\alpha_f - 2\delta - 2i\beta} + \sqrt{\sin\alpha_i^2 - 2\delta - 2i\beta}\,\right]. \tag{2.18}$$

For a small angle $\alpha_{i,f} < \alpha_c$ the $\mathbf{q}'_\perp$ inside the sample becomes complex, the incoming wave becomes evanescent and propagates in the $(\mathbf{q_x}, \mathbf{q_y})$ plane as shown schematically in Fig. 2.4 (a). The penetration depth Λ is defined as the depth at which the intensity drops to $1/e$ times the original intensity.

$$\Lambda = \frac{1}{Im\,(q_\perp)} = \frac{\lambda}{2\pi(l_i + l_f)}, \tag{2.19}$$

where $l_{i,f}$ is given by

$$l_{i,f} = \frac{1}{\sqrt{2}}\left[\sqrt{(\sin^2\alpha_{i,f} - \sin^2\alpha_c)^2 + 4\beta^2} + \sin^2\alpha_c - \sin^2\alpha_{i,f}\right]^{1/2}. \tag{2.20}$$

The grazing incidence and exit angles thus allow us to tune the probing depth of the sample, which can be varied between ~1 to few hundred nanometer. The penetration depth is proportional to $1/(\alpha_c^2 - \alpha_{i,f}^2)$ for $\alpha_{i,f} \ll \alpha_c$ and to $\alpha_{i,f}/\mu$ if $\alpha_{i,f} \gg \alpha_c$, [18]. The x-ray penetration depth as a function of incidence angle is shown in Fig. 2.4 (b). The penetration depth for a MnAs film for total external reflection condition is calculated to be about 40 Å. The penetration depth is below ∼ 20 Å for a grazing incidence angle slightly below the critical angle. Thus, grazing incidence diffraction with low incidence and exit angles gives maximum surface sensitivity. At the same time, it minimizes the background intensity, since the atoms deep in the bulk are not excited by the incident wave and therefore enhance the signal-to-noise ratio. This is employed in our work to study the morphology evolution during growth.

The penetration depth approaches to 300 nm, for a incidence angle of about 0.8°, enabling us to study the buried interface. On the other hand, with increasing the incidence angle the intensity of the specularly reflected beam decreases. In MnAs films, the specular reflected intensity decreases by three orders of magnitude for an incidence angle of 0.8°, as shown in Fig. 2.5. Therefore, high intense synchrotron radiation is required to counterbalance the loss in the reflected intensity. In addition, fine tuning of the incidence angle is required to get an optimized intensity from buried thin interfacial structures. In our studies we use incidence angles between 0.6° to 0.8° to investigate the interface configuration of MnAs thin films.

2.3 Experimental setup

This section will briefly describe synchrotron radiation, the beamline, and the six-circle diffractometer used in the experiments. Finally a description of the MBE chamber used to grow the samples is given.

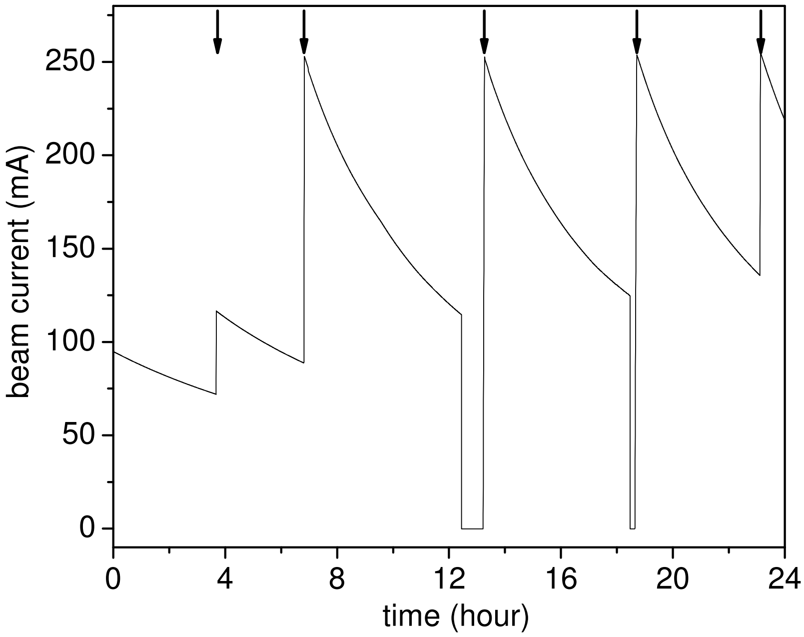

Figure 2.6: Graph showing the beam current inside the storage ring on a typical day. The arrows indicate the injection time of fresh electrons to the storage ring.

2.3.1 Synchrotron radiation

Synchrotrons are circular particle accelerators - facilities built to accelerate sub-atomic particles to almost the speed of light. Any accelerated charged particle produces electromagnetic radiation [19]. The electromagnetic radiation emitted by charged particles circulating in a synchrotron or attached storage ring is called “synchrotron radiation". Synchrotron radiation has

- a high intensity or photon flux,
- a wide spectral range usually from extreme infrared to hard x-rays,
- a small source size, determined mainly by the electron beam dimensions,
- small vertical angular divergence and high collimation.

Our x-ray diffraction experiments were performed at the synchrotron BESSY (Berlin, Germany) on the PHARAO beamline. The high photon flux enables us to study the growth starting from the sub monolayer regime and to detect very thin distorted layers at the interface. BESSY is a third generation synchrotron source and operates at an energy of 1.7 GeV. At first, the electrons are produced from a thermionic emitter, and then accelerated up to few 100 MeV in a booster ring. They are then injected into the large storage ring. The lifetime of the beam in the storage ring is finite [20], and subsequent periodic injection is required. An example of the damping of beam current between consecutive injections at BESSY is shown in Fig. 2.6. At our beamline, the high intensity synchrotron radiation is produced by an undulator driven in the wiggler mode (gap 15.7 mm) located in the high beta section of the storage ring. The undulator consists of 32 periods, each with a length of 125 mm and the gap between the magnets can be tuned from 40 mm to 15.7 mm. The x-rays are guided to the experimental station via a series of optical elements and vacuum pipes called “beamline" as described below. A general introduction

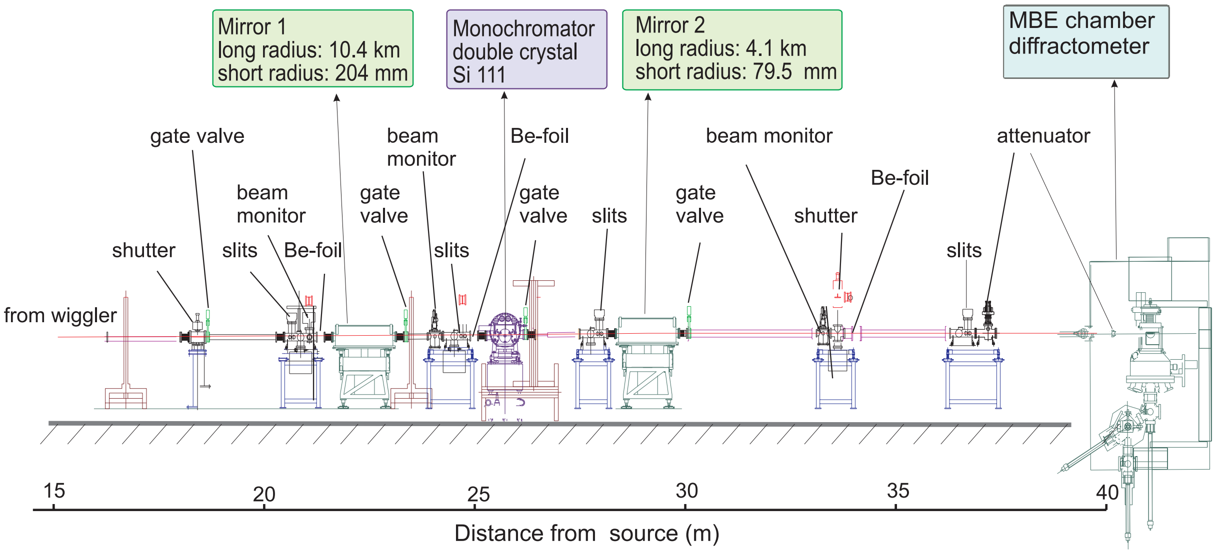

Figure 2.7: Sideview showing the different components of the PHARAO beamline schematically. The distance of the components from the source is also indicated.

to synchrotron radiation is given by Margaritondo [21], Duke [22] and the applications of synchrotron radiation in materials science are reviewed by Sahito and Gohshi [23].

2.3.2 Beamline

The different components of the 40 meter long PHARAO beamline are shown in Fig. 2.7. The details of the PHARAO beamline and experimental setup are described by Jenichen *et al.* [24]. As shown in the figure, the x-ray beam from the wiggler is shaped by water-cooled slits and then the lower energy part of the continuous x-ray spectrum is absorbed by a water-cooled Be foil. After this, the beam intensity, size, collimation, and focusing optics are controlled by two attenuators, three slit units, two mirrors and one double crystal monochromator. The beam path and the influence of the different optical components on the beam is shown schematically in Fig. 2.8. As shown in the figure, the beam leaving the wiggler generally diverges in the horizontal and vertical directions. The divergent beam hits the toroidal first mirror which is a Si crystal coated with Rh and located at a distance of 23.4 m from the source. This collimates the divergent beam to a parallel beam and feeds it into the double crystal monochromator. The double crystal monochromator (DCM) consists of two flat Si (1 1 1) crystals, and selects a particular energy out of the polychromatic white beam. The available energy range is 6 to 12 keV. The energy resolution of the monochromator $\Delta E/E \cong 7 \times 10^{-4}$ [24]. The first monochromator crystal is watercooled from the back surface. The parallel monochromatic beam from the second crystal of the DCM is then focused to the sample surface at the end station by the second mirror as shown in Fig. 2.8. The second mirror is a toroidal mirror located at 29 m from the source. The final beam size at the experimental hutch is approximately 1 mm × 1 mm.

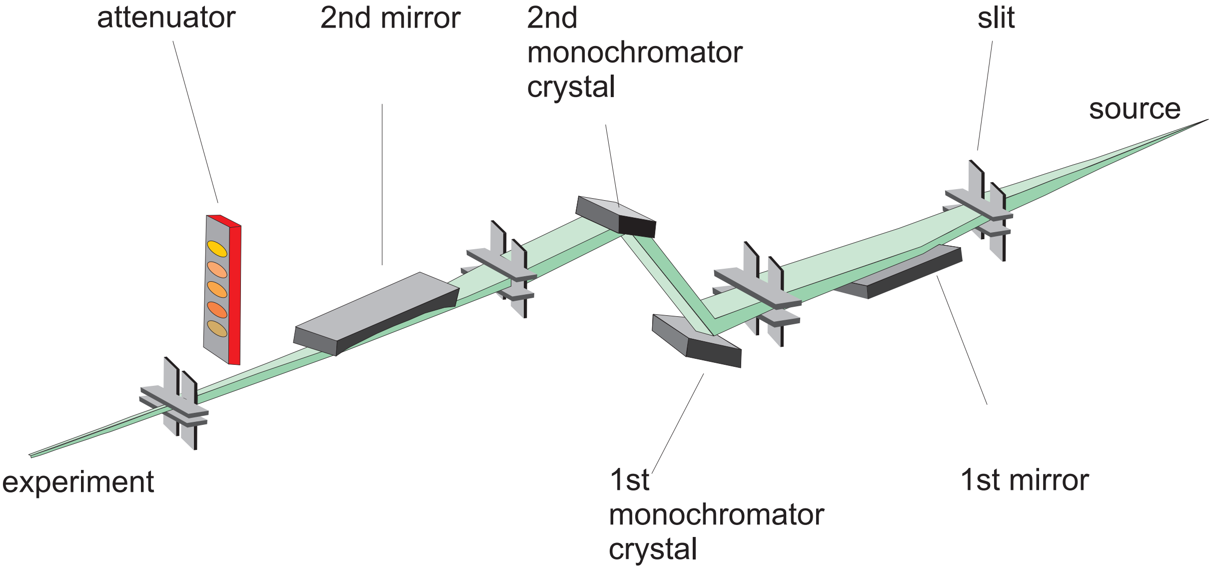

Figure 2.8: A schematic showing the beam path and the effect of different optical elements in the beamline on the x-ray beam.

2.3.3 Diffractometer

The six-circle diffractometer installed at PHARAO is schematically shown in Fig. 2.9. This diffractometer has three degrees of freedom for the sample (θ, χ, ϕ), two for the detector (δ, γ) and one for the combined rotation of both (μ). The χ and ϕ circles are mounted on the θ circle and used to align the sample surface normal with the horizontal diffractometer axis. The alignment is a two step process. First a coarse alignment by optical reflection is performed followed by a precise alignment using an x-ray reflection and a position-sensitive detector. The detector is rigidly mounted to the flight tube which is fixed on the detector bridge as shown in Fig. 2.9. The δ circle rotates the detector about the z-axis (azimuthal angle). The γ circle is a joint movement of flight tube translation

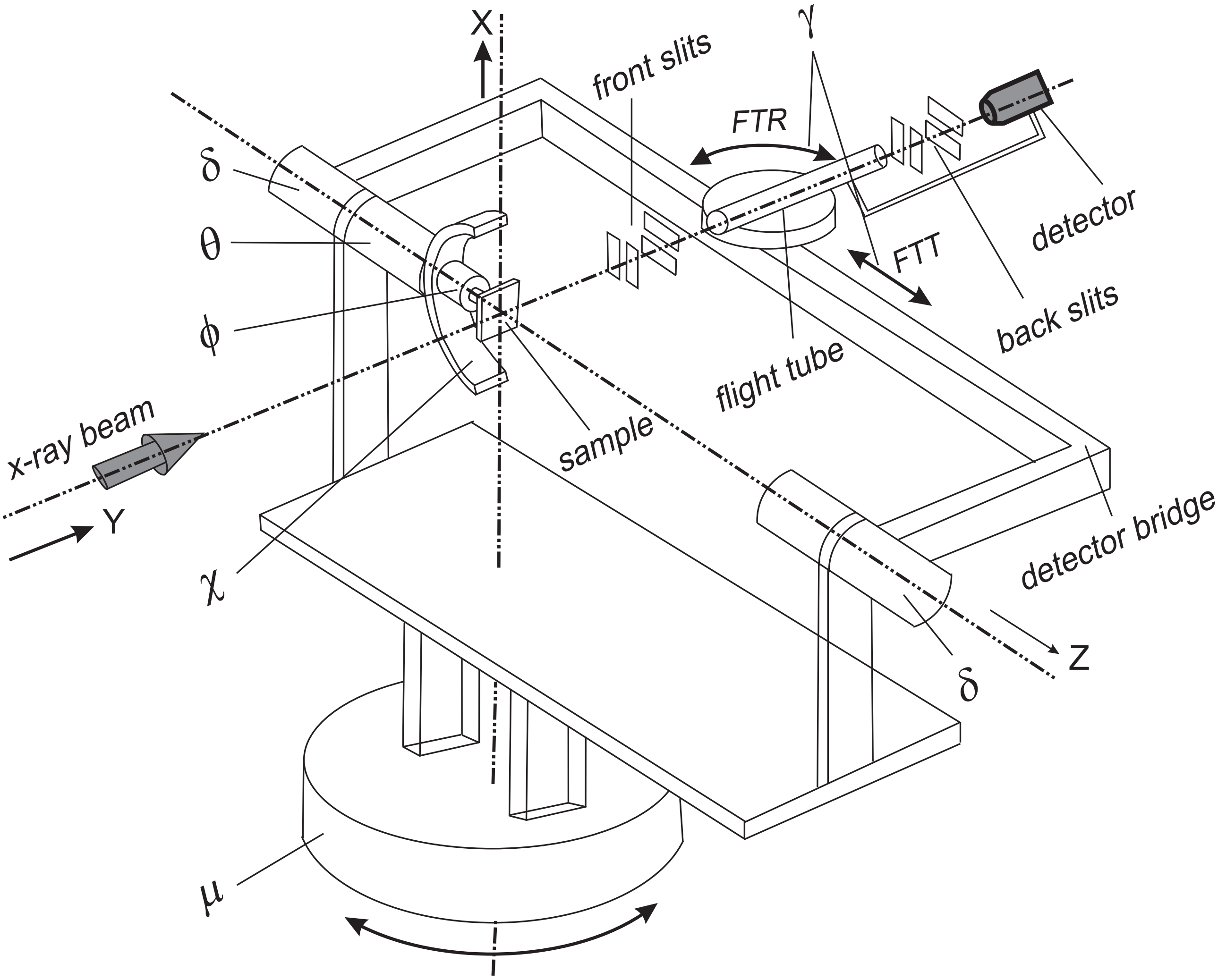

Figure 2.9: A schematic drawing of the six-circle diffractometer installed at the PHARAO beamline showing all the circles set to zero position. All the six circles θ, χ, ϕ, μ, δ, γ (FTT + FTR) are explicitly shown. The movement of the sample is possible with the θ, χ, and ϕ, circles. The detector has two degrees of freedom. It moves about the z axis via the δ circle. The γ circle is a joint movement of flight tube rotation (FTR) and flight tube translation (FTT). FTR and FTT movements are independently shown. The entire diffractometer rotates with the rotation of μ to define the incidence angle. The geometry of the drawing is taken from Fig. 1 of reference [25] .

Table 2.1: The angular range and resolution of each circle of the diffractometer shown in Fig. 2.9.

Circles	Range	Resolution
μ	0 ° - 45°	0.02°
χ	- 3 ° - + 3°	0.001°
ϕ	0 ° - 360°	0.001°
θ	0 ° - 360°	0.001°
δ	0 ° - 130°	0.001°
γ	0 ° - 45°	0.001°

(parallel to z axis) and flight tube rotation (around x axis). It defines the polar angle.

The γ circle can be rotated up to 45°, which allows us to perform out-of-plane measurements (measurement along the crystal truncation rod) with large momentum transfer perpendicular to the surface. The high perpendicular momentum transfer can be achieved by using either a large incidence or large exit angle. In our work, grazing incidence at large exit angles are used. In our case, the sample is mounted vertically, i.e. the surface normal is parallel to the horizontal axis of the diffractometer, as shown in Fig. 2.9. The movement of the detector during an in-plane radial scan and scan along the CTR is schematically shown in Fig. 2.10. The resolution of our diffractometer in the grazing incidence–grazing exit geometry decreases at higher momentum transfer values. The angular range and resolution for each circle are given in table. 2.1. Two units of adjustable slits are used at distances of 200 mm and 1100 mm after the sample to obtain a high angular resolution.

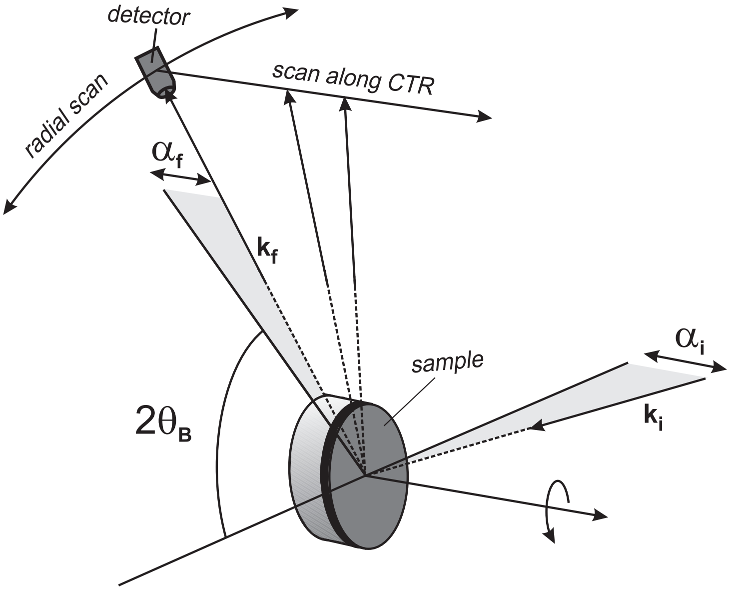

Figure 2.10: Grazing incidence diffraction geometry showing the movement of the detector during radial scans and the scan along the crystal truncation rod. $\mathbf{k_i}$, $\mathbf{k_f}$ and α_i, α_f indicate the incident, and outgoing wave vector and the incident and exit angles, respectively.

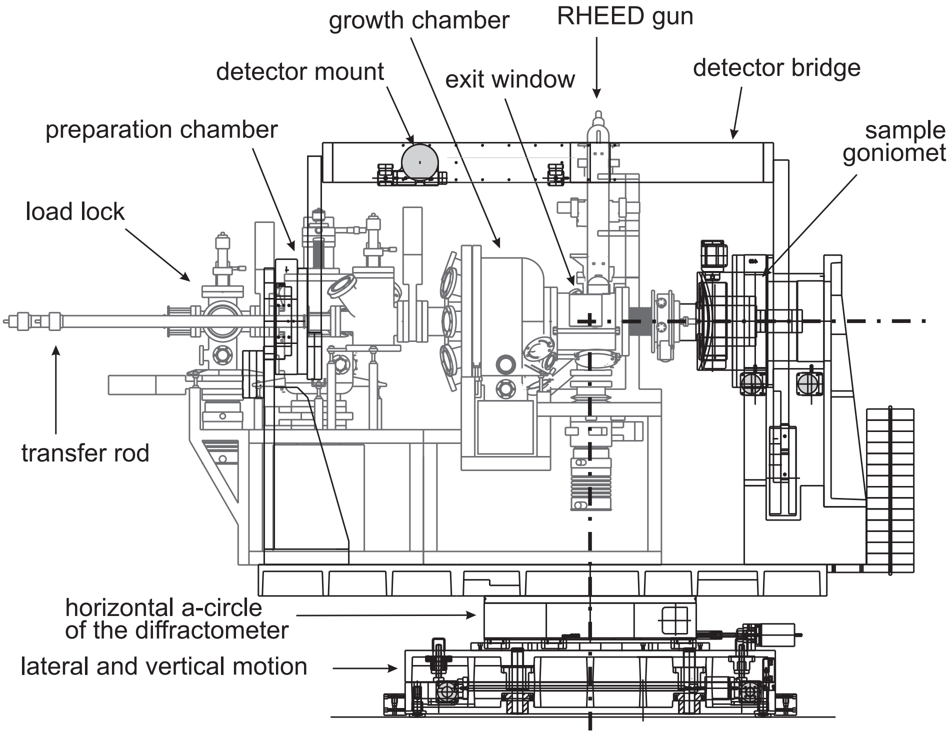

Figure 2.11: Schematic showing the MBE system (gray lines) and the six-circle diffractometer (black lines) at the PHARAO beamline. The sample is positioned at the intersection of the horizontal and vertical axis of the diffractometer.

2.4 Molecular-Beam epitaxy

All the samples that are investigated in this thesis are grown by means of molecular-beam epitaxy. This technique was first developed in the early 1970s for growing high purity epitaxial layers of compound semiconductors [26, 27]. Nowadays MBE provides the greatest flexibility for the growth of many kinds of complex semiconductor multilayers, ferromagnet-semiconductor hybrid structures, epitaxial metal and oxide layers because of the precise control of the thickness (accuracy down to one monolayer), the composition, the cleanliness of the growth process and the doping of the involved layers. It is a versatile technique for growing thin epitaxial structures via the interaction of one or several molecular or atomic beams that occurs on a surface of a heated crystalline substrate. Generally, in MBE, the substrate has a strong influence on the growth process and the deposited film adopts as far as possible the orientation and crystallographic characteristics of the substrate. The important factor which distinguishes MBE growth from other growth techniques is that the growth proceeds in an ultra high vacuum environment and provides real-time assessment of the growing surface by several *in situ* techniques. The MBE growth techniques [28] and the growth of III-V compound semiconductors [29] are reviewed in several publications.

The MBE setup used in this work is integrated inside a six-circle diffractometer as schematically shown in Fig. 2.11. The MBE system consists of four chambers (load lock, preparation chamber, sample exchange chamber and growth chamber) separated by mechanical gate valves. The growth chamber is equipped with six effusion cells (Ga, In, Mn, Al, As, Sb) which allows the growth of a variety of materials. The growth chamber

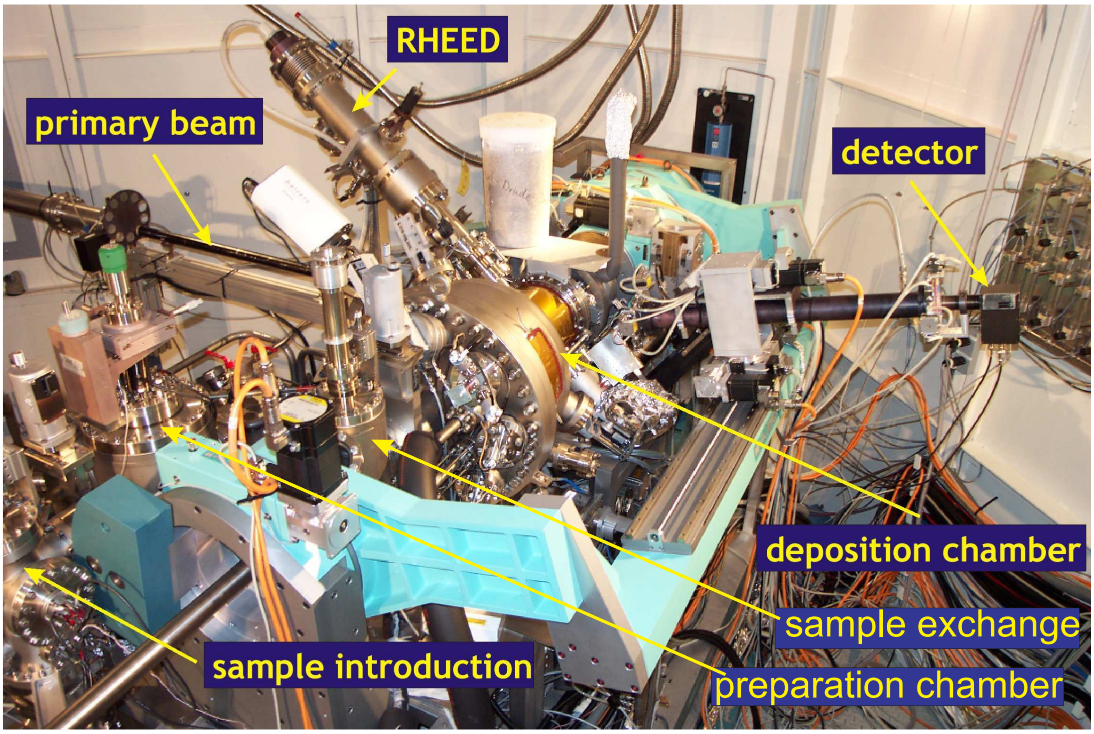

Figure 2.12: The MBE system and the six-circle diffractometer. The incoming x-ray beam and the RHEED gun position are indicated. All four chambers of the MBE system are shown.

has two large Beryllium windows around the sample which allow the x-rays to go in and come out. The base pressure of the growth chamber is maintained at about 7×10^{-10} mbar by the combination of an ion pump and a turbo-molecular pump. During the III-V compound growth, the chamber pressure is maintained at about 9.5×10^{-8} mbar. The group-V component (As), is kept in overpressure since it desorbs from the hot substrate and only incorporates together with a group III atom. Since the sticking coefficient of the group III atom (Ga) and of Mn are unity at our growth temperatures, the growth rate is controlled by the group III flux. The group V materials do not control the growth rate. Therefore, only the group III cells (Ga, In, Al) and the Mn cell are provided with mechanical shutters to abruptly switch on and off the fluxes. The As is available in the form of As_4 molecules. The fluxes of the effusion cells determine the growth rate and therefore need precise control. In our system the cell temperatures are measured by using type C Tungsten-Rhenium thermocouples and controlled via extremely stable feedback loops and proportional integral derivative (PID) temperature controllers. Two liquid nitrogen cooled shrouds, one around the effusion cells and the other around the substrate heater, help to maintain a stable temperature and high vacuum. The sample is mounted on a specially designed holder and connected to the ϕ circle of the diffractometer. The movements of the sample are controlled by the diffractometer by means of a two stage differentially pumped rotary feedthrough. For additional safety, the rotary feedthrough is encapsulated in a Ar environment to prevent the growth chamber from contamination in case of a leak. The picture of the experimental setup consisting of MBE and diffractometer at PHARAO beamline is shown in Fig. 2.12.

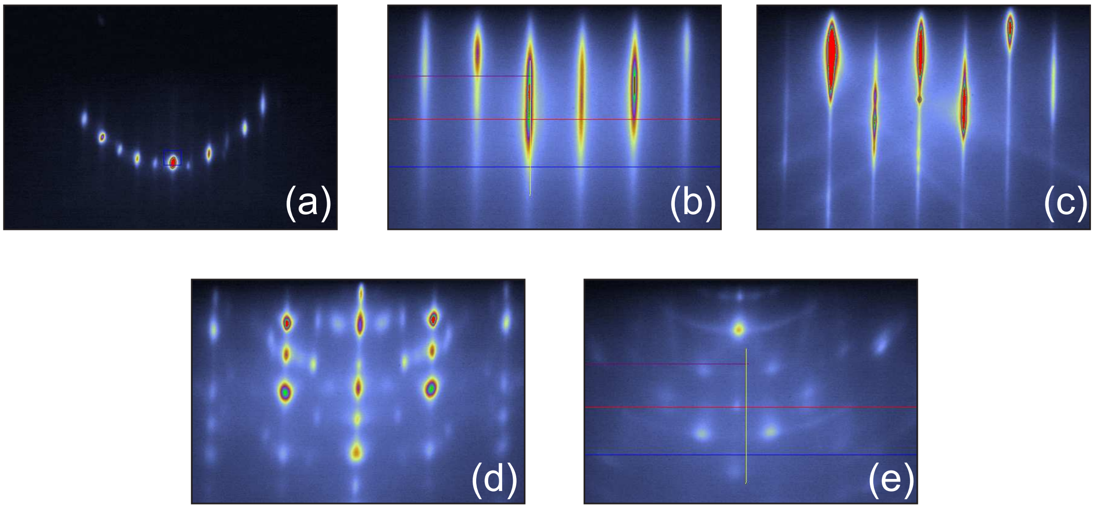

Figure 2.13: RHEED patterns recorded during growth on different surfaces. (a) Showing the diffraction spots on a Laue circle from a smooth InAs (0 0 1) surface (taken by W. Braun). (b) Showing the diffraction streaks recorded during growth of MnAs on GaAs (0 0 1). (c) Streaky pattern from a GaAs (1 1 3)A surface during buffer layer deposition. (d) Shows the transmission pattern through the three dimensional mounds of MnSb growing on GaSb (0 0 1). (e) RHEED pattern showing discontinuous rings, recorded from a polycrystalline film of MnAs grown on InAs (0 0 1).

2.5 Reflection high-energy electron diffraction

It is well known that reflection high-energy electron diffraction (RHEED) is a powerful *in situ* tool for real-time characterization of growth processes in high and ultrahigh vacuum. This technique consists of the scattering of high-energy electrons (5 - 20 keV) from the crystal surface at glancing incidence angles. Although electrons at this energy can coherently penetrate up to 100 Å, due to the small angle of incidence (about 1° to 3°) the penetration depth is limited to a few angstroms. This makes RHEED particularly suited for surface characterization, and allows us to analyze the growing surface during MBE growth. The experimental setup of this technique is very straightforward and can be found in many textbooks [30, 31]. A high-energy focused electron beam produced by an electron gun is directed towards the sample surface at a glancing incidence angle and the diffracted electrons are then allowed to impinge on a phosphorescent screen mounted opposite to the electron gun. The diffraction pattern on the fluorescent screen is digitally recorded via a CCD (charge coupled device) camera connected to a computer with a digital image processing software [32]. In our case, the sample is mounted vertically and the sample holder can be rotated about the horizonal axis thus allowing the electron beam to diffract along different crystallographic directions. The position of the RHEED gun in our MBE setup is shown in Fig. 2.12.

Since in RHEED the electrons are diffracted from a very thin almost two-dimensional layer near the surface, the Laue condition for diffraction along the growth direction is relaxed. Therefore, instead of points, the reciprocal lattice of the thin surface layer consists of rods along the direction normal to the surface (see the section 2.1.2). The kinematic diffraction condition for the RHEED pattern is given by the intersection of these reciprocal lattice rods with the Ewald sphere of radius k; $k = 2\pi/\lambda$ is the electron wave vector. The expected pattern should consist of a set of sharp spots lying on concentric arcs called Laue circles, for a smooth surface. As an example, the RHEED pattern for a rather smooth surface with the spots lying on the Laue circle is shown in Fig. 2.13 (a). However, in reality the intensity of these sharp spots is distributed with the main spreading direction perpendicular to the crystal surface and along the direction of the reciprocal lattice rods. There are many factors that contribute to the spread of intensity, and lead to a streaking of the RHEED pattern, often quoted in the literature as a characteristic of a smooth surface. The streaking is primarily due to relatively small deviations of the crystal surface from ideal positions due to steps and shallow mounds [33, 34]. The instrumental resolution (the spread in energy of the incident electrons, angular distribution of the electron beam) and phonon scattering also contribute to the streaking of RHEED patterns [30, 35]. Such streaky RHEED patterns from the MnAs and GaAs surface are shown in Figs. 2.13 (b) and (c), respectively. Due to the multiple scattering of the electrons, the overall shape and intensity of the RHEED pattern is difficult to interpret quantitatively. The width of the streaks can be directly related to the average coherent terrace size on the surface. If the full width at half maximum (FWHM) is w then the average terrace size is given by $2\pi/w$ [36], (This is an approximate value because the actual size depends on the distribution of steps on the surface). Therefore, the average terrace size on the GaAs surface [Fig. 2.13 (c)] is larger than the one of the MnAs surface [Fig. 2.13 (b)]. Another indication of a well-ordered surface is the presence of a regular pattern of sharp lines called Kikuchi lines in the RHEED pattern present in Fig. 2.13 (c). Kikuchi lines are the result of the incoherent scattering of electrons and can be explained by a two step scattering process of the electrons [31].

Even for the less perfect surface with high roughness the electron beam transmits through the three-dimensional mounds and produces sharp spots. One such example during the growth of MnSb on GaSb (0 0 1) is shown in the Fig. 2.13 (d). For completely polycrystalline films the RHEED pattern consists of diffraction rings like the powder diffraction pattern. The presence of discontinuous rings during the growth of MnAs on InAs (0 0 1) is shown in Fig. 2.13 (e).

2.6 Different modes of epitaxial growth

Ernst Bauer first classified the observed epitaxial growth modes into three different categories according to their surface energy [37]. These three growth modes are shown for different layer coverages in Fig. 2.14. Depending on the surface energy of the epilayer (γ_e), substrate material (γ_s) and the interface energy ($\gamma^\star$) two things can happen. First, if the surface energy of the film is lower than the sum of the substrate surface energy and interface energy ($\gamma_e < \gamma_s + \gamma^\star$), wetting of the substrate occurs by the formation of a two-dimensional strained layer. Putting it in another way, when the deposited atoms are more strongly attracted to the substrate than they are to themselves, and the misfit is small, then result is layer-by-layer growth (Frank-van der Merwe) as shown in Fig. 2.14 (a). In layer-by-layer growth, the film is strained to match the in-plane substrate lattice spacing at the interface. Second, if $\gamma_e > \gamma_s + \gamma^\star$, the deposited atoms are more strongly attracted to themselves than to the substrate then three-dimensional islands nucleate with the absence of a wetting layer. This is known as Volmer-Weber growth [38] and shown schematically in Fig. 2.14 (b).

An intermediate case is the layer-plus-island growth which occurs when the interface

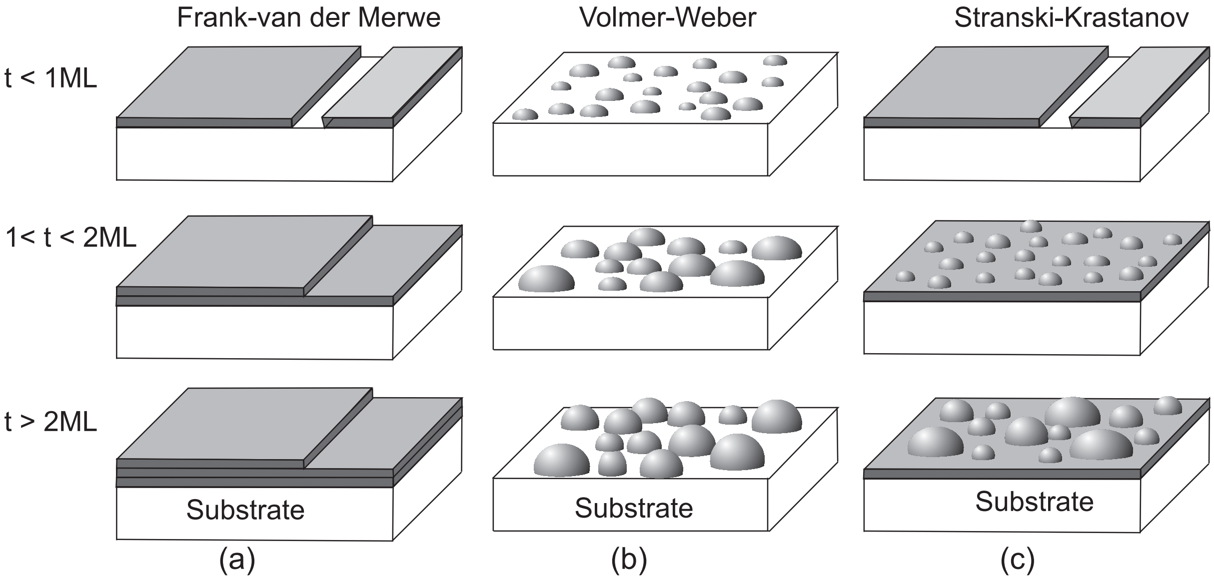

Figure 2.14: Schematic diagram showing the different modes of epitaxial growth. The layer coverage is denoted by 't'.

energy increases with increasing layer thickness. In this case, first a strained continuous wetting layer forms on the substrate, and then strain is released by the formation of 3D islands on that layer. This is known as Stranski-Krastanov (SK) growth mode and shown schematically in Fig. 2.14 (c). SK growth is reported to occur during the growth of Ge/Si [39] and InGaAs/GaAs [40]. It is worth to point out that the strain in large Volmer-Weber or Stranski-Krastanov islands is ultimately released by the formation of misfit dislocations. More details of the thermodynamics and kinetics of different epitaxial growth modes are given by Venables [41]. Another kind of growth mode, which could be considered as the high-temperature version of layer-by-layer growth, is the so-called step-flow growth mode. Steps are formed whenever the surface of the substrate is cut slightly off from a low index plane or when mounds are present on the surface. In step-flow, all adatoms diffuse and adhere to the step edges. Therefore, no nucleation of islands takes place on the terraces. As we will discuss in chapter 3, the growth of MnAs on GaAs cannot easily be sorted into one of these known categories, at least according to our present experimental results.

2.7 Superconducting quantum interface device magnetometry

The direct superconducting quantum interface device (dc-SQUID) is currently the most sensitive magnetic field detector and allows us to measure the integral properties of the magnetic films. It combines flux quantization with Josephson effect. The dc-SQUID is a simple device consisting of two Josephson junctions connected in parallel in a closed superconducting loop as shown in Fig. 2.15 (a). When a current flows through this loop, it sends Cooper pairs of electrons tunnelling through the Josephson junctions. An applied magnetic field penetrating the ring, however alters the flow. Specifically, it changes

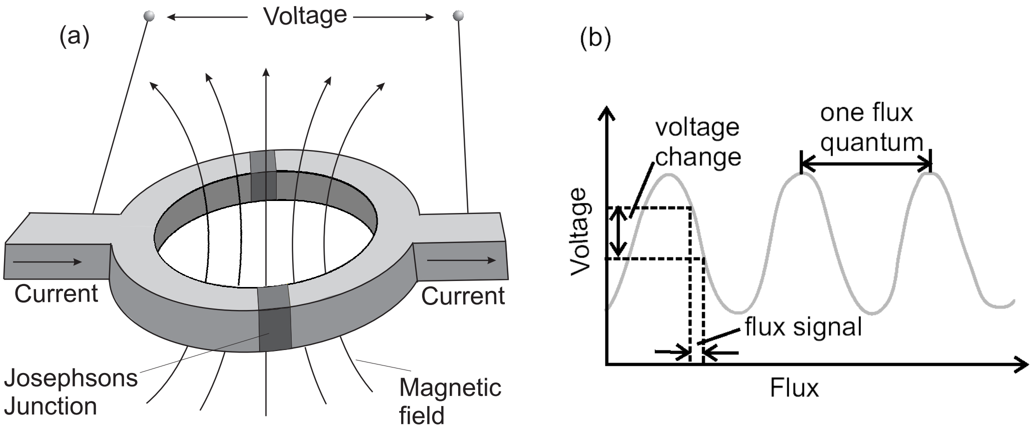

Figure 2.15: Schematic diagram showing the principle of DC SQUID. The two Josephson junctions form a superconducting ring that provides information about the change in flux. (b) Shows the output voltage as a function of flux. This figure is adopted from [42] .

the quantum-mechanical phase difference across each of the two junctions. These phase changes affect the critical current of the SQUID. An increase or decrease in the magnetic field causes the critical current to oscillate between a maximum and a minimum value. The maximum occurs when the flux administered to the SQUID equals an integral number of flux quanta through the ring; the minimum value corresponds to a half-integral number of flux quanta [42]. In practice, we do not measure the current but rather the voltage across the SQUID, that swings back and forth under a steadily changing magnetic field as shown in Fig. 2.15 (b). This quantum interference effect provides us a digital magnetometer, where each digit represents a flux quantum. The SQUID is a flux-to-voltage transducer, converting a tiny change in magnetic flux into an oscillating voltage.

Our SQUID magnetometer system (MPMS quantum design [43]) is composed of several units: the dewar, the probe, the SQUID assembly and the electronic control system. The probe contains a high precision temperature control system, allowing measurements between 1.9 and 400 K and with an accuracy of 0.01 K (according to the data sheet provided by the manufacturer), and a superconducting electromagnet delivering a field of up to 5×10^4 G with a field accuracy of 0.1 G. The dewar consists of an inner liquid helium reservoir and an outer liquid nitrogen jacket to reduce liquid helium boil out. The liquid helium is used both to maintain the electromagnet in a superconducting state and to cool the sample space. The samples are mounted between two hollow plastic straws and inserted into the dewar.

Chapter 3

Growth of MnAs on GaAs (0 0 1) surface

3.1 Introduction

In semiconductor spintronics, one of the most important issues is the development of ferromagnet/semiconductor hybrid structures in which the spin degree of freedom of the electron can be used. Since magnetic materials are usually dissimilar to semiconductors, the integration of magnetic or spin-related functions with semiconductor electronics has been considered to be difficult. However, advanced fabrication technologies, especially molecular-beam epitaxy, offer new opportunities for exploration in this direction. The integration of a ferromagnetic material (MnAs) with a semiconductor (GaAs) has been demonstrated although their corresponding crystal structures, lattice constants and chemical bondings are different. Nevertheless, MnAs has the potential for spintronics applications for several reasons.

- It has a ferromagnetic (α MnAs) phase at room temperature.
- It is thermally stable and chemically inert on GaAs.
- It can be grown with the same MBE chamber used for GaAs growth which means that growth is compatible with the existing III-V MBE technology.

In this chapter, first a brief introduction to bulk MnAs and epitaxial MnAs thin films are given and then we discuss aspects of MnAs growth on the GaAs (0 0 1) template.

3.1.1 Bulk MnAs

Bulk MnAs was first studied by Heusler [44]. At room temperature MnAs crystalizes in the NiAs crystal structure that has alternating hexagonal planes of Mn and As atoms as shown in Fig. 3.1 [45, 46]. The bulk lattice parameters at the room temperature are a=3.72 Å and c=5.71 Å [46]. According to the As-Mn phase diagram [47], MnAs assumes the NiAs-type γ MnAs structure above 125 °C, the orthorhombic MnP-type β MnAs structure (B31) between 125 °C and 40 °C and the ferromagnetic NiAs-type α MnAs ($B8_1$) structure below 40 °C. The ferromagnetic phase of MnAs having a Curie temperature $T_c \simeq 317\,K$ was discovered by Hilpert and Deckmann in 1911 [48]. Serres [49] and Guillaud [50] found that

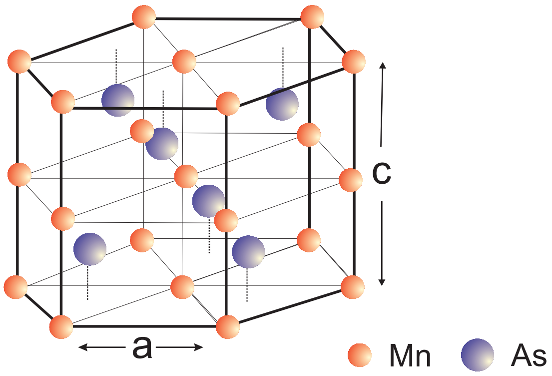

Figure 3.1: NiAs-type crystal structure of α MnAs consisting of hexagonal planes of Mn and As alternating in a sequence ABACABAC.. The a and c axis are indicated in the figure.

a metal-insulator transition occurs at T_c. Willis and Rooksby [46] observed a large (1.8%) discontinuous density change at $T_c = 317\,K$. The density change was used by Bean and Rodbell [51] to explain the loss of magnetization at 317 K that occours with a latent heat of 1.79 cal/gm [52]. The phase transition at 317 K is abrupt in bulk MnAs. The phase transition is a coupled magnetic and structural first-order transition as confirmed by the presence of latent heat [52]. The change in T_c with fields $0 < B < 11\,T$ and at a pressure P=1Kbar was studied by De-Blois and Rodbell [52]. A second-order phase transition, without any volume change, was detected by calorimetric measurement at 399 K [53]. The α MnAs shows metallic conductivity [54], and therefore contains itinerant electrons.

It is still under discussion whether the ferromagnetism in MnAs should be described by a double exchange mechanism due to the strongly directional, hybridized Mn-As bonds or has mainly itinerant character, because of the metallic behavior of MnAs [55]. In the ferromagnetic α MnAs phase, the spin moments are carried exclusively by Mn ions. The Mn ions in the unit cell have two types of magnetic neighbors: a pair of first nearest-neighbors are along the c axis at a distance of $c/2$=0.286 nm and six second nearest-neighbors in the hexagonal plane at a distance of 0.372 nm. Usually, in hexagonal close-packed magnetic materials the easy axis lies along the c axis. In contrast to this, in MnAs the easy axis of magnetization is along the a axis [52].

3.1.2 Epitaxial MnAs layers

Epitaxial ferromagnetic MnAs films on semiconductors have received considerable interest in the last few years because they open up a perspective for the development of hybrid spin based magnetic-semiconductor devices. The research interest in this direction was triggered during the last decade by the achievement of good quality epitaxial layers of MnAs. Tanaka *et al.* [8, 56] first showed that MnAs can be epitaxially grown on III-V semiconductors by MBE. The growth of high-quality epitaxial MnAs layers on different orientations of GaAs [(0 0 1) [57, 58, 59], (1 1 1) [60], (1 1 3) [61], (1 1 0) [62]] and on Si (0 0 1) [63] has been reported since then. A single-phase high-quality MnAs film was achieved by growing on the As-rich c(4×4) and d(4×4) [disordered c(4×4)] reconstructed GaAs (0 0 1) surfaces [56, 58, 59]. Schippan *et al.* [64] presented a surface phase diagram showing various stoichiometry-dependent reconstructions during the epitaxial growth of MnAs films on GaAs (0 0 1) substrates, which indicates the growth of well-ordered material. These

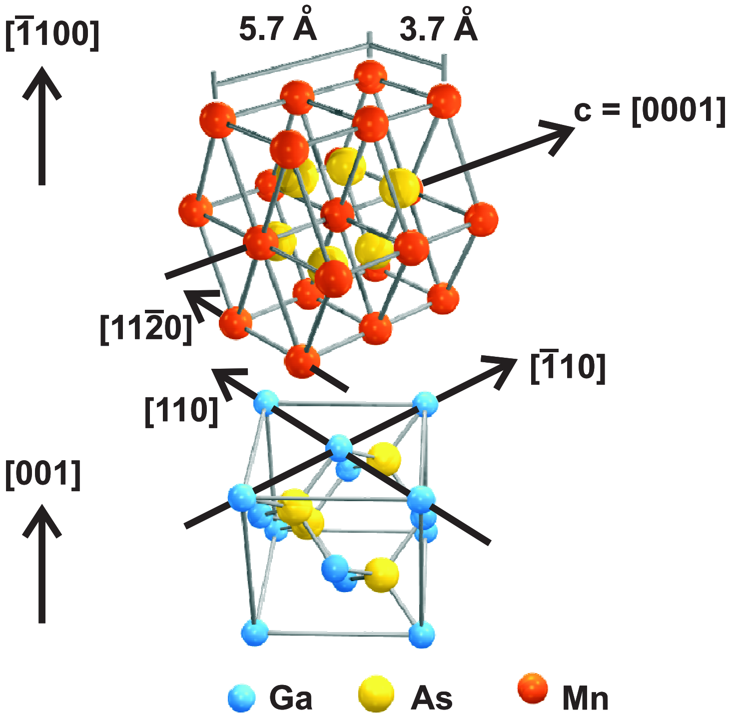

Figure 3.2: Epitaxial relationship with parallel MnAs $(1\,\bar{1}\,0\,0)$ and GaAs $(0\,0\,1)$planes. Three unit cells of MnAs form the hexagon shown here (adopted from [58]).

surface phases show different reconstructions depending on the growth temperature and $\mathrm{As_4/Mn}$ flux ratio.

The epitaxial relationship of MnAs on GaAs $(0\,0\,1)$ is shown schematically in Fig. 3.2. Conventionally, the $[1\,1\,\bar{2}\,0]$ direction is called a axis and the $[0\,0\,0\,1]$ direction is called c axis. The lattice misfit f along the in-plane a axis of MnAs is defined as:

$$f = \frac{\mathrm{d_{GaAs}}(2\,2\,0) - \mathrm{d_{MnAs}}(1\,1\,\bar{2}\,0)}{\mathrm{d_{GaAs}}(2\,2\,0)}, \tag{3.1}$$

where $\mathrm{d_{MnAs}}(\mathrm{h\,k\,l\,m})$ and $\mathrm{d_{GaAs}}(\mathrm{h\,k\,l})$ are the interplanar spacings of the corresponding atomic planes. The misfit along this direction is calculated to be 6.9%. The lattice misfit along the c axis is

$$f = \frac{\mathrm{d_{MnAs}}(0\,0\,0\,1) - \mathrm{d_{GaAs}}(1\,\bar{1}\,0)}{\mathrm{d_{GaAs}}(1\,\bar{1}\,0)}, \tag{3.2}$$

which gives a numerical value of $\sim 43\%$. If we define the misfit on the basis of the distance between adjacent lattice planes of the same kind [$\mathrm{d_{MnAs}}(0\,0\,0\,2)$ and $\mathrm{d_{GaAs}}(1\,\bar{1}\,0)$] then the misfit is

$$f = \frac{\mathrm{d_{MnAs}}(0\,0\,0\,2) - \mathrm{d_{GaAs}}(1\,\bar{1}\,0)}{\mathrm{d_{GaAs}}(1\,\bar{1}\,0)}, \tag{3.3}$$

resulting in a value of 29 %. This value is so high that epitaxial growth can hardly be expected. As was found already in earlier work [65], the epitaxial relationship corresponds to a coincident lattice [66] with two units of MnAs to three units of GaAs in the c axis. The formation of a near coincidence lattice was experimentally confirmed by high-resolution transmission electron microscopy [67]. Every fourth MnAs $(0\,0\,0\,2)$ plane corresponds to every sixth GaAs (2 2 0) plane. This 4 to 6 coincident lattice reduces the lattice misfit to 5 %, which is a reasonable value for the epitaxial growth.

Although epitaxial growth of MnAs was reported a decade ago, the strain state of the film during growth, and the exact mechanism of epitaxial growth is not completely understood. This is due to the fact that while cooling to room temperature from growth temperature of 250 °C, MnAs undergoes several structural and magnetic phase transitions. It is therefore difficult to deduce the strain state of the film during epitaxy by *ex situ* measurements at room temperature. Only *in situ* experiments can provide access to the strain state of the system at the growth temperature during deposition. Grazing incidence x-ray diffraction is well suited for this purpose, since it can be used *in situ* in ultra-high vacuum, without perturbing the MBE growth, and the data can be analyzed quantitatively using the kinematic approximation. We have carried out *in situ* studies of the strain evolution of MnAs during growth by RHEED and GID and our findings are discussed in the following sections.

3.2 GaAs (0 0 1) substrate preparation

The structural quality, orientation and morphology of epitaxial metallic films on semiconductors depend critically on the stoichiometry and reconstructions of the starting substrate template. Therefore, to achieve high–quality reproducible epitaxial layers, substrate preparation should be done with utmost care. In particular, for MnAs growth Tanaka *et al.* [56] reported that the dominant epitaxial orientation of MnAs is mainly defined by the surface reconstruction and the termination of the GaAs (0 0 1) template [68].

The 1 mm thick epiready n-type doped (0 0 1) oriented GaAs wafers were supplied by Wafer Technology surface for epitaxy is protected by a grown oxide layer on the substrate. Prior to the oxide removal, the substrate is heated to 150 °C for about an hour, to desorb the water in a separate preparation chamber. This step is done to ensure the cleanliness of the growth chamber and to keep the contamination low. The wafer is then transferred

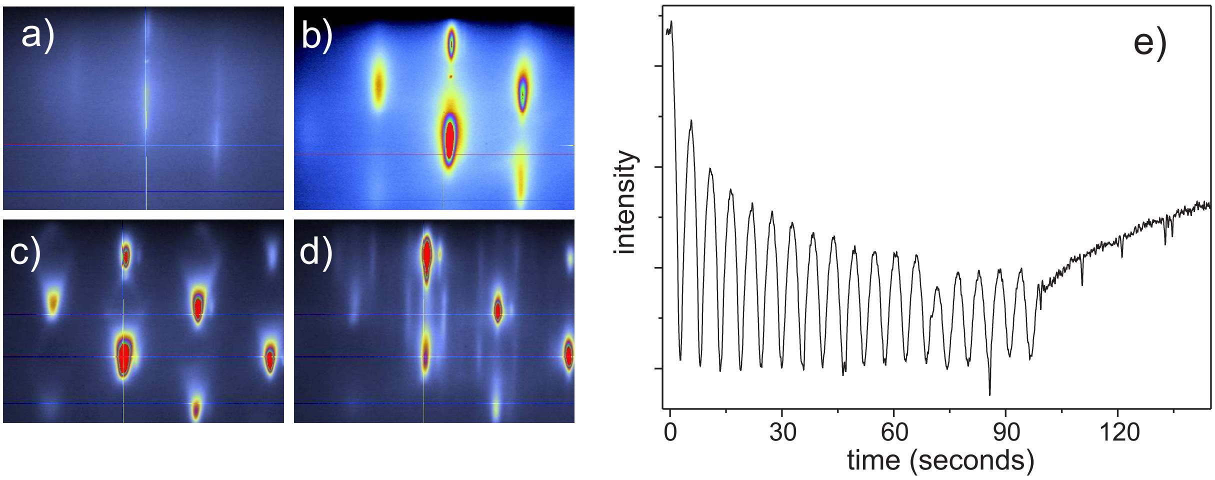

Figure 3.3: RHEED patterns of GaAs (0 0 1) substrate recorded at (a) 500 °C, (b) 580 °C, during oxide desorption. (c) RHEED pattern showing chevron spots arising from pyramidal facets. (d) RHEED during the buffer layer growth. (e) RHEED oscillations recorded during GaAs buffer layer growth indicating a smooth layer-by-layer growth mode. Spike artefacts are from the discharges in the RHEED gun.

to the growth chamber in vacuum for oxide desorption. The oxide desorption is done under As_4 flux.

We constantly monitor the oxide desorption from the GaAs surface by RHEED while heating at a rate of 10 °C/min. The static RHEED pattern of the GaAs surface at a temperature of 500 °C shows a diffuse background due to the amorphous oxide layer Fig. 3.3 (a). High intensity spots in Fig. 3.3 (b) corresponding to the bulk GaAs reflections appear immediately after the oxide is completely desorbed at 580 °C. The removal of the oxide creates a rough faceted morphology on the GaAs surface. These facets are planarized by the buffer layer growth at a temperature, which is 30 °C below the oxide desorption temperature. From the observation of chevron shaped RHEED spots as shown in Fig. 3.3 (c), a 3D growth of the buffer layer is obvious at the first stages of growth. Upon further growth the chevrons disappear as the valleys are filled. High-temperature (590 °C) buffer growth is then used in order to get a smooth surface with large terraces. The appearance of RHEED streaks corresponding to the GaAs surface reconstruction Fig. 3.3 (d), indicates the formation of a smooth buffer layer. We did a continuous buffer growth at rate 1 manolayer (ML)/sec. Large and flat GaAs terraces are achieved by pulsed deposition with a 1:3 time ratio for Ga shutter opening to closing. RHEED oscillations [Fig. 3.3 (e)] are clearly observed during this pulsed deposition, indicating the layer-by-layer growth. The pulsed buffer layer is grown at a lower growth rate of 0.3 ML/sec, and monitored by the RHEED intensity oscillations shown in Fig. 3.3 (e).

3.3 Nucleation of MnAs studied by RHEED azimuthal scans

We use *in situ* RHEED azimuthal scans and GID to study the nucleation and subsequent evolution of strain during epitaxy. In this section we will discuss qualitatively the rotational and static RHEED measurements during growth of MnAs.

3.3.1 Azimuthal RHEED

The standard RHEED measurement widely in use is performed without moving the sample and uses a flat screen to image reciprocal space. To measure the two-dimensional intensity distribution parallel to the surface a different approach is required. The use of a spherical RHEED screen allows the imaging of reciprocal lattice rods in the vicinity of the specular (0 0) rod, permitting the determination of the 2D surface lattice symmetry from a static RHEED pattern [69]. However, such a spherical RHEED screen allows access only to very limited regions of reciprocal space near to the specular (0 0) rod. A much larger area of reciprocal space can be imaged by recording an electron diffraction pattern while rotating the substrate about its surface normal [70]. The recorded intensity pattern allows us to reconstruct a planar cut through the reciprocal space parallel to the surface [31]. These scans are called RHEED azimuthal scans. This type of cut of the reciprocal space is similar to the diffraction patterns recorded by low energy electron diffraction (LEED) measurements, except that the LEED pattern is a spherical cut, whereas our azimuthal scans are planar. The planar azimuthal scans provide a better insight into the surface morphology, reconstruction, and kinetics during growth.

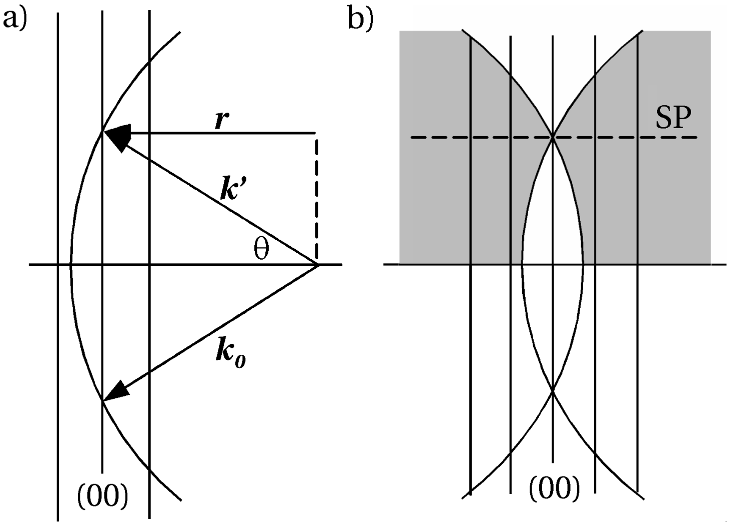

Figure 3.4: Reciprocal space geometry of a) static RHEED and b) RHEED during substrate rotation around an axis parallel to (0 0). The shaded area (rotated around (0 0)) represents the volume of reciprocal space accessible with substrate rotation (Adopted from [31]).

The reciprocal space geometries for both traditional and azimuthal RHEED are shown in Fig. 3.4. Figure 3.4 (a) shows the Ewald sphere construction for the static case. The condition for elastic scattering requires that both $\mathbf{k_0}$ and $\mathbf{k}'$ must terminate on the (0 0) lattice rod for any incidence angle θ. In this case, both the reciprocal lattice rods as well as the Ewald sphere remain stationary. On the other hand, in azimuthal RHEED scans, the reciprocal lattice rods revolve around the specular (0 0) rod because of sample rotation, while the Ewald sphere remains fixed (if we neglect wobble and miscut of the sample). Therefore, in one rotation of the sample, the Ewald sphere scans almost the entire upper half of the reciprocal space [shown by the shadowed region in Fig. 3.4 (b)]. The plane shown as SP in Fig. 3.4 (b) is the specular plane. Recording intensity along a line during the substrate rotation enables us to reconstruct a complete cut through the

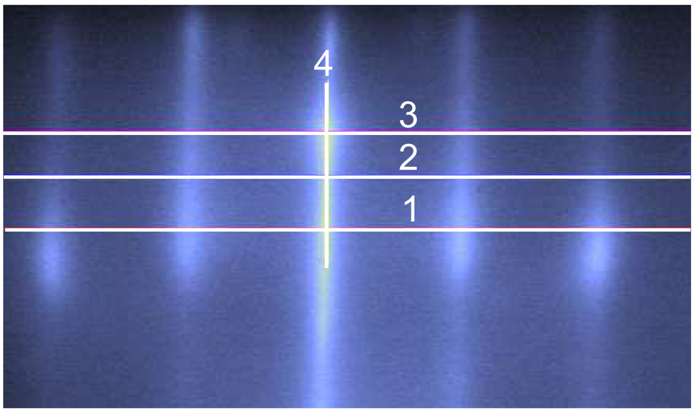

Figure 3.5: RHEED pattern along the 1× direction of MnAs superimposed with four lines (sensors) along which the intensities are recorded during the substrate rotation. The sensors are used for recording the azimuthal scans.

reciprocal space parallel to the surface.

As an example, the RHEED pattern along the 1× direction of MnAs superimposed by four lines along which the intensities are recorded during the substrate rotation is shown in Fig. 3.5. Due to the electrical field of the sample heater, the specular spot usually describes an elliptical movement during sample rotation. The vertical line (shown as number 4 in Fig. 3.5) serves as a reference on which to hold the specular spot by small manual adjustments of the beam position during the measurement.

The sample holder was rigidly connected to the goniometer of the diffractometer, which enabled us to rotate the sample with high precision. The rotation speed of the substrate was about 0.16 rpm. The sample, typically one quarter of a 2 inch GaAs (0 0 1) wafer, was fixed at one corner by a clamp on the specially designed sample holder [24]. This made it possible to have unshadowed access to the sample surface while rotating it by 180 °. The electron gun was operated at 20 kV. The RHEED intensities were recorded with a charge coupled device (CCD) camera at a rate of 25 Hz using a specially designed image acquisition system [32]. Since we recorded the measurement line across the complete width of the diffraction pattern, half a rotation was sufficient to reconstruct the complete plane. One half rotation took about 120 s resulting in about 3000 lines to build the image.

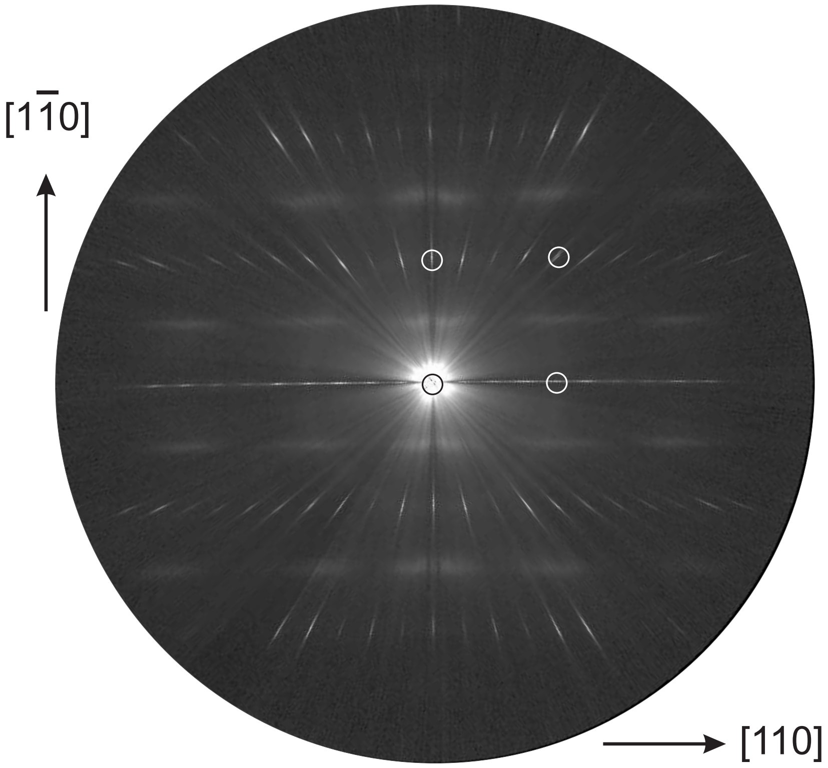

Figure 3.6: RHEED azimuthal scan corresponding to the GaAs β (2×4) reconstructed surface. The (2×4) unit cell is indicated by the circles that enclose it. The in-plane [1 1 0] directions are also indicated.

3.3.2 Azimuthal Scans of the GaAs (0 0 1) template

After the buffer layer deposition, we performed RHEED azimuthal scans on the GaAs (0 0 1) surface at a temperature of 550 °C which is close to the center of the stability regime of the GaAs $\beta\,(2\times4)$ surface reconstruction. The processed azimuthal scan is shown in Fig. 3.6. The surface unit cell and the different in-plane [1 1 0] directions are indicated. The number of diffraction orders (reciprocal space unit cells) that can be imaged is only limited by the RHEED screen size. The alternating rows of sharp 4× and diffuse 2× spots can be clearly identified. The spots in the azimuthal scan are elliptical with the long axis along the radial direction. This shape anisotropy results from the different transfer width of RHEED parallel and perpendicular to the beam [71]. Note that in conventional RHEED, only the long direction with low resolution is accessible.

After an extended annealing at 550 °C, the substrate was cooled down to 250 °C to obtain a c(4×4) reconstructed surface, which seems to be vital to obtain single orientation high-quality MnAs films [8, 58]. The RHEED azimuthal scan showing a c(4×4) reconstruction recorded at 250 °C is shown in Fig. 3.7. This c(4 × 4) reconstruction of GaAs (0 0 1) surface is characterized by additional As-containing dimers bound to a bulk-like As top layer [72]. The unit cell with the centered mesh is indicated by the white circles. From the two-dimensional azimuthal scan, one can immediately distinguish between the c(4×4) and a (2×2) structure which would look the same when observed along one of the typically used {1 1 0} azimuths in static RHEED. The square surface unit cell with the 2× periodicity along ⟨1 1 0⟩ and 4× along ⟨1 0 0⟩ can be clearly identified and is marked by white circles indicating the (0 0), (1 1), (0 2) and ($\bar{1}$ 1) rods at its corners. The

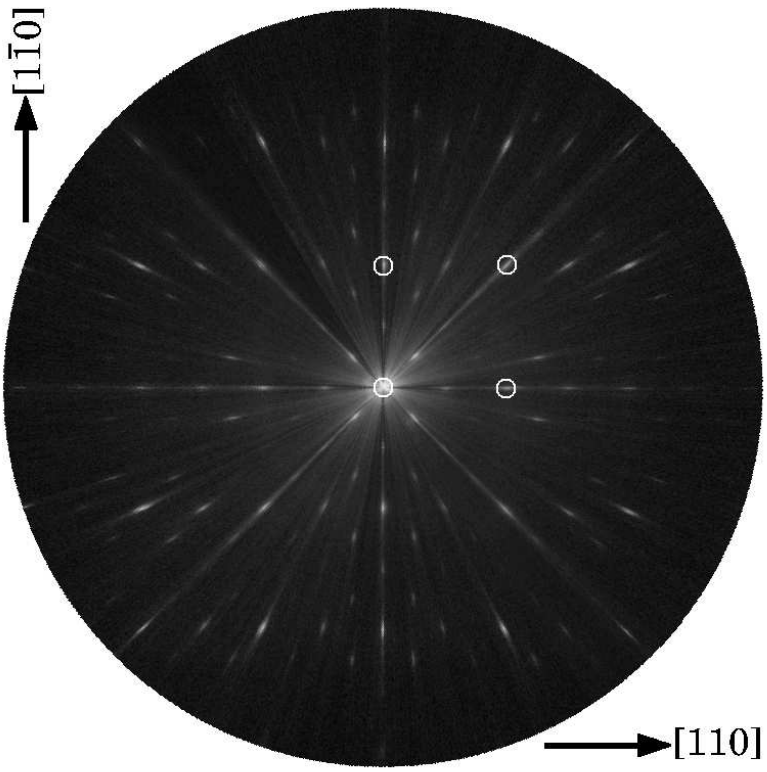

Figure 3.7: Azimuthal RHEED scan of the GaAs c(4×4) surface immediately before MnAs deposition. The corners of the surface unit cell are marked by circles.

area of the scans encompasses more than two diffraction orders of the surface unit cell in both directions.

3.3.3 Azimuthal scans during MnAs nucleation

In this section, we focus on a qualitative investigation of the nucleation phase of MnAs by RHEED azimuthal scans [73]. The azimuthal scans are recorded continuously without interrupting the MnAs growth. The MnAs nucleation starts on the c(4×4) reconstructed surface. The typical growth rate used in this study is around 0.36 nm/hour. This growth rate is achieved with a Mn cell temperature of 820 °C and an As cell temperature of 316 °C. The Mn and As molecular beams from two separate effusion cells are directed onto the substrate. The substrate temperature was maintained at 250 °C. The growth chamber pressure was maintained at 8.5×10^{-8} mbar. The resulting azimuthal scans during the nucleation of MnAs are shown in Figs. 3.8 to 3.12. All scans have the same orientation and size in reciprocal space. Since the RHEED intensities cover a significant dynamic range, the gray scale in the images are made nonlinear (Gamma correction) to reveal the weak structures close to the background level. This nonlinearity is identical for all patterns except Fig. 3.12, which is from a different sample. The RHEED intensity was constant except for an increase from 1.67 Amp to 1.72 Amp between Figs. 3.8 and 3.9. These scans were all acquired with the same sensor position on the RHEED screen and during a single growth run. This means that, since the cut is planar and parallel to the surface, the third index l is constant, for all scans except Figs. 3.9 (b) and (c), l=0.7±0.15. This l position is the geometrical value, without inner potential corrections. We divide the nucleation into distinct stages and will discuss them.

First stage (coverage < 0.3 ML) At the start of MnAs deposition, the c(4×4) reconstruction vanishes during the first 1/4 monolayer of deposited MnAs. This range is shown in Fig. 3.8. The diffuse background intensity remains practically unchanged. During this first stage (Fig. 3.8) with coverages below 0.3 ML (1 ML corresponds to 3.2Å), the c(4×4) surface reconstruction disappears and no additional reflections are observed. This could be caused by the Mn adatoms occupying completely random positions, producing an increased uniform diffuse background in the diffraction pattern. Another possibility is a coherent occupation of the Mn atoms on the same site within each (1×1) fundamental surface unit cell. This could take place without increasing the disorder and therefore the diffuse background intensity. The data in Fig. 3.8 compared to Fig. 3.7 do not show an increase of the background level within the accuracy of our measurement. The fact that the surface is crystalline and of high-quality further supports this assumption. At the end of this stage, only the integer order reflections of the fundamental surface unit cell remain [$(h\,k\,0.7)$, h, k integer]. The adsorption of Mn destroys the GaAs surface reconstruction since it obviously alters the surface energy.

Second stage (0.3 ML < coverage < 0.7 ML) When the coverage exceeds 0.3 ML (not shown), we observe the appearance of a spherical shell of diffuse intensity in reciprocal space that becomes strongest around a coverage of 0.7 ML (Fig. 3.9). However, since, we increased the electron beam intensity between the 0.13 ML and the 0.67 ML measurement to better resolve the background structure, the experimental data is not conclusive regarding the increase in diffuse background. Similar diffuse rings in the RHEED pattern

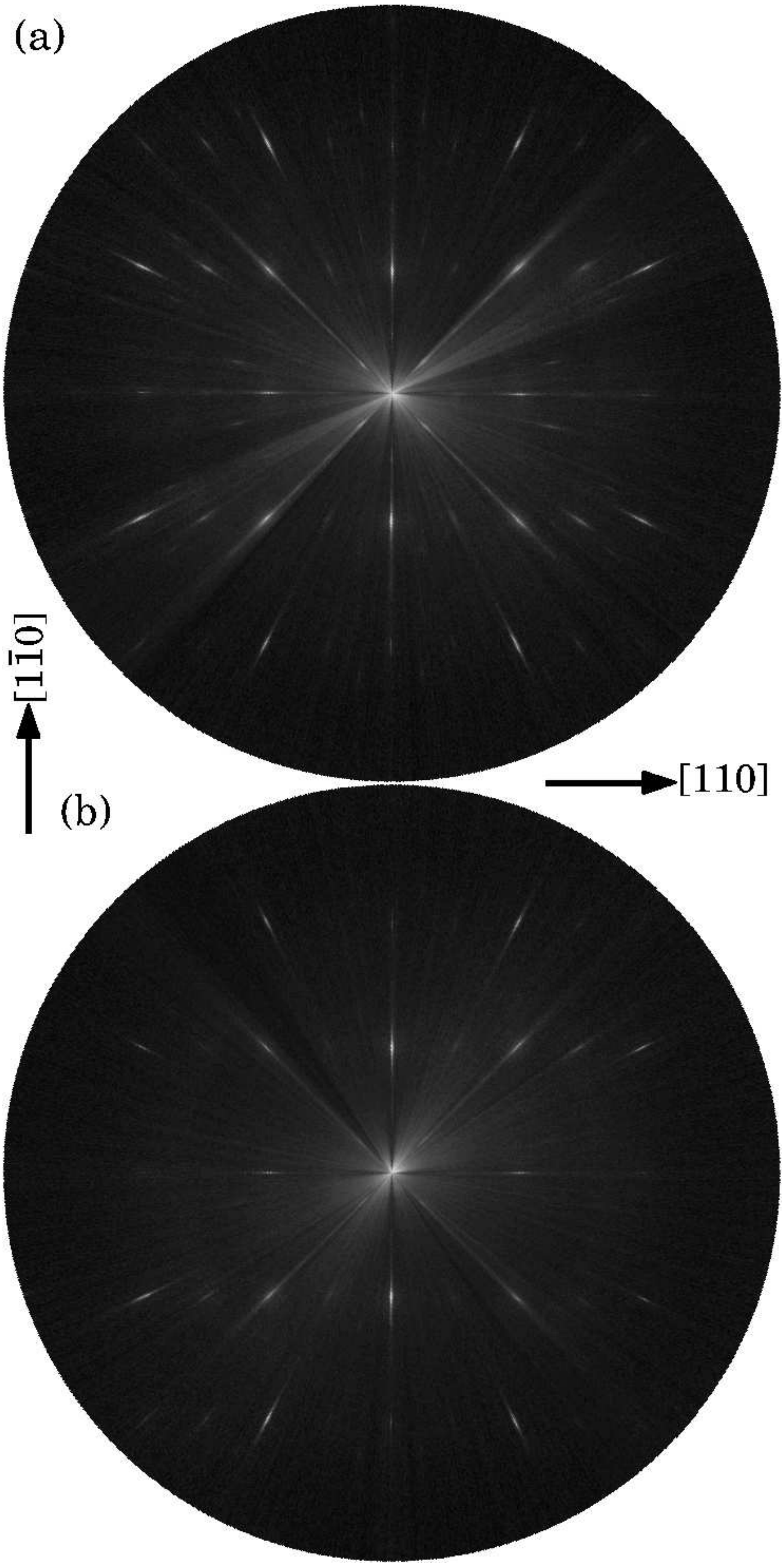

Figure 3.8: Azimuthal scans during deposition of MnAs at (a) 0.03±0.01 ML and (b) 0.13±0.02 ML coverage.

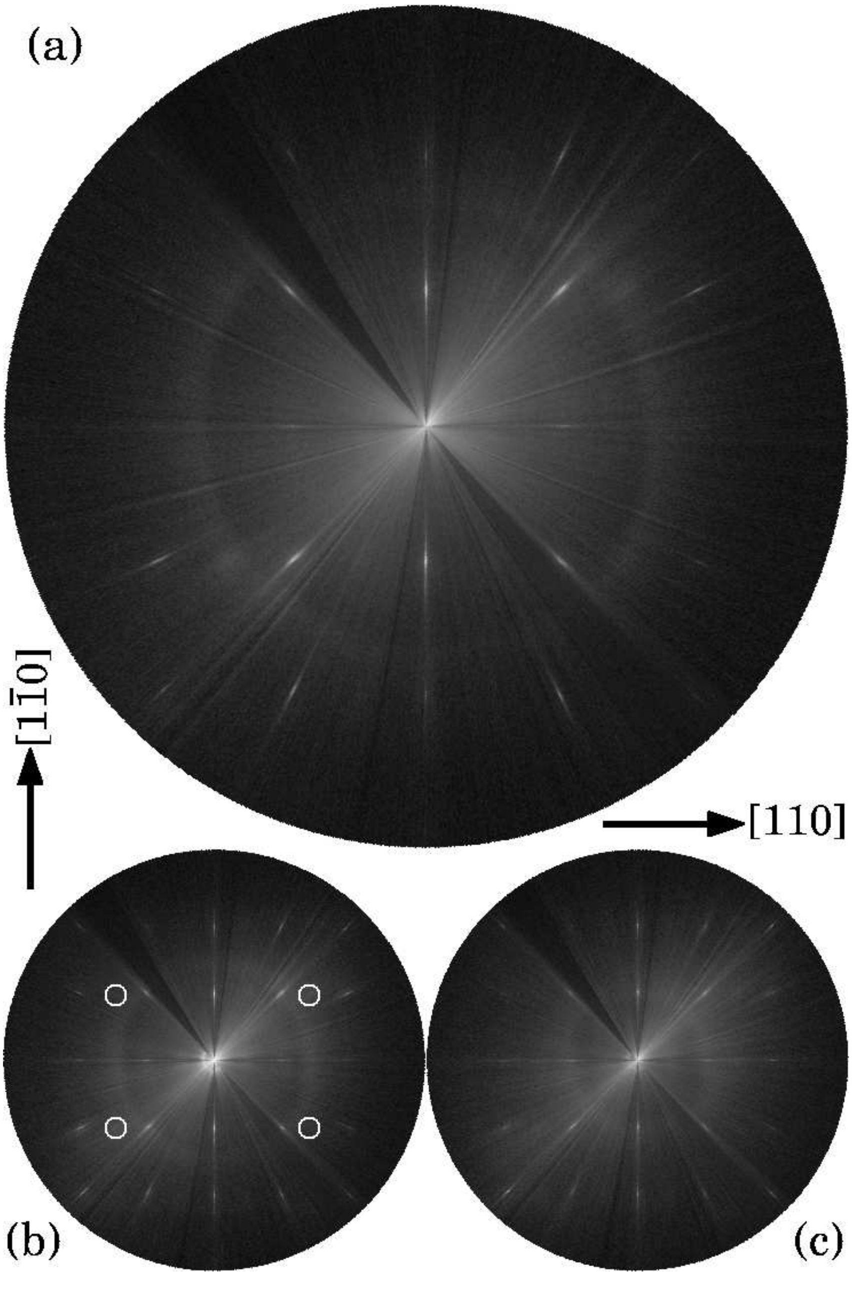

Figure 3.9: Azimuthal scan at a coverage of 0.67±0.07 ML coverage (a) plus two simultaneously acquired scans at l=1.1 (b) and l=1.5 (c). A spherical shell of diffuse intensity has developed. These scans are recorded during deposition of MnAs.

are observed during the initial stage of copper film growth on Si [74] and from carbon nanotubes [75]. The origin of such rings in the RHEED pattern can be understood if we consider that the film contains crystallites oriented in all possible orientations. For an individual crystal, the diffraction pattern is made up of reflections that are composed by the orientation of the crystal. While the actual position of the reciprocal lattice points in Fourier space depends on the crystal orientation, the distance of the lattice points from the origin does not. Therefore, if the crystal orientation is completely random, then for each diffraction spot there will be a corresponding sphere in the reciprocal space. In this case [Fig. 3.9], the radius of the sphere is $0.4\,\text{Å}^{-1}$, corresponding to a real-space distance of 2.5 Å. To demonstrate that the diffuse intensity is actually spherical, the azimuthal scans at two higher l values (1.1 and 1.5, again geometrical positions without potential correction) are shown in Fig. 3.9 (b) and (c).

The radius of the spherical shell is around 2.5 Å, in agreement with typical nearest-neighbor distances in MnAs [45]. Next-nearest neighbor distances (smaller distances in reciprocal space) are not observed. This is obviously the moment when the first MnAs bonds form and the coherent or random adsorption or binding of the Mn adatoms breaks down. Microscopically small units with random orientation and MnAs crystal spacing form. These could be Mn-As dimers or molecules with either a Mn or an As atom in the center and several As or Mn ligands. Since we are working with As overpressure and the Mn in MnAs has six nearest As neighbors in a octahedral environment [45], it is likely that these units may have more than one As bound to a Mn in a central position. The spherical diffuse intensity is almost uniform, and the growth conditions are such that we observe MnAs growth oscillations for thick layers [59], indicating good mobility of Mn adunits. We can therefore safely assume that either a part of such unit or the whole unit itself is mobile, at a minimum the unit interacts weakly with the periodic potential of the surface.

A closer look reveals the four weak non-integer reflections. These positions are marked in Fig. 3.9 (b). They are present in all scans in Fig. 3.9 independent of l at $(0.5\,2.5\,l)$ and its mirror-symmetric positions with respect to the $\langle 1\,1\,0\rangle$ axes. At the 90 ° rotated positions, this reflection is absent. The reflections have a distance close to 2.5 Å from the origin. This indicates i) that some fraction of the MnAs units are bound to the surface, presumably only weakly so, and that ii) in this case, only certain orientations are allowed. Obviously, the bonding of the adatom units already at this early stage is strongly directional, which is probably the reason why a single orientation of MnAs on GaAs (0 0 1) can be obtained when growing with a large As overpressure.

Third stage (0.7 ML < coverage < 1.1 ML) Increasing the coverage further, the spherical intensity vanishes and at coverages between 0.8 and 1.1 ML (Fig. 3.10), an fairly featureless diffraction pattern with a high and almost uniform diffuse background is observed. The scans for 0.78 and 1.13 ML coverage are shown in Figs. 3.10 (a) and (b), respectively. The weak reflections of Fig. 3.9 are still there, although in Fig. 3.10 (b) they have almost vanished in the background.

The increase in diffuse background intensity from Fig. 3.9 to Fig. 3.10 (a) is dramatic, considering that it is a change in coverage of only 16%. The change in coverage is the same as between panels (a) and (b) in Fig. 3.8, where no noticeable change was observed. The density of MnAs adunits on the surface is now high enough that the interaction with the substrate can no longer dominate its behavior. The high background level indicates

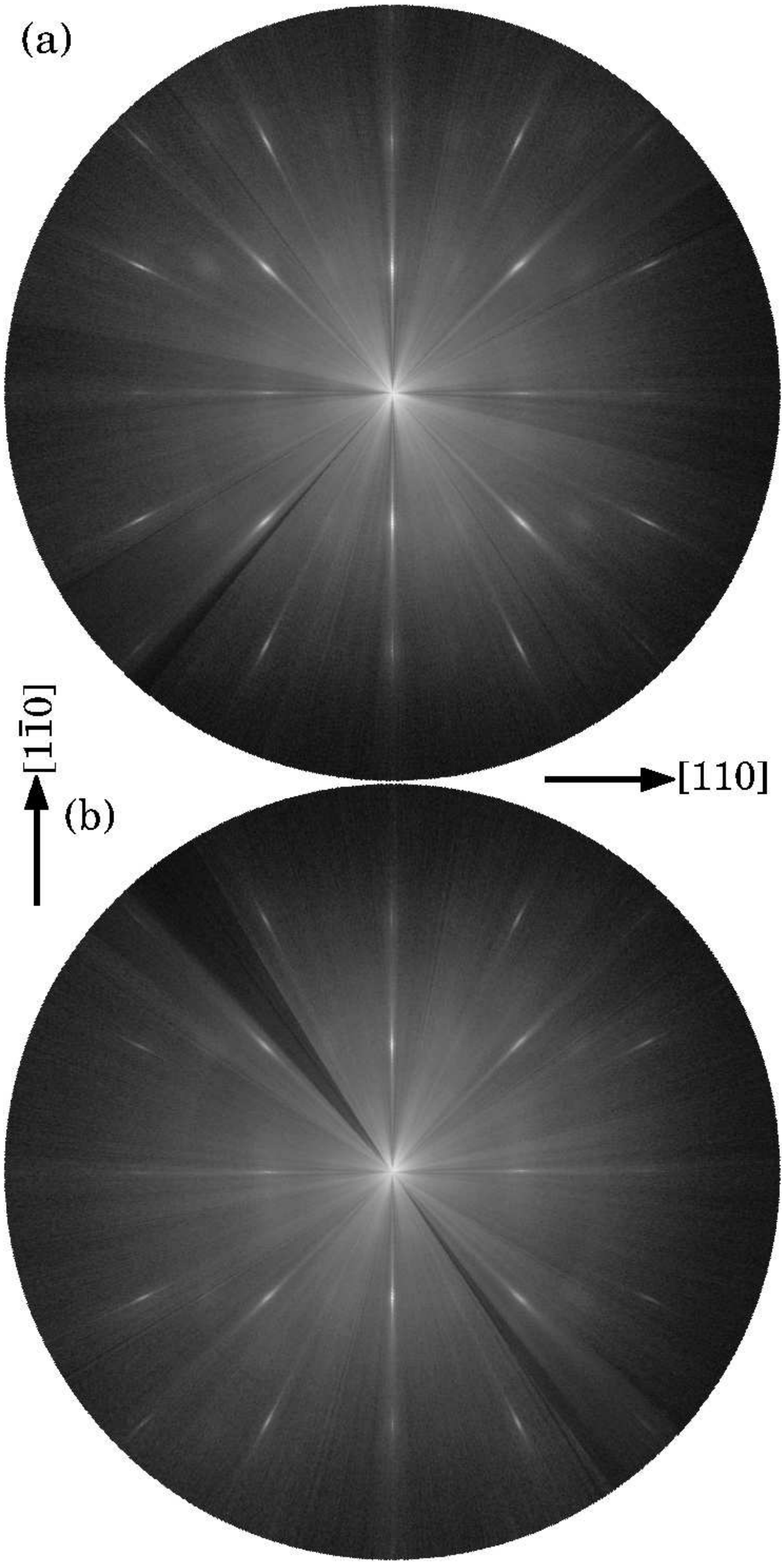

Figure 3.10: Azimuthal RHEED scans for 0.78±0.08 and 1.13±0.1 ML coverage during growth of MnAs. The spherical diffuse intensity has disappeared.

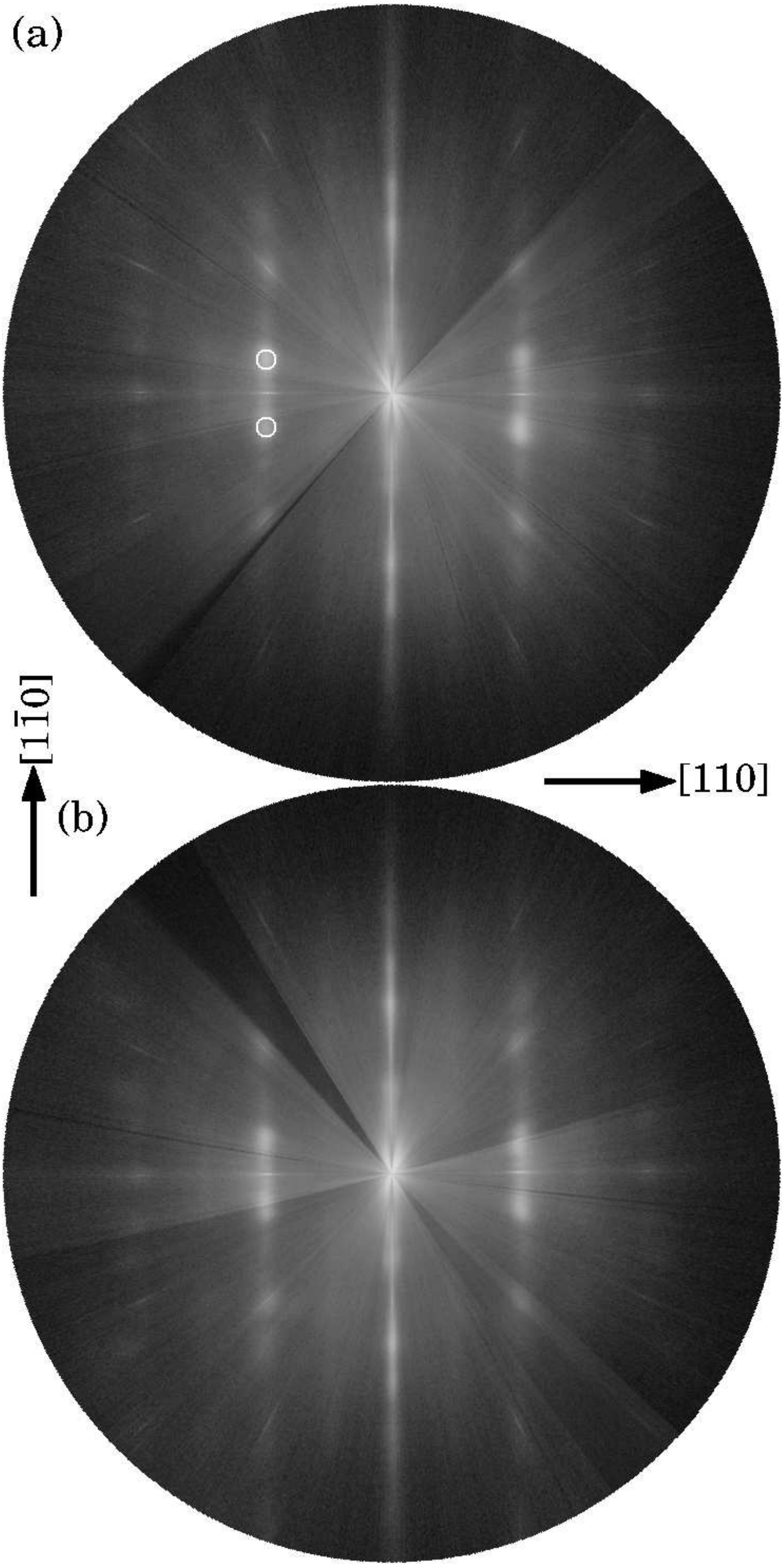

Figure 3.11: Azimuthal scans at 1.78±0.2 and 1.91±0.2 ML coverage during growth of MnAs. The patterns shows vertical diffuse bands through the integer order reflections and satellites above and below the $(n\,n)$ reflections, n integer. Two of these satellites are marked in (a) by circles.

a high random arrangement of the MnAs adunits, neither following the structure of the substrate nor assuming an independent MnAs structure. Presumably the MnAs that needs to coalesce into bigger units at such high coverage needs to comply with the neighboring MnAs units and the substrate over larger distances. At the end of this stage, some ordering along the $\langle 1\,1\,0\rangle$ directions seems to occur as the background starts to develop more intense bands along the square mesh connecting the integer order reflections. Note that although the coverage has changed by 45% the intensity of the diffuse background has not changed. The transition between stage 2 and stage 3 is therefore rather sudden, and stage 3 has a rather extended stability range.

Fourth stage (coverage> 1.7 ML) No data is available between 1.1 and 1.8 ML. At 1.78 ML coverage (Fig. 3.11), another significant redistribution of the diffracted intensity has taken place. We now see relatively strong bands of intensity running along $[1\,\bar{1}\,0]$ through the integer order reflections. Until 1.91 ML coverage, this pattern remains practically unchanged, as can be seen from the comparison of Figs. 3.11 (a) and (b).

At 1.8 and 1.9 ML, again a different arrangement is present (Fig. 3.11). The intensity around the Bragg reflections is not confined, rather it is distributed in reciprocal space. Now the diffraction pattern is dominated by diffuse bands running along the $[1\,\bar{1}\,0]$ direction. These bands are already quite narrow in the perpendicular $[1\,1\,0]$ direction. This indicates that along the $[1\,\bar{1}\,0]$ direction the film is loosely connected and a continuous variation of lattice spacings are present in the film. The epitaxial ordering therefore happens in a two-stage process. In the current stage, the epitaxial lock-in only takes place along $[1\,1\,0]$, while along $[1\,\bar{1}\,0]$, the order is still quite weak. The $(n\,n)$ reflections (n integer) develop satellites marked by the circles that correspond to a real-space distance of around 14 Å, approximately three times the substrate periodicity in this direction. This 14 Å distance can be associated with a weak short-range order as the satellites are quite broad and only the first order is observed. Relatively suddenly, around 2 ML coverage (Fig. 3.12), long-range epitaxial order along the orthogonal $[1\,\bar{1}\,0]$ is established as well. This anisotropy is not too surprising in view of our TEM [67] and x-ray results [76, 77] that show a strong interaction between film and substrate with periodic misfit dislocations along $[1\,1\,0]$ and a very weak interaction with small strain variation at the interface along $[1\,\bar{1}\,0]$. The threshold for epitaxial lock-in is therefore reached earlier along the direction with the strong substrate-layer interaction.

Past 2.1 ML nominal thickness, the final structure of the film is reached with the well-established single-phase epitaxial relationship $[0\,0\,0\,1]_{\mathrm{MnAs}} \parallel [1\,\bar{1}\,0]_{\mathrm{GaAs}}$ and $[1\,1\,\bar{2}\,0]_{\mathrm{MnAs}} \parallel [1\,1\,0]_{\mathrm{GaAs}}$. The single phase heteroepitaxial orientation can be verified by an azimuthal scan of a thicker sample such as the one shown in Fig. 3.12 (b) with around 6.5 ML nominal coverage. The presence of surface reconstruction spots along the $[1\,1\,0]$ direction indicates the 2×1 reconstructed surface for the MnAs film.

It is worth to compare our *in situ* results with scanning tunneling microscopy (STM) data from the same heteroepitaxial system [78]. In this study, the surface was quenched to room temperature at various stages of the deposition and investigated under ultrahigh vacuum conditions. Bulk MnAs undergoes two structural phase transitions in this temperature range, so the results may not be directly comparable. Also, the MnAs deposition rate was significantly higher than the 0.36 nm/hour used here. At 0.4 ML coverage, the STM shows small, two-dimensional islands up to 30 Å in size. At 1.5 ML coverage, the islands are still disconnected and three-dimensional with an average size of 100 Å. At 5.5 ML

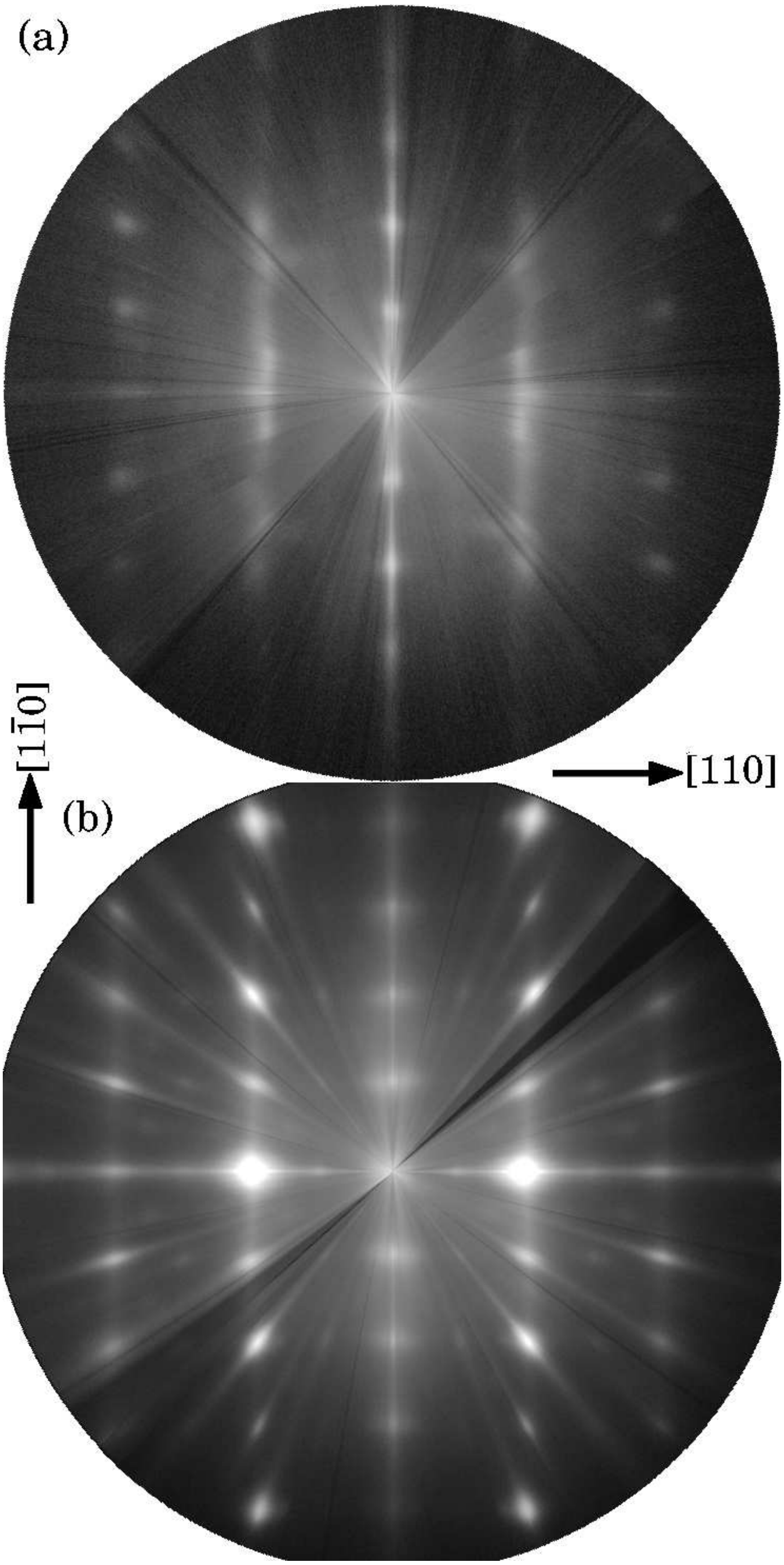

Figure 3.12: Azimuthal scans at 2.09±0.2 ML coverage during deposition of MnAs and from a 6.4±0.7 ML thick MnAs film. At around 2 ML, the film assumes its final epitaxial structure and orientation.

coverage, the islands begin to coalesce and form a closed film. If we assume that the film follows the same morphology during deposition in our case, this would mean that the ordering we see in diffraction patterns for coverages of more than 1 ML is occurring in the growing mounds. On one hand, the sharp GaAs (1×1) reflections are still visible at 2 ML nominal coverage [Fig. 3.12 (a)], implying that they are still within reach of the RHEED beam that is very surface sensitive and does not sample more than the top 2-3 ML of a flat surface. On the other hand, the layer reflections are always wider than what would be expected for finite size effect limited scattering with the droplet or island sizes inferred from STM. This implies that the domain sizes we see in the azimuthal scans for any film structure are smaller than the mound sizes. Our result is not in disagreement with the observed surface morphology. Thirdly, we do not observe chevrons in RHEED, the typical sign of crystalline, faceted mounds present on the surface. For the heteroepitaxial system InAs on GaAs (0 0 1), these form e.g. at critical thicknesses between 1.6 and 2.0 ML [79]. Here, there are no crystalline, facetted mounds at the growth temperature. If there are mounds, they are presumably disordered and ductile enough to reorder up to a nominal thickness of 2 ML. Our measurements therefore monitor processes within the islands or mounds forming around 1 ML nominal coverage. Since these are significantly higher than a single ML, the observed results imply a rearrangement in the volume of the mounds, contrary to the general assumption that only surface adatoms can migrate. The results of the present study indicate that it takes up to an average coverage of 2 ML of MnAs until the interface is stable and a two-dimensional epitaxial relationship is established.

The static RHEED patterns along MnAs [1 1 $\bar{2}$ 0] and MnAs [0 0 0 1] are shown in Fig. 3.13. These patterns are taken after the film has attained the final thickness of about 7 ML. This shows the direct comparison between the azimuthal scan Fig. 3.12 (b) and the static RHEED pattern. The 2×1 reconstructed MnAs surface is clearly seen in both cases. In Fig. 3.13 (a), the electron beam is parallel to the GaAs [1 $\bar{1}$ 0] direction, in Fig. 3.13 (b) the electron beam is parallel to the [1 1 0] direction. The arrows in Fig. 3.13 (a) mark the half-order streaks along the 2× direction. The lattice constant of the hexagonal MnAs unit cell as determined from the RHEED patterns is 5.8±0.5Å along the [0 0 0 1] direction and 3.8±0.5Å along the [1 1 $\bar{2}$ 0] direction, which is in agreement with the *in situ* GID measurements.

The epitaxial geometry of the film obtained from the RHEED azimuthal scans is shown in Fig. 3.14. The hexagonal MnAs grows with its MnAs (1 $\bar{1}$ 0 0) prism plane parallel to the GaAs (0 0 1) planes. The [0 0 0 1] direction of the hexagonal MnAs unit cell is aligned with the [1 $\bar{1}$ 0] direction of the GaAs substrate.

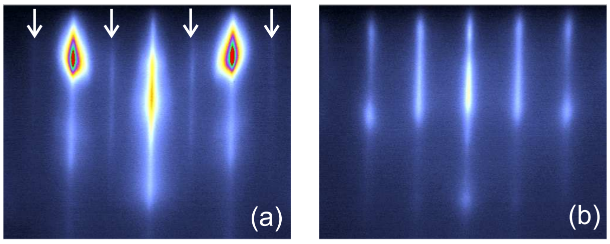

Figure 3.13: RHEED patterns of a MnAs film after growth showing a 1×2 surface reconstruction. (a) e-beam along the [0 0 0 1] direction, (b) e-beam along [1 1 $\bar{2}$ 0]. Arrows indicate the half-order streaks along the 2× direction.

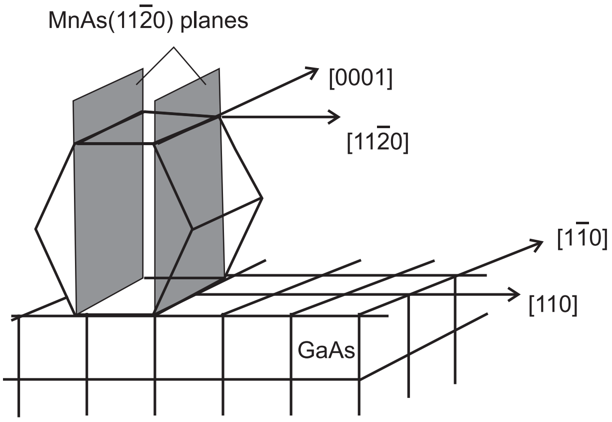

Figure 3.14: Epitaxial relationship of hexagonal MnAs on GaAs. Shadowed planes represent the MnAs (1 1 $\bar{2}$ 0) planes perpendicular to the GaAs (0 0 1) surface

3.4 *In situ* x-ray diffraction during growth

Grazing incidence x-ray diffraction, directly probes the lattice spacing parallel to the interface. Therefore, it measures the strain directly. The MnAs (1 1 $\bar{2}$ 0) planes (gray in Fig. 3.14) and GaAs (2 2 0) planes were chosen as the diffraction planes. These planes offer the advantage that the MnAs (1 1 $\bar{2}$ 0) and GaAs (2 2 0) planes are parallel to each other and both perpendicular to the surface. Hence, signals from both the planes can be

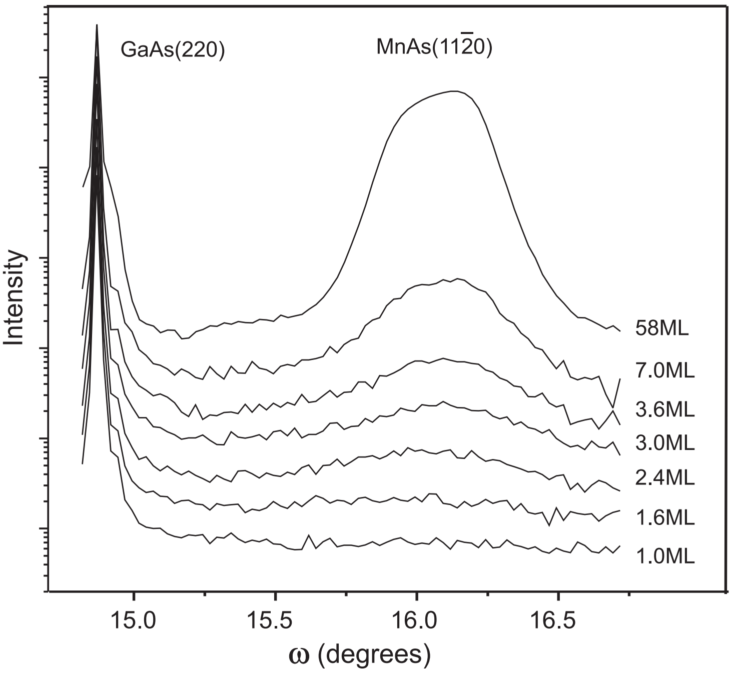

Figure 3.15: X-ray diffraction curves ($\omega/2\Theta$ scans) measured at a substrate temperature of 250 °C along GaAs [1 1 0] with the GaAs (2 2 0) substrate and the MnAs (1 1 $\bar{2}$ 0) layer reflections during the growth of the MnAs film. The approximate nominal layer thickness is indicated at the right. Both the position and the half width of the MnAs (1 1 $\bar{2}$ 0) peak change with layer thickness. For clarity, the curves are shifted vertically.

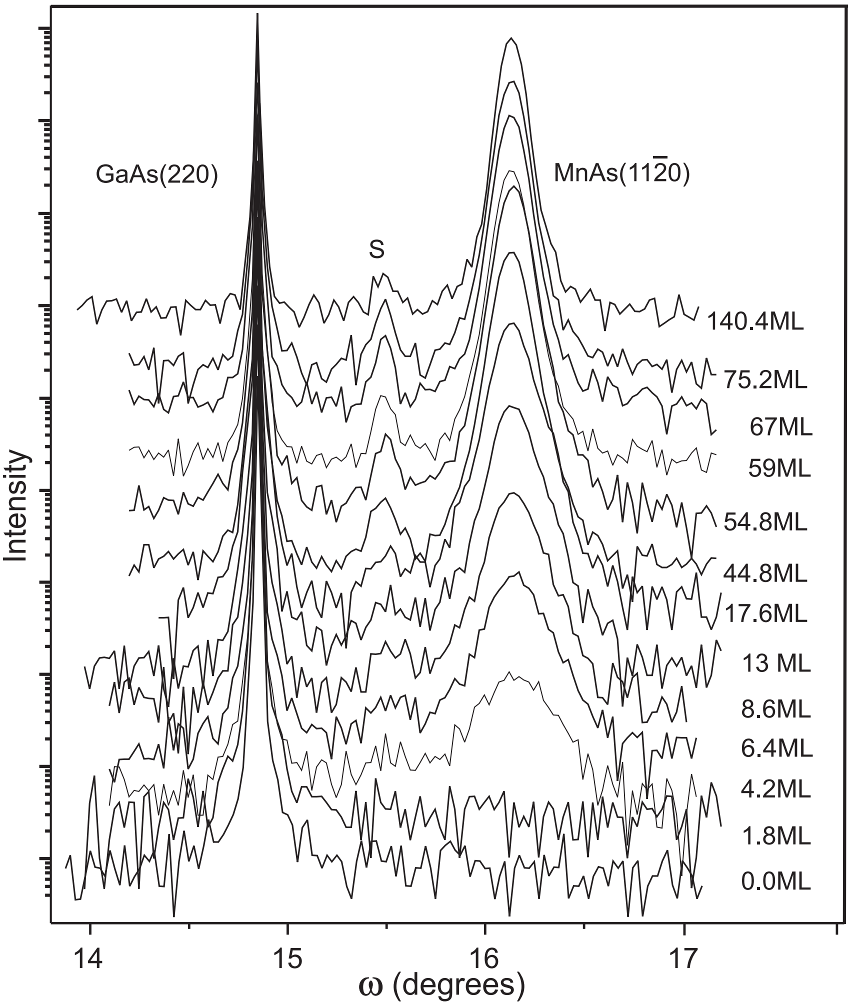

Figure 3.16: X-ray diffraction curve ($\omega/2\Theta$ scans) measured *in situ* at the substrate temperature of 250 °C during growth along the GaAs [1 1 0] direction with the GaAs (2 2 0) substrate and the MnAs (1 1 $\bar{2}$ 0) layer reflections. The deposited number of monolayers is indicated at the right of each scan. For clarity, the curves are shifted vertically.

obtained in a single radial scan along the [1 1 0] substrate direction. The high brilliance of the synchrotron x-rays used in this study provides monolayer sensitivity. The energy of the x-rays used was 12 keV. The critical angle for total external reflection of MnAs for this energy is 0.23°. The results obtained for two samples with lower growth rate (sample A) and higher growth rate (sample B) are discussed below.

Figure 3.15 and Fig. 3.16 present the $\omega/2\Theta$ scans recorded during the growth of MnAs on GaAs (0 0 1) with a growth rate of about 0.36 nm/hour (sample A) and 6 nm/hour (sample B). For sample A the grazing incidence angle was kept at 0.2 °, close to the critical angle for total external reflection α_c for GaAs, for maximum surface sensitivity. The grazing incidence angle for sample B was increased with increasing film thickness from 0.2 ° to 0.3 °, to achieve maximum sensitivity from the interface. The signal from MnAs (1 1 $\bar{2}$ 0) planes is already detected at a nominal film thickness of about 2.4 ML (sample A) or 4.2 ML (sample B). At this thickness, epitaxial MnAs crystallites form. The epitaxial relationship found from the RHEED and GID measurement is as follows:

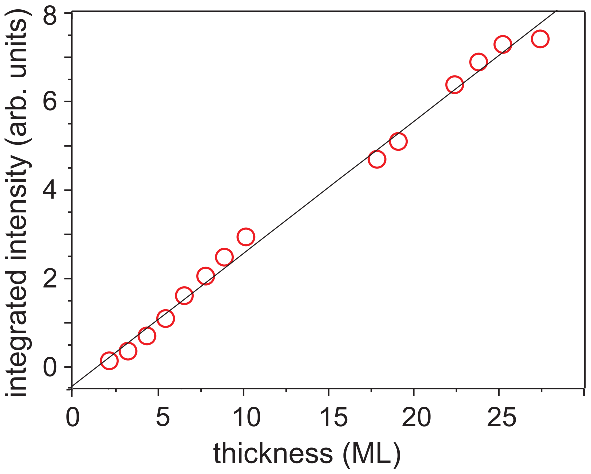

Figure 3.17: Evolution of integrated intensity of the MnAs $(1\,1\,\bar{2}\,0)$ peak as a function of layer thickness for sample B (high growth rate). The solid line is a linear fit to the measured data.

$$\begin{aligned}\text{MnAs}\,[1\,1\,\bar{2}\,0] &\parallel \text{GaAs}\,[1\,1\,0]\\ \text{MnAs}\,[0\,0\,0\,1] &\parallel \text{GaAs}\,[1\,\bar{1}\,0]\\ \text{MnAs}\,[1\,\bar{1}\,0\,0] &\parallel \text{GaAs}\,[0\,0\,1]\end{aligned}$$

With increasing layer thickness, the integrated intensity, which is directly proportional to the amount of deposited material in kinematical theory, increases approximately linearly with the layer thickness for both sample A and B. The integrated intensity as a function of layer thickness for sample B is shown in Fig. 3.17. This demonstrates that the growth proceeds smoothly with a uniform rate. Therefore, the thickness and growth rate can be directly calibrated with sufficient accuracy. Let us first discuss the thickness measurements of these layers and then return to the strain evolution as a function of thickness.

3.4.1 Thickness determination from x-ray reflectivity

The sample thickness was determined from *ex situ* specular x-ray reflectivity measurements. The x-ray reflectivity (XRR) measurements were done using a PANalytical X'Pert diffractometer system with a Ge $(2\,2\,0)$ hybrid monochromator and a 0.18° receiving slit using CuKα_1 radiation. The sample was mounted on the vertical sample stage which is installed on a high resolution goniometer. By repeatedly adjusting the z (penetration of sample in the beam) and ω (tilt of the sample with respect to the x-ray beam), an optimum position was obtained in which the sample is located at the center of the x-ray beam and only half of the x-ray beam was detected by the detector. The measured specular reflectivity curve (circles) for sample B along with the simulated profile (continuous line) is shown in Fig. 3.18. The simulation is based on the well established iterative scheme for analyzing specular reflectivity from a stack of different layers, developed by Parratt in the 1950s [80] by generalizing methods used in optics [81]. As the reflectivity measurement is done *ex situ* after exposing the sample to air for more than an hour, a layer of porous oxide (Mn_3O_4 or Mn_2O or MnO) has formed on the sample. The reflectivity simulation therefore takes into account the density and thickness of the continuous MnAs layer and an oxide layer on top of it. The roughness at the three interfaces, (substrate–film, film–oxide,

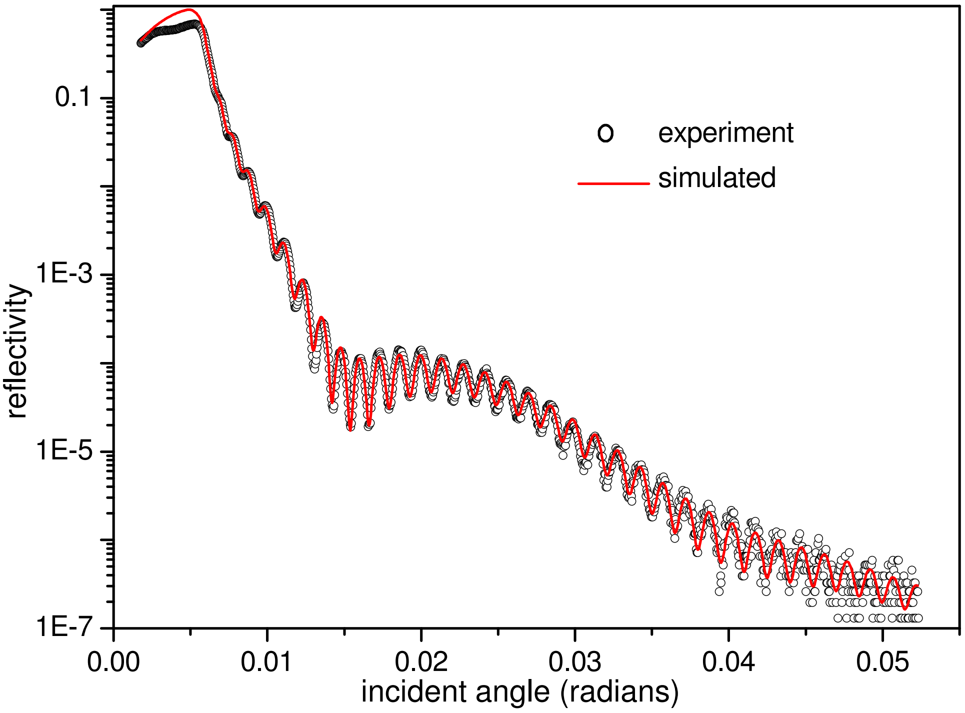

Figure 3.18: Specular reflectivity curve for MnAs films grown on GaAs (0 0 1) (sample B). The open circles show the measured data and the continuous line represents the simulated curve. The thickness of the MnAs film is determined to 51.2 nm.

oxide–vacuum) is modelled by graded intermediate layers. The best fit to the measured reflectivity curve is obtained for a MnAs film thickness of 51.2 nm with a roughness of 0.4 ±0.1 nm at the MnAs–substrate interface. The top oxide layer, probably Mn_3O_4, is found to be 2.3 nm thick, with a roughness of 0.3 ±0.1 nm between MnAs and the oxide. The roughness of the oxide-vacuum interface is found to be 0.75 ±0.1 nm. From the thickness of the MnAs layer we can determine the growth rate, which was constant throughout the deposition. We estimate a 2% error in thickness measurement. The thickness for sample A is determined to be 20 nm. The prominent x-ray oscillations seen in the reflectivity measurement indicate a smooth and abrupt interface between MnAs/GaAs.

3.4.2 Evolution of strain in the layer

The MnAs $(1\,1\,\bar{2}\,0)$ peaks shown in Fig. 3.15 and Fig. 3.16 are well fitted with a Gaussian function and we calculate the in-plane lattice parameter a from the peak position. The GaAs $(2\,\bar{2}\,0)$ peak is taken as a reference to calculate the Bragg angle (θ_B) of the MnAs peak in each scan. The in-plane lattice parameter is calculated according to the formula

$$d_{hk[-(h+k)]l} = \sqrt{\frac{3}{4\{\frac{h^2+hk+k^2}{a^2} + \frac{3l^2}{c^2}\}}}\,. \tag{3.4}$$

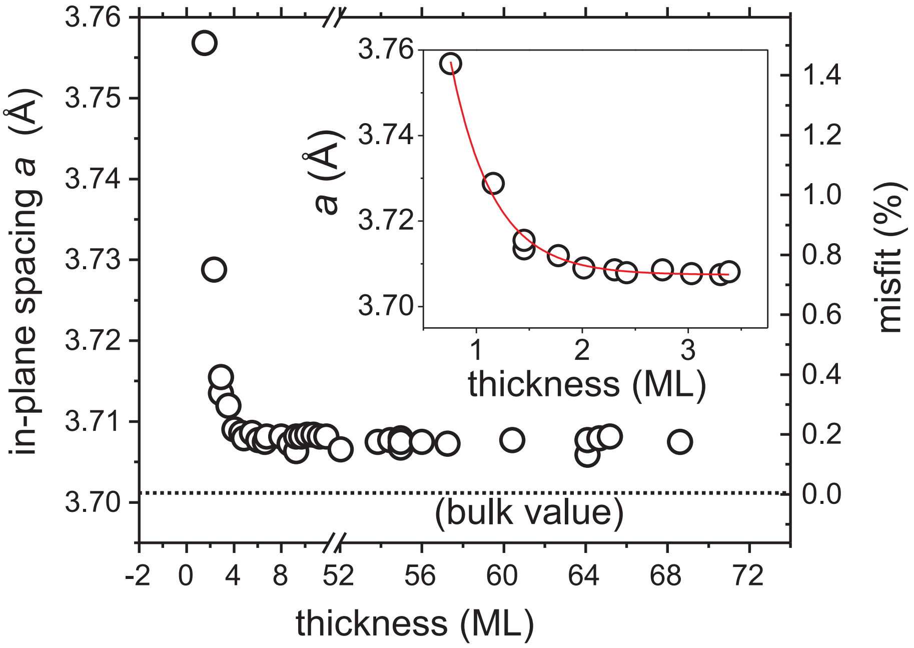

Figure 3.19: Lattice parameter a as a function of the thickness of the growing MnAs layer (sample A). The line fitted to the data is an exponential decay function. The insert presents an enlarged plot of the initial phase of the growth. Growth rate is 0.36 nm/hour.

The spacing for MnAs $(1\,1\,\bar{2}\,0)$ planes is $d_{1\,1\,\bar{2}\,0} = a/2$. Substituting the value of $d_{11\bar{2}0}$ in Bragg's equation, $2d_{11\bar{2}0}\sin\theta_B = \lambda$, we get the formula for the in-plane lattice parameter a,

$$a = \frac{\lambda}{\sin\theta_B}\,, \tag{3.5}$$

where λ is the wavelength of the x-rays, λ=1.03317 Å for our measurements. The evolution of the in-plane lattice parameter as a function of thickness (determined from x-ray reflectivity measurement) is shown in Fig. 3.19 for sample A (grown with lower growth rate) and for sample B (grown with higher growth rate) in Fig. 3.20. Two different types of relaxation behavior are clearly observed depending on the growth rate. For the lower growth rate case, the lattice is under tensile strain during the nucleation of the layer. A net 1.2% relaxation is observed upon increase in thickness. A continuous decrease of the lattice parameter towards the bulk value is seen up to a thickness of about 8 ML. Very little change is observed with further increase in layer thickness. However, the lattice is not completely relaxed. About 0.2% of tensile strain remains even at a thickness of 70 ML.

The growth experiment with about 15 times higher growth rate provided only short time windows to record *in situ* x-ray profiles during growth. Therefore, we observe the first MnAs peak at a nominal layer thickness of 4.2 ML and the corresponding in-plane lattice parameter is 3.690 Å. The first observed value for the in-plane lattice spacing a, is already quite close to the bulk value of MnAs at the growth temperature of 250 °C i.e. 3.701 Å [46]. The interesting point is that the lattice is compressively strained (0.3%) unlike the tensile strain observed for the lower growth rate case. A 0.1% relaxation of the in-plane lattice spacing is observable upon further growth. A compressive strain of 0.2% remains in the layer even at a thickness of 159 ML. In conclusion, a different relaxation

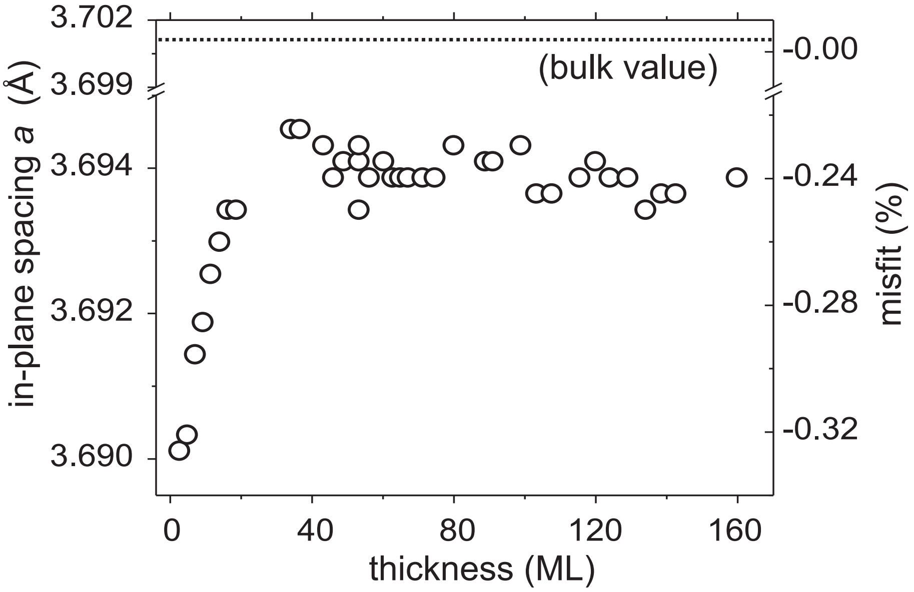

Figure 3.20: Evolution of the in-plane lattice parameter a with the thickness of the MnAs film (sample B). After an initial fast relaxation, no further relaxation is seen. Growth rate is 6 nm/hour.

process is seen depending upon the growth rate.

The dependence of the relaxation process upon growth time is shown in Fig. 3.21. We find, although the initial lattice parameters and relaxation mechanisms are different for different growth rates, the time needed for relaxation is the same. At the same time, both samples show the same absolute misfit of ±0.2%. Since both samples are grown at the same temperature, this indicates that the relaxation process is thermally activated [82]. The speed of relaxation is determined by the substrate temperature.

The GaAs $(2\,2\,0)$ plane spacing (1.99 Å) is larger than the MnAs $(1\,1\,\bar{2}\,0)$ plane spacing. Therefore, in epitaxy tensile strain is expected for MnAs films, as seen for the lower growth rate case. However, we see a 0.3% compressive strain in the MnAs layer at the onset of growth for the sample grown with higher growth rate. Two possible explanations for this phenomenon can be thought of. First, it can be explained, at least partially, by the curvature of the island surface. The surface energy γ gives rise to the stress $P{=}\gamma/R$, where R is the radius of the island. Then the strain is $\varepsilon = \gamma/ER$, where E is the Young modulus. Taking a typical surface energy of a metal, $\gamma = 1.5$ J m^{-2}, the Young modulus of MnAs $E = 0.7 \times 10^{11}$ J m^{-3} [83] and an island radius $R = 10$ nm, we obtain $\varepsilon{=}0.2\%$. The surface energy is thus partially responsible for this compression of the MnAs islands. Second, the higher growth rate is achieved by increasing the Mn flux during growth [82]. This may also lead to a slight change in the layer stoichiometry resulting in the smaller in-plane lattice parameter.

3.4.3 Evolution of in-plane grain size

As seen from the time evolution of the MnAs $(1\,1\,\bar{2}\,0)$ peak in Figs. 3.15 and 3.16, upon further growth, the integrated intensity of the MnAs film peak increases and the full width at half maximum (FWHM) of the peak decreases. This indicates an increase in in-plane grain size during growth. The in-plane grain size is measured from the FWHM of the

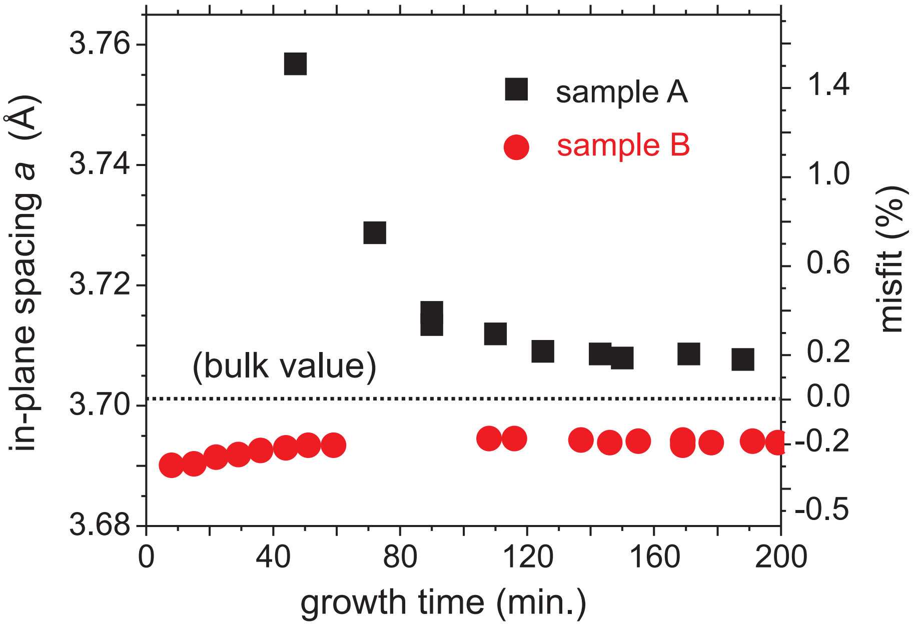

Figure 3.21: The measure of in-plane lattice constant a, as a function of the growth time for high and low growth rates.

MnAs peaks along two perpendicular in-plane directions during growth and *ex situ* after growth along the out-of-plane direction using Scherrer's formula [11]:

$$\tau = K \frac{\lambda}{h \times \cos \theta_B}. \tag{3.6}$$

Here, τ is the in-plane grain size (correlation length), K is a constant close to unity, h is the FWHM of the MnAs $(1\,1\,\bar{2}\,0)$ peak, λ is the wavelength of x-rays and θ_B the Bragg angle. The evolution of the in-plane grain size along the MnAs $[1\,1\,\bar{2}\,0]$ direction is shown in Fig. 3.22. We found that the in-plane grain size increases continuously with thickness. This increase in grain size indicates that the crystallinity of the film is enhanced with thickness. Along the MnAs $[1\,1\,\bar{2}\,0]$ direction, it reaches ~27 nm at a layer thickness of about 160 ML. The increase of the in-plane grain size can be subdivided into two different regimes, i.e. a regime of faster increase and a slower increase. The individual linear fit to these regimes (shown as dotted lines in Fig. 3.22) clearly shows different slopes. We conclude that after an initial fast stage, the in-plane grain size increases with a slower rate after a thickness of about 20 ML. This indicates that coalescence of 3-dimensional islands occurs at a thickness of 20 ML. This behavior can be well fitted with a sum of two exponential functions. Along the MnAs $[0\,0\,0\,1]$ direction, the grain size reaches a final value of ~32 nm. In the out-of-plane direction, the grain size reaches a value of about 50 nm.

3.5 Discussion

Here we combine the results presented in the last two sections from RHEED and *in situ* x-ray measurements during growth to provide a complete picture of the growth mecha-

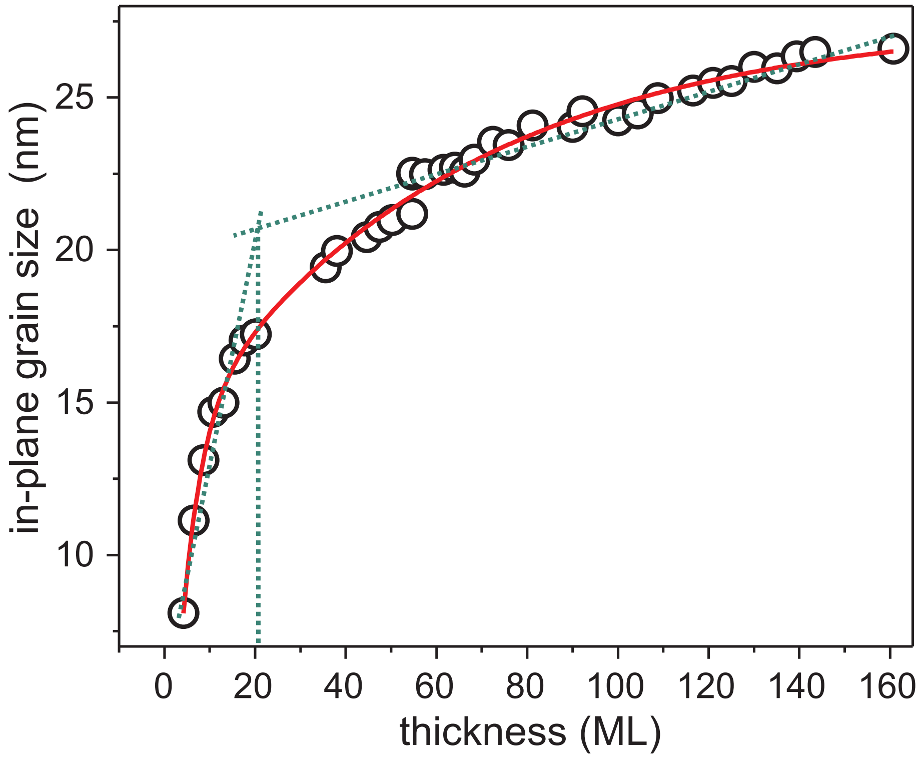

Figure 3.22: Evolution of in-plane grain size starting from the beginning of the growth up to a final thickness of 160 ML (sample B). The solid line fitted to the data is a sum of two exponential growth function. The dotted lines are linear fits to the data in the fast and slow increase regime. The coalescence is seen at a thickness of 20 ML. The sample is grown with a growth rate of 6 nm/hour.

nism of MnAs on GaAs. Our x-ray diffraction method is not sensitive to first three stages of nucleation seen below 2 ML. Therefore we study the microscopic nucleation process by RHEED, and the coarsening of the islands and the evolution of strain by GID. Our RHEED measurements reveal two interesting phenomena present during the nucleation of the (hexagonal) metal MnAs on the (cubic) semiconductor GaAs (0 0 1). A coherent adsorption of Mn adatoms is seen up to a coverage of 0.3 ML. At coverages between 0.3 and 1 ML, randomly oriented structures with the nearest neighbor distance of MnAs form that evolve into a completely disordered state with neither the film nor the substrate periodicity. Out of this disordered state, the epitaxial lock-in of the layer structure happens in two stages. It occurs first along the [1 1 0] direction, in which there is a strong interaction between film and substrate, and finally in the orthogonal $[1\,\bar{1}\,0]$ direction at a nominal coverage of 2 ML.

The relaxed MnAs $(1\,1\,\bar{2}\,0)$ peak appears at the high-angle side of the substrate peak already at a thickness of 2.4 ML (Fig. 3.15) in sample A (low growth rate) or 4.2 ML as shown in Fig. 3.16 for sample B (high growth rate) after the formation of the hexagonal MnAs crystal structure. In the high growth rate case, most probably the hexagonal MnAs has formed at a nominal thickness of about 2.5 ML, but is not observed due to the small time window allowed for the *in situ* measurements. The appearance of the peak indicates that relaxed three-dimensional MnAs islands are formed on the surface at a minimum thickness of 2.5 ML. This is consistent with the RHEED observation, which reveals the formation of hexagonal MnAs at a thickness of about 2.1 ML. The question arises how the film grows until 2.1 ML. Does the absence of MnAs peak until 2.5 ML in the XRD profiles mean that MnAs is growing coherently? Put it in another way, does a wetting layer form first ? This question can be answered from the experimental findings in several ways. First, the absence of the MnAs peak until 2.5 ML shows that at least a wetting layer of hexagonal MnAs is not formed. Second, we do not see any broadening of the substrate reflection in the course of growth until 2.5 ML (see Fig. 3.16). The incidence angle for the x-ray beam of 0.2° (the critical angle for GaAs at 12 keV is 0.203°) minimizes the penetration depth of x-rays into the substrate lattice, and therefore increases the possibility of detecting the small broadening effects. Broadening (although small) of the GaAs (2 2 0) substrate reflection is expected either for the pseudomorphic growth of highly strained 2 ML of MnAs film or for the formation of strained islands on top of the GaAs (0 0 1) substrates. Hence, the first two experimental observations show that neither relaxed nor strained MnAs nor a complete layer is formed. Another strong evidence supporting this is the formation of a diffuse ring in the RHEED azimuthal scan at a nominal layer thickness of 0.67 ML (see Fig. 3.9). This clearly indicates the formation of randomly oriented adunits with some unknown stoichiometry. At this stage the epitaxial orientation is not imposed on these adunits by the substrate.

The initial weak increase of diffuse intensity below a coverage of 0.3 ML (Fig. 3.8) is indicative of a coherent adsorption or binding of the Mn adatoms during these early stages of growth. This would correspond to an initial wetting behavior of the surface. The STM studies [78] and indicative of Volmer-Weber type of nucleation and the GID studies at the later stage of growth are consistent with this interpretation. Therefore, we conclude that the growth of MnAs contains elements of both Stranski-Krastanov and Volmer-Weber growth mode.

We calculate the critical thickness at which the formation of dislocations is energetically favorable under thermodynamic equilibrium conditions using the Matthews Blakeslee model [84, 85]. In this model, the critical thickness h_c is calculated as,

$$h_c = \frac{b(1-\nu\cos^2\theta)}{8\pi(1+\nu)\varepsilon\cos\varphi}\ln(\frac{\alpha h_c}{b}) \,, \tag{3.7}$$

where $\mathbf{b}$ is the Burgers vector of the dislocation, φ is the angle between b and the normal to the dislocation line in the interface (0° for the edge dislocations), θ is the angle between the line direction and b of the dislocation (90° for the interfacial misfit dislocations), α is the core energy per dislocation (it is generally estimated to be 0.5 to 1 in the case of metals), ν is the Poission ratio, and ε is the linear strain between the epilayer and the substrate. The critical thickness calculated according to this model using reasonable estimates for the parameters is 1.6 ML. The experimental observation of the first MnAs at a thickness of 2.5 ML is at a higher value than that predicted by the model. Only small relaxations of 0.1% and 1% are noticed upon further growth until 159 ML as shown in Figs. 3.19 and 3.20, respectively. A satellite reflection between the substrate peak and the layer peak (denoted by "S" in Fig. 3.16) already appears at a nominal layer thickness of about 6 ML. As will be discussed in chapter 5, this peak indicates the formation of a regular array of misfit dislocations at the interface. The islands are relaxed by the introduction of misfit dislocations during their nucleation. The misfit dislocations are introduced directly at the interface during the growth of islands before coalescence.

3.6 Epitaxial orientations of MnAs

In this section, we present quantitative investigations regarding the presence of different orientations of MnAs in a single film. The MnAs epitaxial films on GaAs (001) grow with the two main orientations named type A and B. The epitaxial relations for both orientations are given below

Type A	Type B
MnAs $[11\bar{2}0] \parallel$ GaAs $[110]$	MnAs $[11\bar{2}0] \parallel$ GaAs $[1\bar{1}0]$
MnAs $[0001] \parallel$ GaAs $[1\bar{1}0]$	MnAs $[0001] \parallel$ GaAs $[110]$
MnAs $[1\bar{1}00] \parallel$ GaAs $[001]$	MnAs $[1\bar{1}00] \parallel$ GaAs $[001]$

This means that the *a* axis of hexagonal MnAs is aligned either along GaAs $[110]$ or GaAs $[1\bar{1}0]$ for the A and B orientations, respectively. Therefore, the unit cell in one orientation is rotated in the interface plane by 90 ° with respect to the other [58]. The unit cells for the A and B orientation are shown schematically in Fig. 3.23. The orientations of the MnAs domains in a film mainly depend on the surface reconstruction and termination of the GaAs (001) template [56, 68]. A very As-rich c(4×4) [or d(4×4)] template mainly results in type A orientation and a As-deficient c(4×4) surface covered by one monolayer of Mn results in type B orientation [56]. Samples that are grown in a As-deficient environment often contain both orientations simultaneously. However, by optimizing the growth conditions it is possible to tailor the fractions of different orientations.

We discuss here two MnAs films (samples I and II) with different contents of B domains. Both samples were grown on the c(4×4) reconstructed surface of GaAs but sample I was grown in a more As-deficient regime than sample II. In-plane grazing incidence diffraction allows a quantitative determination of the rotated domains of MnAs. It is worth to mention that it is not easy to detect the different rotated domains with traditional x-ray diffraction. The radial GID profiles recorded along both the GaAs $[110]$ and GaAs $[1\bar{1}0]$ directions for sample I are shown in Fig. 3.24 (a) and (b), respectively. The presence of the MnAs $(11\bar{2}0)$ peak in both profiles clearly indicates the presence of both the A and B orientation in the film. The profiles are normalized to the monitor counts. In the kinematical approximation, the percentage of A and B orientation can be estimated

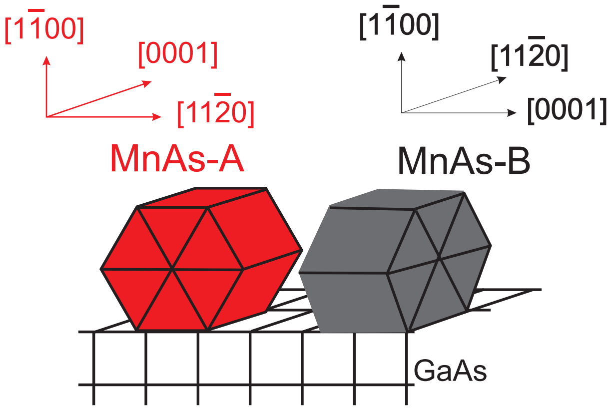

Figure 3.23: Schematic view of the epitaxial scheme for A and B oriented MnAs domains on GaAs (001). The unit cells are rotated by 90° relative to each other.

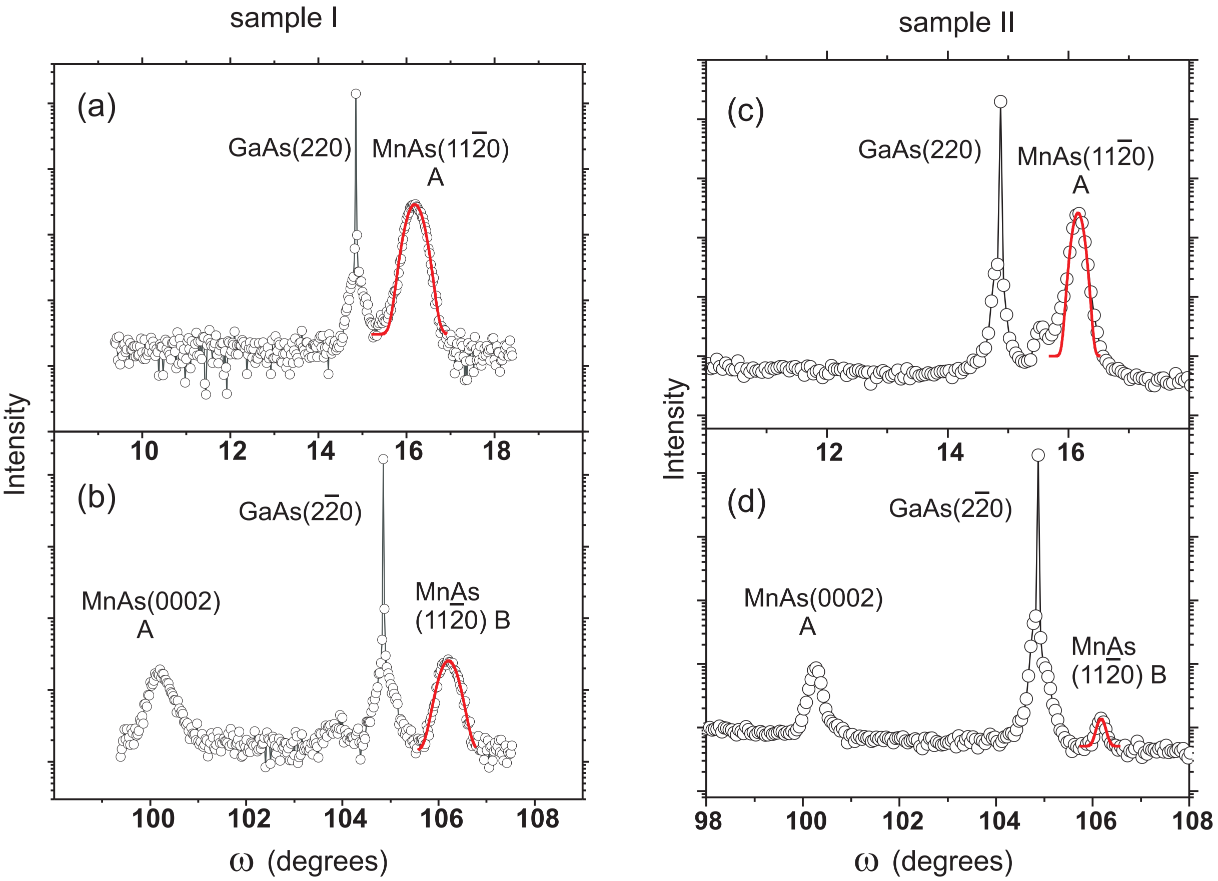

Figure 3.24: Radial GID profiles from MnAs samples [sample I, (a,b) sample II (c,d)] showing both the A and B orientation . A higher content of B oriented domains is present in sample I in comparison to sample II. The MnAs peaks are fitted with a Gaussian. Sample I is grown in As-deficient conditions whereas sample II is grown under As-rich conditions.

by comparing the intensities of similar reflections. According to the definition given above for the A and B orientations the MnAs $(1\,1\bar{2}\,0)$ in the profile Fig. 3.24 (a) is attributed to the A orientation and in Fig. 3.24 (b) is to the B orientation. Therefore by comparing the intensities we obtain

$$\frac{\mathrm{I}^{\mathrm{A}}_{\mathrm{MnAs}\,(1\,1\,\bar{2}\,0)}}{\mathrm{I}^{\mathrm{B}}_{\mathrm{MnAs}\,(1\,1\,\bar{2}\,0)}} = 6.7\ , \tag{3.8}$$

where, $\mathrm{I}^{\mathrm{A}}_{\mathrm{MnAs}\,(1\,1\,\bar{2}\,0)}$ is the intensity of the MnAs $(1\,1\,\bar{2}\,0)$ peak from the A orientation and $\mathrm{I}^{\mathrm{B}}_{\mathrm{MnAs}\,(1\,1\,\bar{2}\,0)}$ is intensity from the B orientation. The film contains 13% B-oriented and 87% A-oriented MnAs domains. The occurrence of both domains is also resolved in the RHEED azimuthal scan of the sample I and shown in the Fig. 3.25. The unit cells corresponding to the A and B orientations are explicitly shown. However, the scan also contains some extra spots which cannot be attributed to either the A or B orientation. This means that the film contains some additional phases or orientations. Additional orientations of MnAs are also reported to occur during growth on the As-deficient surface [86].

The radial GID profiles along the GaAs [1 1 0] and GaAs $[1\,\bar{1}\,0]$ direction for sample II are shown in Fig.3.24 (c, d). We find a very low percentage (0.5%) of B oriented domains. Therefore, we conclude that growth on the As-rich surface favors the growth of A oriented

Table 3.1: Fraction of A and B orientations in MnAs samples grown in As-rich and As-deficient conditions. l is the in-plane domain size along the $[1\,1\,\bar{2}\,0]$ direction.

Sample	thickness (nm)	B-orientation (%)	$l^{\mathrm{A-orientation}}_{[1\,1\,\bar{2}\,0]}$ (nm)
Sample-I (As-deficient condition)	5	13	8
Sample-II (As-rich condition)	6	0.5	18

films. However, it seems to be difficult to achieve completely single domain films.

A satellite reflection (due to the periodic array of misfit dislocations at the interface as will be discussed in chapter 5) is seen in the middle between the layer and substrate reflection in Fig. 3.24 (c), whereas no such satellite is observed in Fig. 3.24 (a). This can be explained by considering the dependence of the in-plane domain size (correlation length l) on the percentage of B oriented domains present in the sample. From the width of the

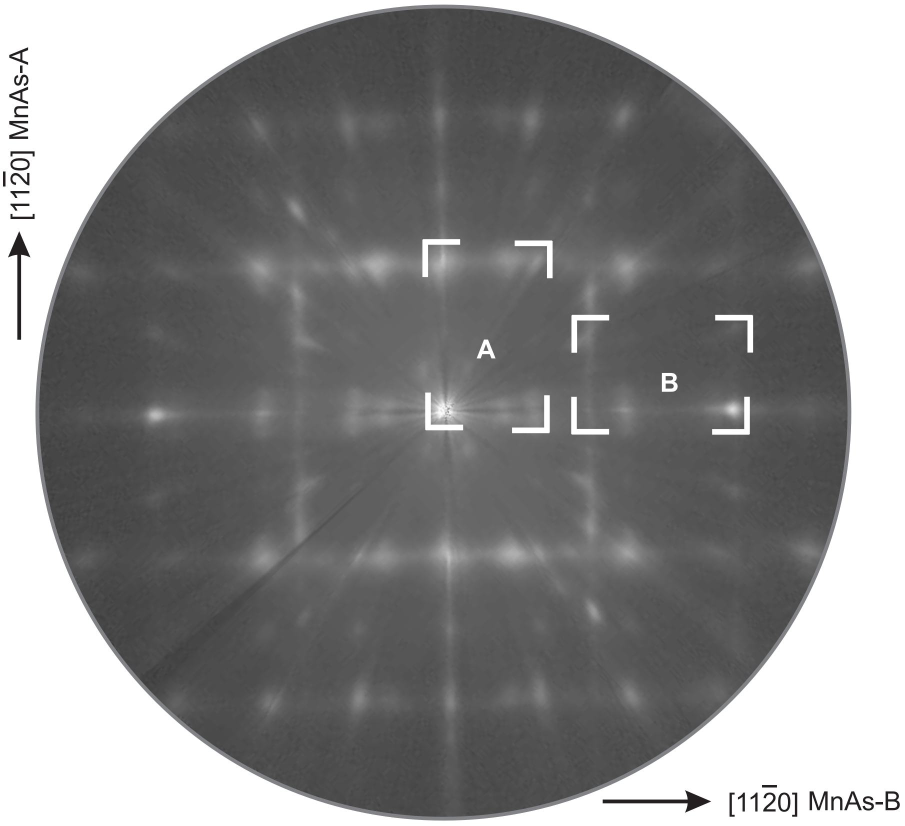

Figure 3.25: RHEED azimuthal scan showing both the A and B oriented MnAs domains. The squares represent the unit cells of both orientations.

MnAs $(1\,1\,\bar{2}\,0)$ reflection it is clear that the sample with a higher percentage of B oriented domains has a larger width of the MnAs peaks, which means smaller domain sizes. The average in-plane domain size for both the A and B-oriented domains is calculated using Scherrer's formula and the result is presented in the table 3.1. We find that the sample having a lower percentage of B domains has about twice the island size and therefore better crystal quality. Since the $[1\,1\,\bar{2}\,0]$ direction of A and B orientations are perpendicular to each other and the domain size for sample I is small, there is no long-range ordering of dislocations. Therefore, in a GID measurement, which averages the signal from a large area of the sample the peak due to the periodic dislocations is absent. In contrast to this, sample II has a domain size of 18 nm with smaller B domains. In this sample the periodic dislocation structure at the interface becomes visible.

For this same reason, the satellite due to periodic dislocations is absent during the *in situ* measurements in Fig. 3.15. We estimate about 7% of B oriented domains in that case. In conclusion, a higher percentage of B oriented domains decreases the crystal quality and creates a disordered interface with irregular dislocation spacing. Therefore, in this thesis, unless otherwise specified, all the work is carried out with samples that contain 99.5% of A oriented MnAs domains.

3.7 Magnetic properties of thin MnAs films grown on GaAs (0 0 1)

The magnetization curve as well as the microscopic magnetic domain structure of MnAs/GaAs (0 0 1) heterostructures have been extensively studied in recent years [87, 88, 89, 90]. The studies have focused mainly on the magnetic properties of thick MnAs films starting from a thickness of 40 nm up to about 500 nm. Here we will discuss the integral magnetic properties of thin MnAs films in the thickness range of 3–20 nm. Magnetization measurements on a macroscopic scale were carried out using a SQUID magnetometer. In our samples, due to the thick GaAs substrates and thin films, the diamagnetic contribution is quite high. Therefore, all signals were carefully corrected for the diamagnetic contribution from the substrate. Figure 3.26 (a, b) shows the magnetization loop and corresponding surface morphology for two different samples (sample I and II). As seen from the atomic force micrographs (AFM), the MnAs films do not show a stripe pattern like the thick samples [91]. The morphology rather shows the presence of distinct islands. The nominal thickness of sample I is 3 nm and that of sample II is 4 nm. The root mean square (rms) roughness of sample I is higher than that of sample II (0.36 nm). A wide hysteresis loop is observed for both samples when applying the magnetic field in-plane along the GaAs [1 1 0] direction as shown in Fig. 3.26. This indicates that the easy axis of magnetization is along the GaAs [1 1 0] corresponding to the MnAs *a* axis. The magnetization loop along GaAs $[1\,\bar{1}\,0]$ instead requires a rather high field to saturate all the magnetic moments, which indicates that this direction is rather hard compared to the [1 1 0] direction. The magnetization curve along GaAs $[1\,\bar{1}\,0]$ also shows a hysteretic behavior. This is because of the presence of B oriented MnAs islands with easy axis along the GaAs $[1\,\bar{1}\,0]$ direction. From x-ray diffraction measurements we know that although the film consists of islands, the islands are not randomly oriented. The preferential orientation of islands at this thickness is also confirmed by the SQUID measurements. The corners of the hysteresis loop are not perfectly sharp, rather they are rounded. This may

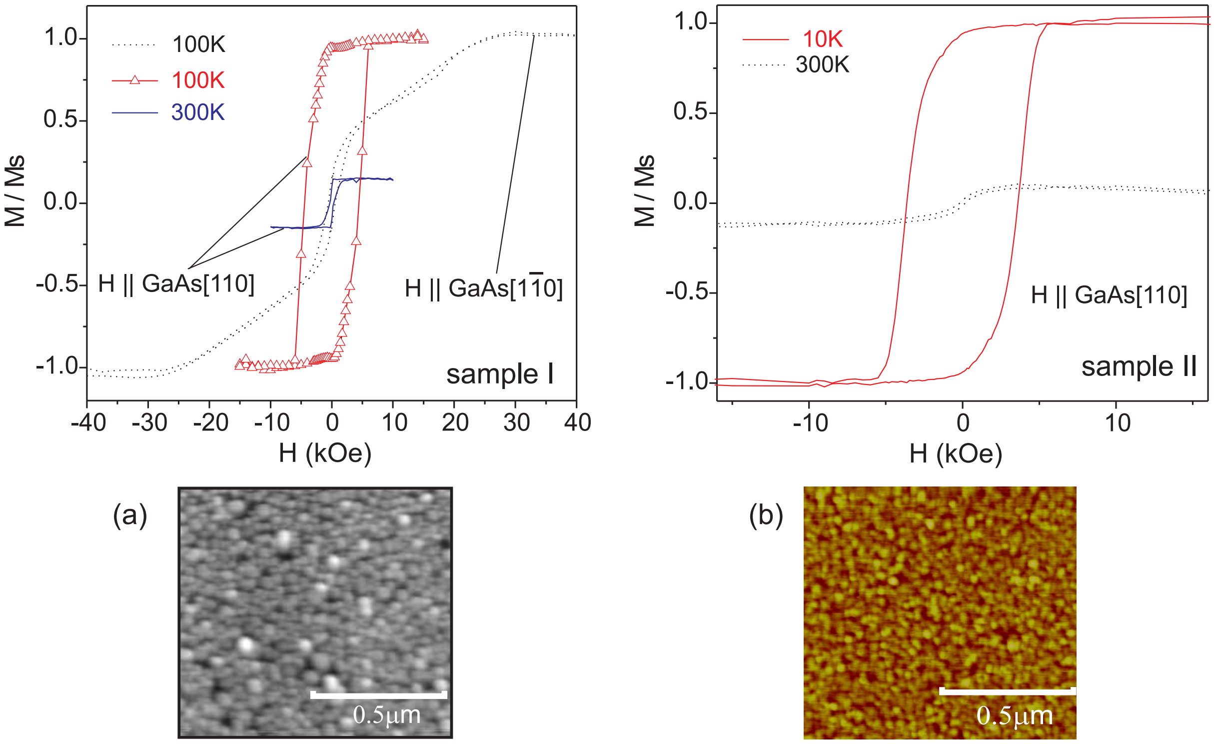

Figure 3.26: (a) The hysteresis loop of a 3 nm thick MnAs film (sample I) at different temperatures and different direction of applied magnetic field. (b) The hysteresis loop for the 4 nm thick MnAs film (sample II). The surface morphology of both the samples are shown below the hysteresis curves.

be related to the orientation and morphology of the islands. This gives a first indication about the relation between structure and magnetic properties but to confirm it more data are required. The switching width for samples I and II is about ± 5 KOe.

The magnetization loop of another sample (III) having a nominal thickness of about 20 nm is shown in Fig. 3.27. The surface morphology for this sample is shown in Fig. 4.1 (b). Although the film consists of islands, the size of the islands is two orders of magnitude larger than that of sample A and B and the rms roughness is also small. The magnetization loop with magnetic field applied along GaAs [1 1 0] shows an almost perfect square shape and is shown in Fig. 3.27 (a). This clearly indicates the improvement of magnetic properties with improved surface morphology and grain size. The switching width of about 1 KOe is quite small in comparison to sample I and II. The magnetization loop with field applied along the GaAs $[1\,\bar{1}\,0]$ is shown in Fig. 3.27 (b). Clearly this is the direction of the hard axis, and the film exhibits a strong anisotropy. However, to understand clearly the evolution of anisotropy and the influence of structural properties, more measurements are required. The Curie temperature of these samples are determined by measuring magnetization as a function of temperature without an applied field. The Curie temperature is determined to be around 320 K in agreement with the previously reported value for continuous films [87].

3.8 Conclusions

MnAs films can be successfully grown on GaAs (0 0 1) substrates by MBE. RHEED and GID are employed to investigate the nucleation process and strain relaxation during the

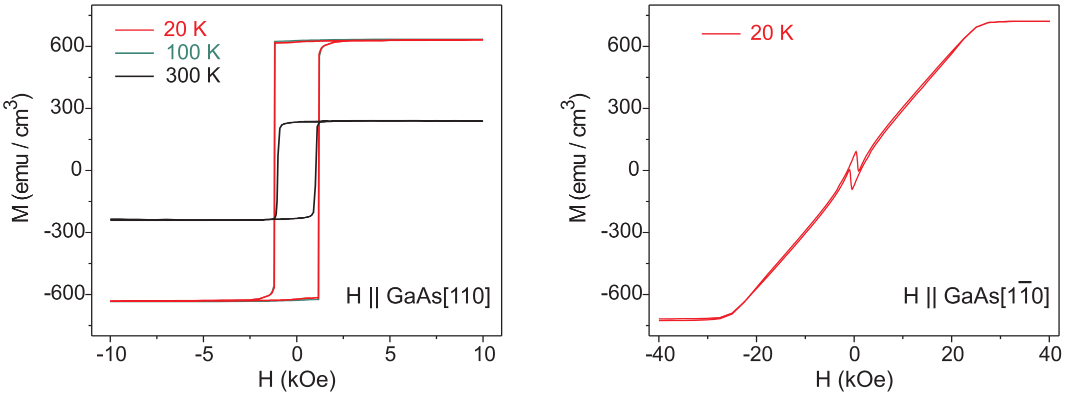

Figure 3.27: (a) Magnetization loops for a 20 nm thick MnAs film. The magnetic field is applied along the GaAs [1 1 0] direction. (b) The hysteresis loop with the field applied along GaAs [$1\,\bar{1}\,0$].

early stages of growth and coarsening of MnAs islands. The RHEED measurements reveal four different stages until the epitaxial lock-in of the MnAs film is established. Below a coverage of 0.3 ML a weak increase of diffuse intensity is indicative of a coherent adsorption or binding of the Mn adatoms during the early stages of growth. Although the STM measurements indicate a Volmer–Weber type nucleation and the x-ray diffraction results at the later stages are consistent with such an interpretation, this would correspond to an initial wetting behavior of the surface. The nucleation process therefore has elements of both Volmer–Weber and Stranski–Krastanov growth and cannot be easily classified into one of the two categories. At coverages between 0.3 ML and 0.7 ML, randomly oriented units of unknown stoichiometry but with nearest neighbor distance of MnAs are formed. The epitaxial constraint is imposed by the substrate on these disordered units between 1 to 2 ML thickness. The strong interaction between the film and the substrate along the GaAs [1 1 0] and a weak interaction along [$1\bar{1}0$] is seen. An almost relaxed MnAs layer forms at a coverage of 2.5 ML. The strain due to the lattice mismatch is released by the formation of misfit dislocations. The dislocations are directly form at the interface during growth. The relaxation process continues with a fast rate until the coalescence, after which, no further relaxation occurs. The relaxation process is thermally activated. The presence of two different orientations of MnAs is detected. As-rich starting surface favors the formation of A oriented MnAs domains. The ultrathin MnAs films show ferromagnetic behavior.

Chapter 4

Defects and microstructure of MnAs films on GaAs (0 0 1)

4.1 Background

Experimetally observed x-ray diffraction maxima are broadened by both the instrument and the sample. The effect of a finite crystal size on the x-ray diffraction line profiles has been known since the experiment of Friedrich, Knipping and Laue [92]. The experimentally observed diffraction line profile $\mathrm{P}(\theta)$ is a convolution of three functions [93],

$$\mathrm{P}(\theta) = \Delta\lambda \star G \star S + \text{background}\,, \tag{4.1}$$

where $\Delta\lambda$ is the spectral distribution of the x-ray source, G is the convolution of all abberations arising from the instrumentation and diffraction process. S is the contribution from the sample. Therefore, to determine the microstructure of the sample, the physically broadened profile due to the sample (S), must be extracted from the observed diffraction profile.

Although many treatments of the broadening of diffraction profiles exist the literature, the most commonly used theories [11, 94] consider two types of structural broadening that occur simultaneously. The first one is the broadening due to the finite size regions in the sample that are diffracting incoherently with respect to one another (grain size or crystallite size effect). In particular, the reduction of the crystallite size in the sample broadens the diffraction line. If the reduction of the crystallite size occurs regardless of any particular crystallographic direction (isotropic condition), the line broadening in reciprocal space is the same for all peaks. This broadening due to finite size is independent of the diffraction order. The second type of broadening is due to the strain caused by the deviation of atoms from their ideal positions in the crystalline matrix. Strain broadening is more complicated because the strain in a thin epitaxial film can have several origins like dislocations, stacking faults, point defects, distorted grain boundaries and inhomogeneous deformations of lattice planes. The strain broadening depends on the order of the reflection and increases with the enhancement in length of the scattering vector. In some cases, due to small inclusions of a different element in the matrix or the presence of residual stresses, the peak position in the diffraction profile can be shifted from the ideal position. The presence of stacking faults in the crystals may affect the peak shape through asymmetry and peak shifts [95].

In the last four decades a large amount of work has been devoted to the extraction of information concerning size and strain from the x-ray diffraction line profiles with particular emphasis on polycrystalline materials [96]. At present, the most frequently used methods to extract the size and strain parameters by decomposing the total line broadening into a broadening due to size and broadening due to strain uses one of the following methods:
The Williamson–Hall (W-H) analysis using the integral width of the line profile [97].
The Warren–Averbach analysis using the Fourier coefficients of the line profile [98].
These two methods are briefly introduced in the following section.

4.2 Line profile description

A line profile measured as a function of diffraction angle 2θ represents a profile $I(s, d_l^\star)$ in reciprocal space with $s = [2\sin\theta/\lambda] - d_l^\star$, where λ is the wavelength of the x-rays used. $d_l^\star$ represents the reciprocal lattice vector for the l^{th} order reflection and $d_l^\star/d_1^\star = l$. The average length of the diffraction vector $\mathbf{k}$ is taken for $d_l^\star$, i.e. the value of $2\sin\theta/\lambda$ at the centroid of $I(s, d_l^\star)$ [94]. The profile $I(s, d_l^\star)$ can be expressed as a Fourier series [11]:

$$I(s, d_l^\star) = F \sum_{L=-\infty}^{+\infty} \left[A(L, d_l^\star)\cos(2\pi L s) + B(L, d_l^\star)\sin(2\pi L s) \right] , \tag{4.2}$$

where F is a constant, A and B are the cosine and sine Fourier coefficients and L is a length in real space parallel to $\mathbf{k}$. Normally L is considered as a continuous variable.

If the line profile is symmetric, the term $B(L, d_l^\star)$ will vanish, and the line broadenings is represented by the integral width β (integrated intensity of the line profile divided by maximum intensity). The β in reciprocal space is related to $A(L, d_l^\star)$ by

$$\beta^{-1} = \int_{-\infty}^{+\infty} A(L, d_l^\star) dL . \tag{4.3}$$

Line profile decomposition The decomposition of a the line profile is important in order to distinguish between size and strain broadenings. The Fourier coefficients (A, B) in eqn 4.2 are expressed as products of a diffraction order dependent strain coefficient (A_D, B_D) and a diffraction order independent size coefficient (A_S, B_S) [11] as follows

$$\begin{aligned} A(L, d_l^\star) &= A_S(L) \quad A_D(L, d_l^\star) \\ B(L, d_l^\star) &= A_S(L) \quad B_D(L, d_l^\star) \end{aligned} \tag{4.4}$$

Integral width method A detailed treatment of this method is presented in reference [99]. This method uses integral width, $\beta(d_l^\star)$, of the line profiles, $I(s, d_l^\star)$, to calculate the integral width due to size, (β_S) of $I_S(s)$, and $\beta_D(d_l^\star)$ of $I_D(s, d_l^\star)$. I_S and I_D indicate the size and strain broadened profiles respectively. This procedure assumes that $\beta_D(d_l^\star) \propto (d_l^\star)$ and that $I_S(s)$ and $I_D(s, d_l^\star)$ have either Gaussian or Lorentzian shapes [100, 101]. The Williamson–Hall method [97] is based on this approach.

In the linear version of the Williamson-Hall analysis [on a 2θ scale instead of s scale] [1], it is assumed that the broadening due to size (β_S) and strain $[\beta_D(d_l^\star)]$ from the same set

---

[1] This Williamson-Hall analysis involves a plot of $\beta\cos\theta$ versus $\sin\theta$.

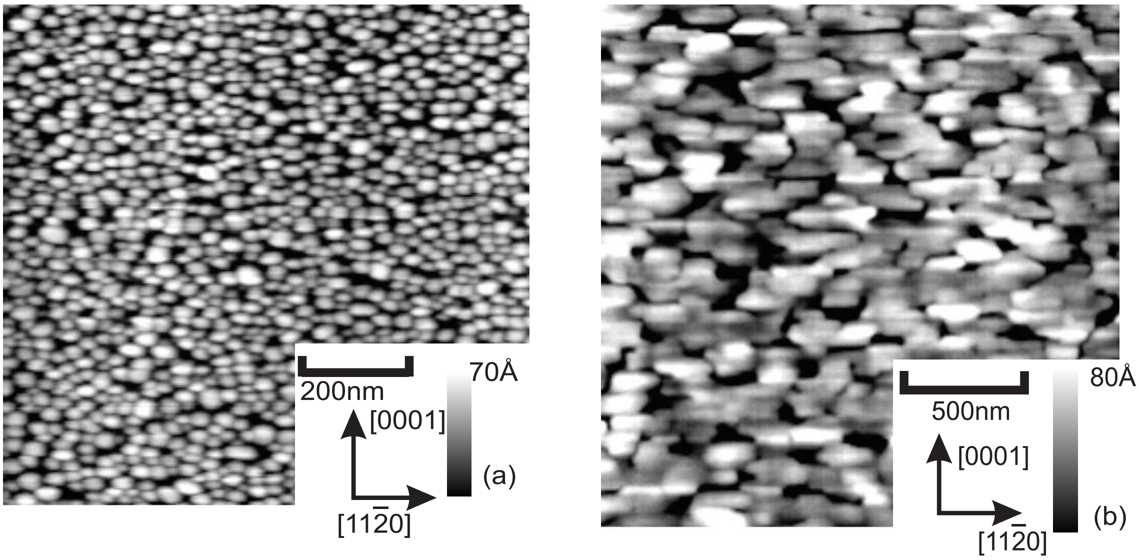

Figure 4.1: Atomic force micrographs of (a) 1×1 μm^2 of a 5 nm thick, (b) 2×2 μm^2 of a 20 nm thick MnAs film grown with a growth rate of 0.36 nm/hour. The picture shows islands of the MnAs films. The micrographs are recorded at room temperature. The scan directions are indicated in the figure.

of lattice planes are linearly additive:

$$\beta(d_l^\star) = \beta_S + \beta_D(d_l^\star) = \frac{1}{D_{\mathrm{WH}}} + \sqrt{2\pi}\, e_{\mathrm{WH}}\, d_l^\star \,, \tag{4.5}$$

where D_{WH} and e_{WH} are the size and strain parameter, respectively. Therefore, a plot between $\beta(d_l^\star)$ versus $d_l^\star$ yields a straight line and the intercept of the ordinate axis gives D_{WH}. The slope is interpreted as $\sqrt{2\pi}e_{\mathrm{WH}}$.

4.3 Micro-strain of MnAs Islands

We performed a line shape analysis of x-ray diffraction profiles to investigate the microstructure, lattice imperfections and defects in the MnAs epitaxial films at the early stage of growth. Before discussing the microstructure and the micro-strain in the MnAs islands during growth, we will briefly discuss the surface morphology of the MnAs films at the early stages of growth.

4.3.1 Surface morphology

A Park scientific instruments AFM system operating in contact mode was used to study the surface morphology at different thicknesses. The samples were annealed *in situ* at 400 °C for 10 min. The measurements were done after exposing the sample to air for more than 2 hours. Figure 4.1 (a) represents the morphology of a MnAs film with nominal thicknes of 5 nm (sample I) and Fig. 4.1 (b) represents the surface morphology of a 20 nm thick MnAs film (sample II).

The grain sizes determined from Fig. 4.1 are in the range of about 20–50 nm for sample I and 100-300 nm for sample II. The AFM micrograph clearly reveals island formation

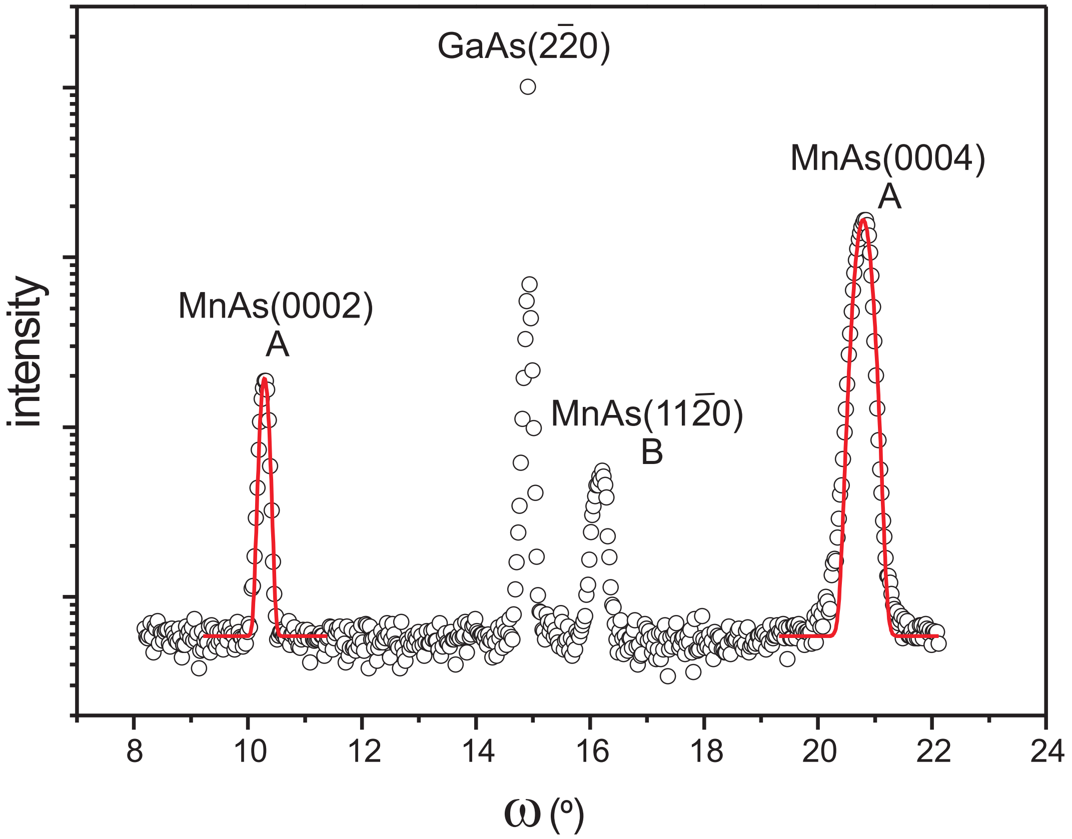

Figure 4.2: X-ray diffraction curve ($\omega - 2\theta$ scan, circles) measured at a substrate temperature of 200 °C along the GaAs $[1\,\bar{1}\,0]$ direction with the GaAs $(2\,\bar{2}\,0)$ substrate and the MnAs $(0\,0\,0\,2)$ and $(0\,0\,0\,4)$ layer reflections (from domains in A orientation). The MnAs $[1\,1\,\bar{2}\,0]$ reflection from domains in B orientation is also visible. The MnAs $(0\,0\,0\,2)$ and $(0\,0\,0\,4)$ peaks are fitted by Gaussian functions (solid lines).

during the starting phase of the growth. This allows us to compare the island sizes obtained by *ex situ* AFM and by *in situ* GID. The height of the islands in the micrograph is 7 nm (sample I) as seen from Fig. 4.1 (a). The height of the islands is almost equal to the film thickness, which means that coalescence has not yet started in the film. The islands are randomly distributed. On the other hand, for sample II the height of the grains is 8 nm [see Fig. 4.1 (b)] whereas a film thickness of 20 nm is obtained by *ex situ* x–ray reflectivity measurements. Therefore, we conclude that the trenches do not reach the substrate surface in this AFM micrograph and so the film is already continuous.

Our observations in chapter 3, STM investigations by Kästner *et al.* [78] and finally Fig. 4.1 reveal that at the beginning of MnAs growth, the film consists of many separate islands which coalesce only at a later stage to form a continuous film. At the boundaries of the originally separated islands an accumulation of defects is expected. Therefore, we can model the whole system as consisting of coherently diffracting regions separated by defected regions. In the next section we will call these coherently diffracting regions as “domains".

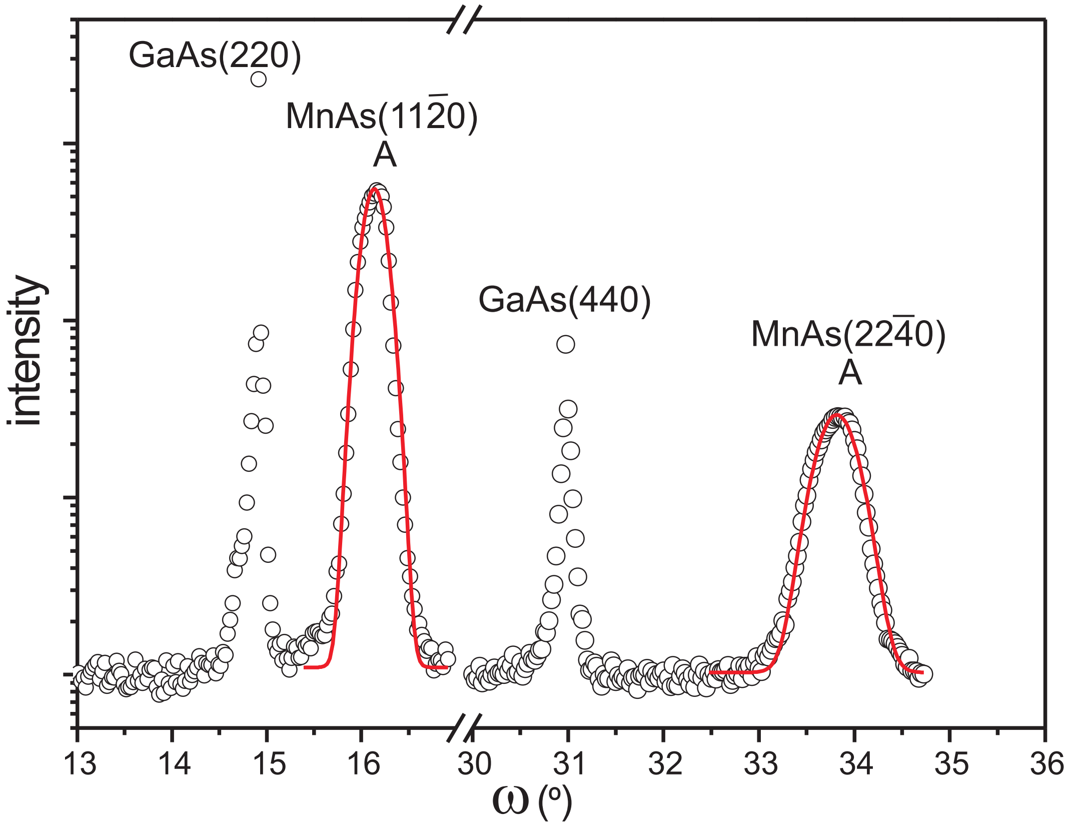

Figure 4.3: X-ray diffraction curves ($\omega - 2\theta$ scan, circles) measured at a substrate temperature of 200 °C along GaAs [1 1 0] with the GaAs (2 2 0) and (4 4 0) substrate and the MnAs (1 1 $\bar{2}$ 0) and MnAs (2 2 $\bar{4}$ 0) layer reflections of the A type domains. The MnAs (1 1 $\bar{2}$ 0) and MnAs (2 2 $\bar{4}$ 0) peaks are fitted by Gaussian functions (solid lines).

4.3.2 Williamson–Hall Plot

We observe a considerable broadening of the MnAs peak in the radial ($\omega - 2\theta$) scans (shown in Figs. 4.2 and 4.3) and transverse (ω) scans (shown in Fig. 4.4) measured in grazing incidence geometry. The broadening of the transverse scans represents the orientational distribution of the different diffracting domains (in-plane mosaic spread) and will be discussed in section 4.4. On the other hand, the broadening of the radial scans shows the finite size of the diffracting domains and the inhomogeneous deformations inside the domains. The aim here is to separate the two contributions to the peak broadening, the finite size of the crystalline domains in the sample and the nonuniform strain within each domain owing to the lattice defects. Since our x-ray line profiles [cf. Figs. 4.2 and 4.3] are fitted well with a Gaussian function, W-H plots can be successively applied to separate the broadening due to finite size and the one due to strain. The W-H analysis is carried out for sample II.

Figure 4.2 presents a radial scan recorded along the GaAs [1 $\bar{1}$ 0] direction. It reveals the presence of two different orientations in the sample (A and B orientation as discussed in chapter 3). The substrate GaAs (2 $\bar{2}$ 0), the MnAs (0 0 0 2) and the (0 0 0 4) layer reflections from A oriented domains are most pronounced. The MnAs (1 1 $\bar{2}$ 0) peak from the B-oriented domain is visible as well. The corresponding transverse scans of the (0 0 0 2) peak is also shown in Fig. 4.4 (a). Similarly, Fig. 4.3 shows the radial scan along the

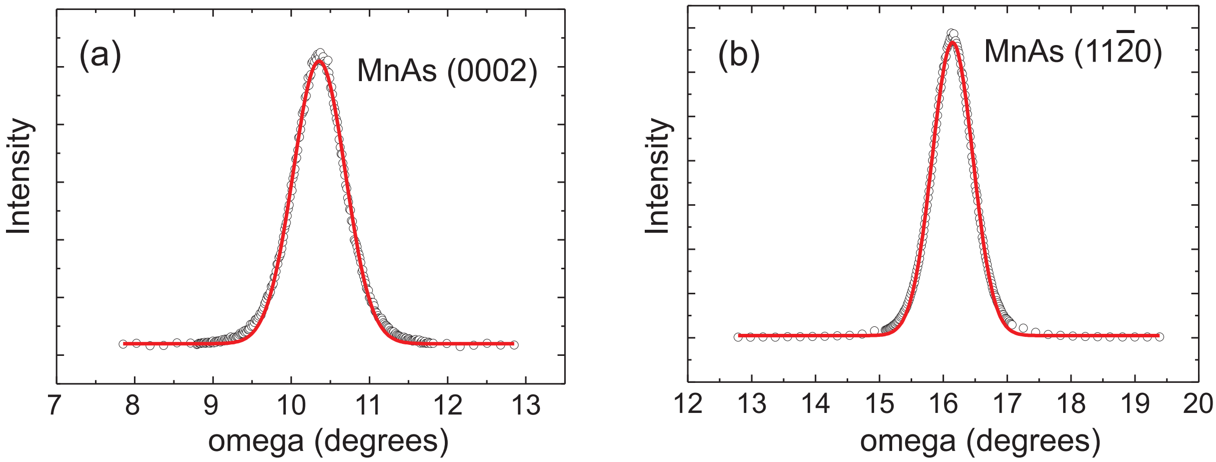

Figure 4.4: X-ray diffraction profile (ω-scan, circles) of (a)MnAs (0 0 0 2) (b) MnAs (1 1 $\bar{2}$ 0) reflection recorded while rocking the sample about the surface normal by keeping the detector fixed. The solid lines show the Gaussian fit to the curves.

GaAs [1 1 0] direction. The transverse scan of MnAs (1 1 $\bar{2}$ 0) reflection is also shown in Fig. 4.4 (b). The broadening of the MnAs (0 0 0 4) peak compared to the MnAs (0 0 0 2) reflection (Fig. 4.2), as well as the broadening of the MnAs (2 2 $\bar{4}$ 0) peak in comparison to the MnAs (1 1 $\bar{2}$ 0) peak (Fig. 4.3) is high in both radial and transverse scans. The integral width of all MnAs peaks in radial scans is smaller than in transverse scans.

The total measured broadening of the x-ray diffraction profile (β_h) can be written as

$$(\beta_h)^2 = (\beta(d_l^\star))^2 + (\beta_G)^2 \,, \tag{4.6}$$

where $\beta(d_l^\star)$ is the width of the physically broadened profile and β_G is the width of the apparatus function. The apparatus function for our diffractometer, including the broadening due to the spectral distribution of x-rays, can be approximated by a Gaussian of 0.1° integral width [102]. In our range of Bragg angles used for the measurements the width of the apparatus functions can be assumed to remain constant [103]. The peak shapes of radial scans are Gaussian, hence we can subtract the width of the device function, β_G, from that of the measured curve

$$\beta(d_l^\star)^2 = (\beta_h)^2 - (\beta_G)^2 \,, \tag{4.7}$$

in order to obtain the width $\beta(d_l^\star)$ of the physically broadened profile [11, 99].

For a Gaussian peak shape, $\beta(d_l^\star)$ can be expressed as sum of squares of the two components [11, 99, 103]. We will use the reciprocal lattice notation, $\beta^\star(d_l^\star) = \beta(d_l^\star)\cos\theta/\lambda$, where θ is the diffraction angle and λ is the wavelength. In reciprocal lattice notation

$$(\beta^\star(d_l^\star))^2 = (\beta_S^\star)^2 + (\beta_D^\star(d_l^\star))^2 = (\beta_S^\star)^2 + (2e_{\mathrm{WH}} \cdot d_l^\star)^2 \,, \tag{4.8}$$

where

$$e_{\mathrm{WH}} = \beta_D^\star(d_l^\star)/2d_l^\star = \Delta d/d \tag{4.9}$$

is the strain. The strain here can be interpreted as the variation of d spacings parallel to the interface within a single domain.

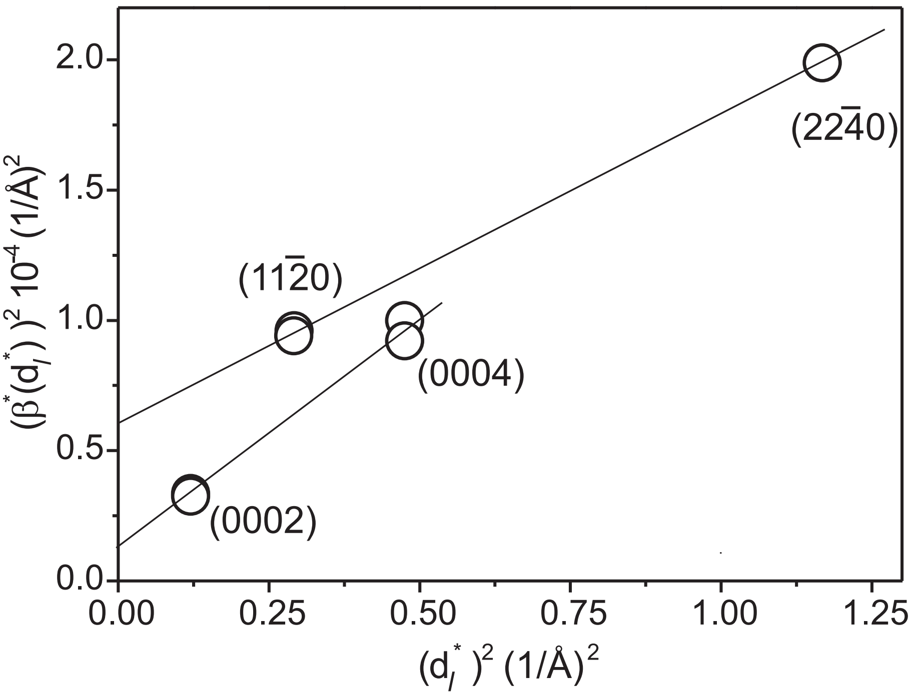

Figure 4.5: Williamson–Hall plot in reciprocal–lattice representation for line profiles of a 20 nm thick MnAs film. $d_l^* = 2\sin\theta/\lambda$ is the reciprocal lattice vector and $\beta^\star(d_l^\star) = \beta(d_l^\star)\cos(\theta)/\lambda$, where $\beta(d_l^\star)$ is the integral width of the physically broadened profile.

According to Eq. 4.8 the plot, $(\beta^\star(d_l^\star))^2$ over $(d_l^\star)^2$ should give a straight line [97, 103]. Such a W-H plot in the reciprocal lattice representation is shown in Fig. 4.5.

We could measure only two orders of reflections in the GID geometry. The intersection with the ordinate axis leads to $\beta_S^\star$. It yields the size

$$L = 1/\beta_S^\star\,. \tag{4.10}$$

This is the average size of a domain (or island) in the direction of the diffraction vector, which in our case is parallel to the interface [82, 104].

Figure 4.6 shows the in–plane domain size L as a function of the thickness of the growing layer. The domain sizes were calculated using equation (4.10) assuming that the strain, e_{WH}, (see Eq.4.9) remains constant during the growth. The average island sizes measured here by *in situ* x-ray diffraction during MnAs growth on exactly oriented GaAs (0 0 1) are of the same order of magnitude as the island sizes obtained by STM [78] for the growth on GaAs (0 0 1) with 2° miscut (after growth interruption and transferring the quenched sample to the STM chamber). The strain e_{WH} is obtained from the slope of the W-H plot. The microstrain and average island size calculated from the W-H analysis are given in Table 4.1. We find a nonuniform strain amounting to 0.54% along the a axis and 0.66% along the c axis.

The island sizes in the AFM micrograph shown in Fig. 4.1 (b) are in the range of about 100–300 nm, i.e., they are larger by a factor of 10 compared to the domain sizes given in Table 4.1. This indicates that coalescence of islands has taken place after terminating the growth. The x-ray measurement is probably probing the size of the originally separated islands.

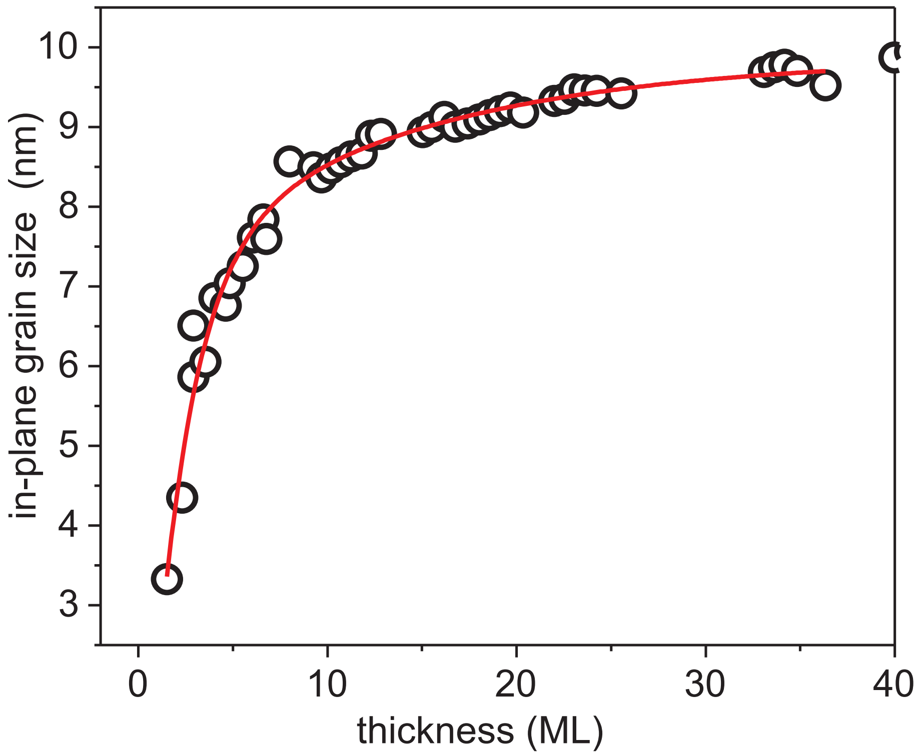

Figure 4.6: In–plane domain size L versus layer thickness during growth. The size is calculated according to Eq. 4.10. The data is fitted with an exponential function.

4.3.3 Correlation between dislocations

In this section, we will describe of correlation among the misfit dislocations along the two perpendicular directions at the interface. Here we assume that the strain is mainly due to misfit dislocations. The diffraction peak width ($\beta^{\star}_{rand}$) due to the random distribution of misfit dislocations at the MnAs/GaAs interface is calculated by the method developed by Kaganer *et al.* [105]. The diffraction peak width due to the strain is taken from the W-H analysis (Table 4.1).

Along MnAs a axis From chapter 3 we know that the MnAs layer is almost completely relaxed on the GaAs substrate during growth. Therefore, along the MnAs $[1\,1\bar{2}\,0]$ direction the change of in-plane lattice parameter a due to the misfit relaxations is $\Delta a/a$= -0.075. The strain along the a axis is released mainly through a periodic array of misfit dislocations with dislocation lines parallel to the MnAs $[0\,0\,0\,1]$ direction [67, 106]. A more detailed discussion of the periodic dislocations is given in chapter 5. The absolute value of their Burgers vector is $|b|= a= 3.7$ Å. Thus, the linear density of misfit dislocations due to this relaxation can be calculated using the formula

$$\rho = \frac{|\Delta a/a|}{b}\,, \tag{4.11}$$

where ρ is the density of misfit dislocations. We find ρ=0.2/nm i.e. the spacing between the periodic dislocation is close to 5 nm.

According to the method proposed by Kaganer *et al.* [105], the half width of the diffraction peak at large densities of misfit dislocations in reciprocal lattice notation can

Table 4.1: Some microstructural parameters of the MnAs/GaAs (0 0 1) heterostructures. β^*_S obtained from the W-H analysis of the $\omega/2\theta$ scans across the (0 0 0 2), (0 0 0 4) and (1 1 $\bar{2}$ 0), (2 2 $\bar{4}$ 0) diffraction maxima is given. e_{WH} is the nonuniform strain obtained from W-H analysis. $\beta^*_D(d^*_l)$, β^*_{rand}, and γ are calculated for the (0 0 0 4) and the (1 1 $\bar{2}$ 0) reflections. The correlation parameter γ of the positions of the dislocations is estimated from a comparison with the width β^*_{rand} calculated from the theory.

direction along IF	$\beta^\star_S$ Å^{-1}	e_{WH} %	*reflection*	$\beta^\star_D(d^\star_l)$ Å^{-1}	$\beta^\star_{\mathrm{rand}}$ Å^{-1}	γ
0001	0.004	0.66	0004	0.01	0.042	0.24
11$\bar{2}$0	0.008	0.54	11$\bar{2}$0	0.006	0.058	0.10

be estimated as:

$$\beta^\star_{\mathrm{rand}} \approx C\,[Qb\sqrt{\rho/t}]\,, \tag{4.12}$$

where $Q = (4\pi/\lambda)\sin\theta = 2\pi d^\star_l$, λ is the x-ray wavelength, and θ is the Bragg angle. The film thickness t is about 20 nm. C is a numerical factor depending on the orientation of the diffraction vector and the scan direction in reciprocal space. For the grazing incidence diffraction geometry used in this study the numerical coefficient is calculated to be $\sqrt{\ln 2/\pi}$ [82].

$$\beta^\star_{\mathrm{rand}} = Q\,\sqrt{(\ln 2/\pi)\,|\Delta a/a|(b/t)}\,. \tag{4.13}$$

For the MnAs (1 1 $\bar{2}$ 0) reflection the theoretically calculated width is $\beta^\star_{\mathrm{rand}} = 0.058$ Å^{-1}, and the experimentally measured width is $\beta^\star_D(d^\star_l) = 0.006$ Å^{-1}. The calculated peak width ($\beta^\star_{\mathrm{rand}}$) is larger than the measured width ($\beta^\star_D(d^\star_l)$). This is not too surprising. This discrepancy can be explained by the introduction of an effective dislocation density $\gamma\rho$, see Kaganer *et al.* [105]. The term γ is called the correlation parameter between the dislocations and defined by $\gamma = \langle(\Delta N)^2\rangle/N$, where N is the mean number of dislocations in some interval and ΔN is the random fluctuation of this quantity. We obtain the correlation parameter γ from the ratio of the measured and the calculated widths

$$\gamma_{(1\,1\,\bar{2}\,0)} = \beta^\star_D(d^\star_l)/\beta^\star_{\mathrm{rand}} \approx 0.10\,. \tag{4.14}$$

The low value of gamma indicates that the dislocations are well correlated along the [1 1 $\bar{2}$ 0] direction.

Along MnAs *c* axis Along the MnAs [0 0 0 1] direction a coincidence lattice is observed [67, 107]: every fourth {0 0 0 2} MnAs plane fits every sixth {2 2 0} GaAs plane forming a commensurate interface region. This 4/6 ratio reduces the lattice mismatch from 30% to about 5%. The remaining misfit is released by the insertion of additional planes in the coincidence mesh, so-called secondary dislocations. These dislocations lead to an inhomogeneous deformation field near the interface, similar to the real dislocations observed in the perpendicular direction, causing the broadening of the x-ray diffraction peaks. We formally define an effective Burgers vector b of such an extended dislocation. The absolute value of its component along the interface is $|b_{\mathrm{IF}}| = c_{MnAs} - a_{GaAs}/\sqrt{2} = 0.171$ nm. For the [0 0 0 4] reflection the value is β^*_{rand} calculated using Eq. 4.13 is 0.042 Å^{-1}. Our measurements give a value of $\beta_D^\star(d_l^\star) = 0.01$ Å^{-1} for the same reflection. The ratio yields the correlation parameter

$$\gamma_{0\,0\,0\,1} = \beta_D^\star(d_l^\star)/\beta_{\mathrm{rand}}^\star \approx 0.24\,. \tag{4.15}$$

The value of $\gamma_{0\,0\,0\,1}$ is higher than that of $\gamma_{1\,1\,\bar{2}\,0}$. This indicates that the defects are less correlated along the c axis and the relative fluctuations in position of the dislocations are larger. In conclusion, the defects are more correlated along the a axis compared to the c axis. The more details of the interface structure are discussed in chapter 5.

4.4 In situ investigation of mosaicity evolution in MnAs films during growth

To study the evolution of the in-plane mosaic spread of the film after coalescence as a function of layer thickness, in-plane transverse scans (ω-scans) are measured *in situ* during growth. The mosaic of a nominally epitaxial film can be described in terms of two crystallographic parameters: the range of tilt that the sub-grains (domains) have with respect to the substrate normal and their range of twist about the substrate normal [108]. While the former is routinely measured from the width of the x-ray rocking curves of the surface normal Bragg peaks, the latter one is less amenable to measure in the conventional diffraction geometry. To find the in-plane twist in-plane rocking curves must be measured in a transmission geometry, which is difficult with a thick substrate. An in-plane transverse

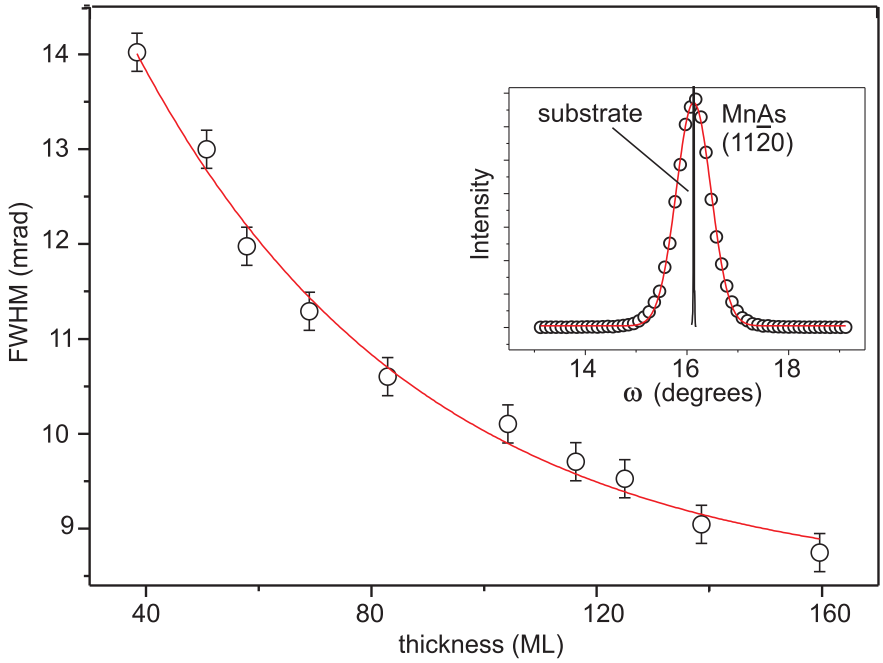

Figure 4.7: The width of transverse scans of MnAs$\,(1\,1\,\bar{2}\,0)$ reflection measured in GID geometry as a function of layer thickness. The error bars indicate the accuracy of each data point. The solid line shows an exponential decay fit to the measured data. The inset shows a single transverse scan with the corresponding Gaussian fit. The resolution-limited substrate GaAs$\,(2\,2\,0)$ peak is also shown in the inset. For clear comparison of widths the GaAs peak is shifted to the center of the MnAs$\,(1\,1\,\bar{2}\,0)$ peak.

scan[2] in grazing incidence geometry directly determines the in-plane mosaic spread of the film.

One of such rocking curves together with the substrate peak is shown as inset in Fig. 4.7. The measured profiles are well fitted with the Gaussian function. The width of the substrate peak is 65 times narrower than the layer peak, which demonstrates our experimental resolution. The measured MnAs $(1\,1\,\bar{2}\,0)$ peak widths are corrected for the instrumental resolution. The FWHM of the rocking curves $\omega(Q)$ continuously decreases with increasing layer thickness as shown in Fig. 4.7. Again, the total integral width of the rocking curves may have two different origins [109]:
(i) the finite size of crystallites $[\omega_S(Q)]$.
(ii) the in-plane mosaic spread of the film (M).

These two contributions are again separated by using the W-H analysis. Two successive order $(1\,1\,\bar{2}\,0)$ and $(2\,2\,\bar{4}\,0)$ peaks are used. We find that the contribution to width from the size is negligible and therefore the broadening of the azimuthal scans are primarily due to in-plane mosaic spread. The in-plane mosaic spread decreases down to 8 mrad, exponentially, with layer thickness. The decrease of the in-plane twist with layer thickness clearly demonstrates the improved layer quality.

4.5 Ex situ x-ray diffraction at room temperature

Conventional co-planner high-resolution x-ray diffraction is a nondestructive tool to measure the out-of-plane orientations of the epilayer and the substrate underneath. Simultaneously the strain in the growth direction can be measured. We use a PANalytical X'Pert diffractometer system with 1 mm receiving slit. The diffractometer is equipped with x-ray mirror and a Ge (0 2 2) monochromator and utilizes Cu-Kα_1 radiation with a wavelength of 0.154 nm. The XRD scans are performed *ex situ* at room temperature.

Figure 4.8 presents a $\theta-2\theta$ x-ray diffraction scan of a 50 nm thick MnAs film grown on GaAs (0 0 1). Here, θ denotes the glancing angle of incidence on the sample surface and 2θ the detector angle with respect to the incident beam. Three orders of the GaAs substrate and the MnAs reflections are clearly distinguishable. The MnAs reflections are split into α MnAs and β MnAs peaks. The in-plane lattice spacing of α and β MnAs differ by 1.2% . As a consequence, they are under different strain conditions in the out-of-plane direction. This leads to the splitting of the MnAs peaks. The coexistence of two different phases of MnAs (α MnAs and β MnAs) is already well described in the literature [110, 111]. The structure factors of both reflections are almost equal. Therefore, the ratio of the integrated intensities of the α MnAs and β MnAs peaks is equal to the ratio of the volume fractions of the phases in the film. From the ratio of the integrated intensities we have calculated that the film contains almost 80% α MnAs domains and 20% β MnAs domains. The phase coexistence is discussed in detail in section 5.4. Here we concentrate on calculating the structural configuration and deformations in the α and β MnAs domains. Apart of the main substrate and layer peaks, some additional narrow peaks with low intensity are visible (Fig. 4.8). Presumably, these peaks arise from a very low content of MnAs with a different orientation.

---

[2] Such a curve is measured in GID geometry by keeping the angle between the source and the detector constant and equal to twice the Bragg angle of the diffracting plane while rotating the sample about the surface normal.

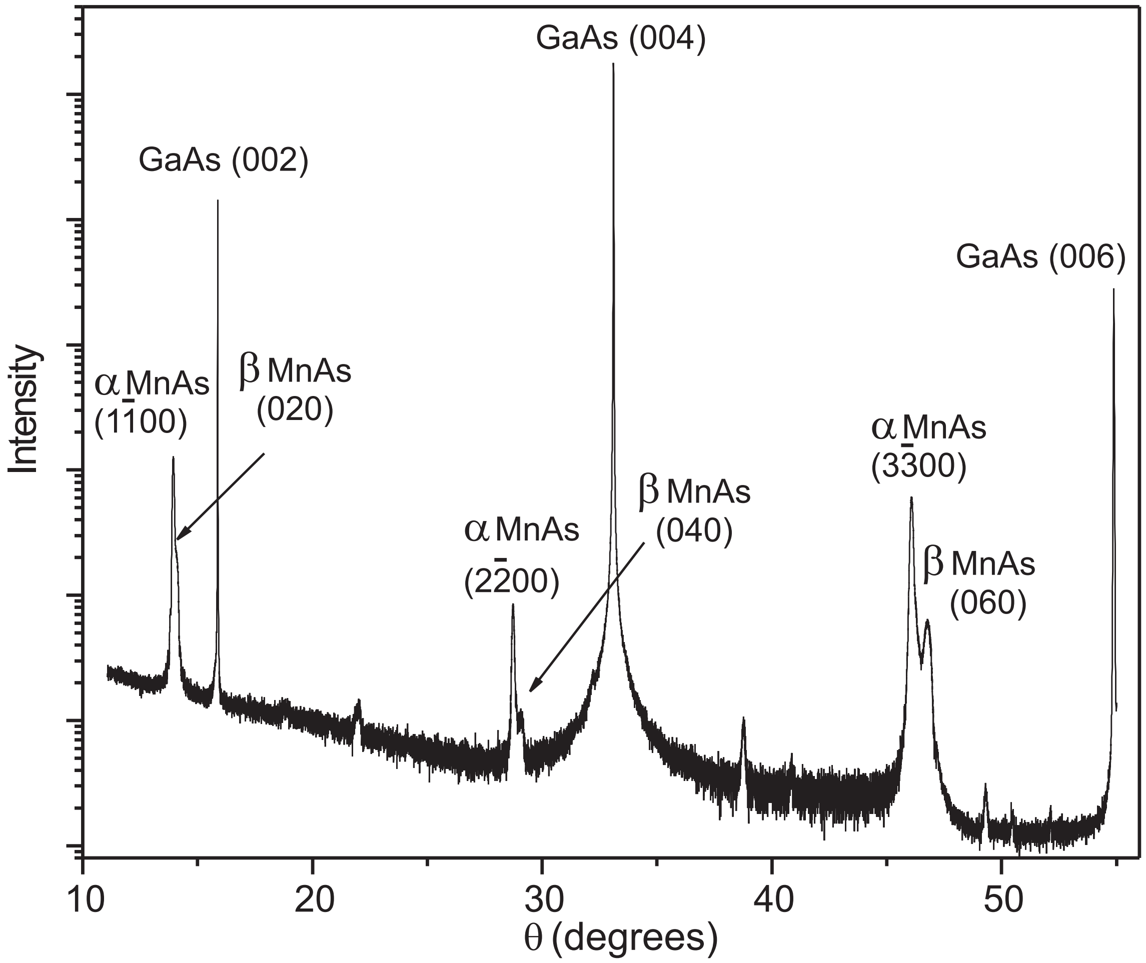

Figure 4.8: Diffraction curve (θ-2θ scan) recorded *ex situ* in co-planar geometry. The reflections are measured at room temperature using (CuK_α radiation). Three consecutive orders of GaAs and MnAs reflections are visible. The MnAs peak is split due to the presence of α and β MnAs phases. The thickness of MnAs layer is about 50 nm.

In the conventional coplanar out-of-plane diffraction geometry, the symmetric radial scans are broadened due to the finite vertical correlation length ($L_\perp$) as well as due to the nonuniform strain along the growth directions (nonuniform strain perpendicular to the interface). These contributions can again be separated by a W-H plot. In this geometry three reflection orders are assessable. The W-H plot for the α and β MnAs is shown in Fig. 4.9. The reflections for both the α and β phases lie in a straight line. This proves that the W-H method can be successfully applied to the in-plane diffraction profiles in GID geometry, even if two orders of reflections are available.

The vertical correlation length calculated from the intersection of the straight lines with the ordinate axis, is almost the same for both α and β MnAs and very close to the thickness of the MnAs film. The non uniform strain in both domains are different. The inhomogeneous strain in the α MnAs domain is smaller in comparison to β MnAs domains. This is clearly seen from the lower slope of the linear fit to the α MnAs peaks in Fig. 4.9 (slope is directly proportional to the strain). This is not surprising, since the film contains 80% of α domains. The width of the α MnAs stripes are 4 times larger. Therefore the α domains are less deformed in comparison to the β domains.

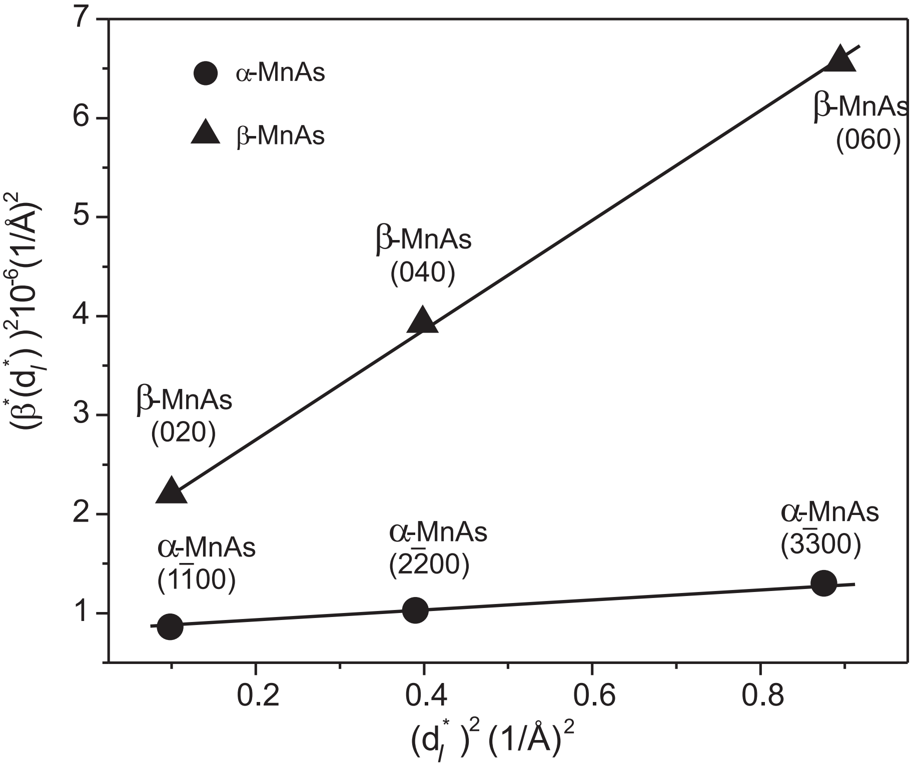

Figure 4.9: Williamson-Hall plot of α and β MnAs peaks. The integral widths are taken form Fig. 4.8.

4.6 Conclusions

Nucleation of MnAs on GaAs proceeds through the formation of many nanoscale islands that are separated from the each other by grain boundaries. The microstructure of the islands can be analyzed by x-ray line profile analysis. The contribution of the finite size of the growing islands and the inhomogeneous strain inside the islands to the width of the x-ray diffraction peak are separated by a Williamson-Hall analysis. An inhomogeneous strain amounting to 0.66% and 0.54% is found along the c axis and a axis, respectively. The size of the growing islands is calculated from the Williamson-Hall plot. The domain size increases exponentially with increasing thickness. The in-plane mosaicity (twist of the islands about the surface normal direction) decreases with increasing thickness. The correlations between the dislocations along the a and c axis of MnAs were then derived. We find that the defects along the a axis are highly correlated (correlation parameter, $\gamma_{11\bar{2}0} = 0.10$) compared to that along the c axis (correlation parameter, $\gamma_{0001} = 0.24$). For a 50 nm thick MnAs film, the β MnAs domains are more deformed than the α MnAs domains at room temperature.

Chapter 5

Interface configuration and phase transition in MnAs/GaAs heterostructures

Epitaxy describes a condition for which adjoining crystals have a definite orientation relationship with a low-energy interfacial structure. The natural lattice mismatch (f) and the chemistry play a major role during the formation of the heterointerface. The elastic strain builds up in epitaxial growth due to two reasons: the lattice mismatch and the difference in thermal expansion coefficient. In conventional heteroepitaxial growth of semiconductors with low lattice misfit there are four possible strain relief mechanisms [112], namely (i) elastic distortion of the epilayer, (ii) interdiffusion between epilayer and substrate, (iii) roughening (islanding) of the epilayer, and (iv) introduction of misfit dislocations. This concept completely fails when the lattice mismatch is enormously large, crystal symmetries along both sides of the interface are different and the dislocation spacing is comparable to the core size of the dislocations [65]. In this chapter, we discuss the MnAs/GaAs (0 0 1) interface which is an example of such a heteroepitaxial interface because of large lattice mismatch, different bonding characteristics, and different crystal symmetry.

In MnAs/GaAs (0 0 1) heterostructures lattice mismatch along the a axis is 7.5% and along the c axis is 30%. This is schematically shown in Fig. 5.1. Along the a axis with low mismatch, a periodic array of misfit dislocations is found, whereas along the c axis the large misfit is released by a coincidence site lattice with additional extended secondary dislocations [67]. Both interface configurations can be compared to the low/high angle grain boundaries although the bonding nature is better defined at the interface here. Low-angle grain boundaries can be created by an array of bulk dislocations, whereas high-angle grain boundaries are described by a periodical repetition of characteristic structural units [113]. Let us now take a closer look on the different possibilities of heterointerface configuration.

Different types of interfaces The atoms at the interface between two crystals in general are displaced from the positions they would occupy in the undisturbed crystal. But it is now well established (and we will discuss this below) that some interfaces have a periodic structure. In such periodic cases the misfit between the crystals connected by the interface is not distributed homogeneously among the atoms at the interface. It is instead periodically localized into discontinuities that separate regions of the interface where the

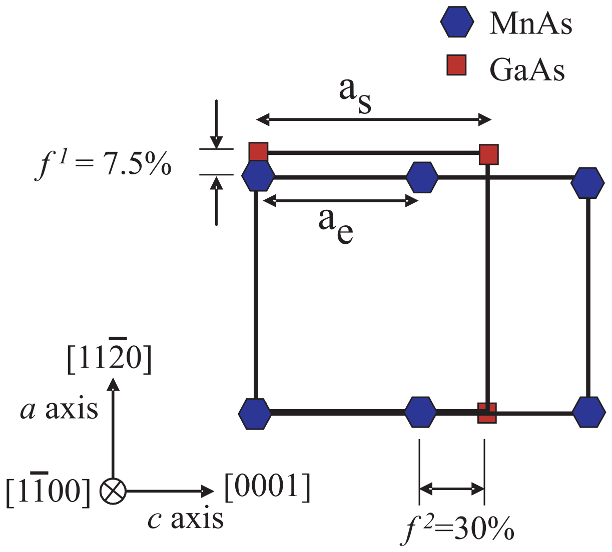

Figure 5.1: Lattice mismatch along the MnAs a axis (f^1) and the MnAs c axis (f^2). The substrate and epilayer spacings are $\mathrm{a_s}$ and $\mathrm{a_e}$, respectively. The growth direction MnAs [1 $\bar{1}$ 0 0] is normal to the plane of the paper.

match between the two crystals is perfect. When these discontinuities are well localized, they are recognized as interface misfit dislocations which separate regions of "good match" from the regions of "poor match". The result is a "semi-coherent" interface. This remains true if the misfit across the interface is $\lesssim 10\%$. The period of these dislocations is $\Lambda = b/f$, where b is the Burgers vector of the dislocation array, and f is the misfit. This type of interface is realized along the a axis of MnAs and schematically shown in Fig. 5.2 (b). Fully coherent interfaces of course also exist between crystals, where a one-to-one correspondence of all atom positions at the interface is observed. Such heteroboundaries contain no dislocations, the whole layer is elastically strained to match the periodicity of the substrate surface. This is schematically shown in Fig. 5.2 (a)

For large misfit systems ($\gtrsim 30\%$), aforementioned concepts do not apply. The predicted spacing of the dislocations for large misfit systems may turn out to be so small that the misfit is highly localized with respect to the boundary and the dislocation model of the interface only formally applies. Putting it another way, the dislocations get so close to each other that their cores overlap. The atomic arrangements in such boundaries may be very haphazard, and with very little correlations of atomic positions across the boundary. This is called completely incoherent interface. However, in some systems with very high mismatch a sharp and periodic interface is observed, which is explained by a coincidence site lattice.

Coincidence site lattice The concept of a coincidence site lattice [114, 115, 116] was initially developed to explain experiments that showed the existence of certain high-angle grain boundaries with the characteristics of low energy semi-coherent or coherent interfaces. These observations imply that at certain crystal orientations, it is possible to obtain interfaces that contain regions of good fit, where the planes fit exactly, and at regular intervals in the interface plane. It is along these planes that the two crystals connected by the interface match exactly. To get a clear idea let us consider good fit planes

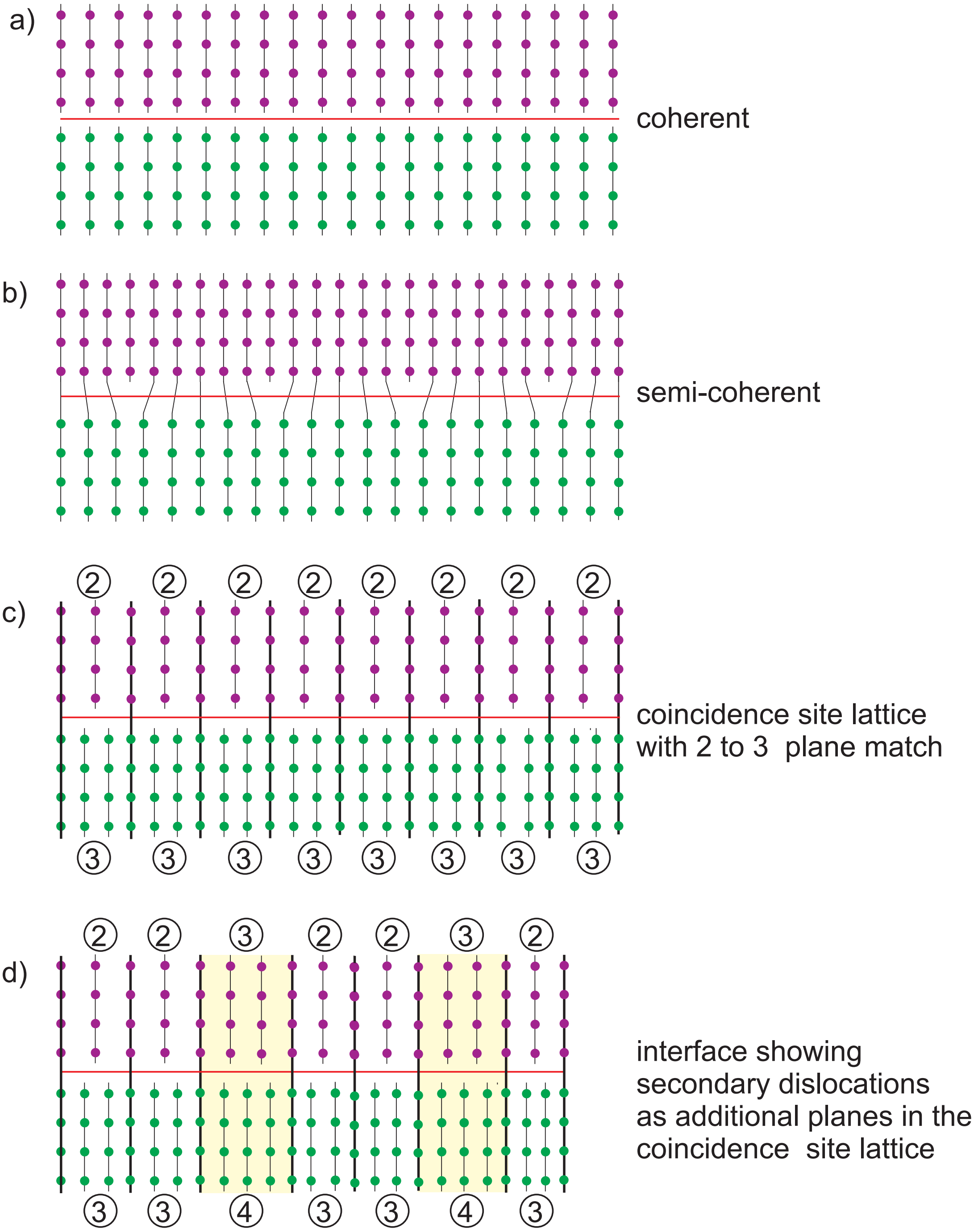

Figure 5.2: Schematic representations of different heteroepitaxial interfaces. The solid circles represent the atoms in the plane and the solid black lines represent crystal planes: (a) A perfect coherent interface, (b) semi-coherent interface with misfit dislocations, (c) coincidence lattice with a lattice plane ratio of $m/n = 2/3$, (d) situation as in (a), however, the slight deviation from 2 to 3 ratio is forming a new coincidence unit with a 3 to 4 plane match.

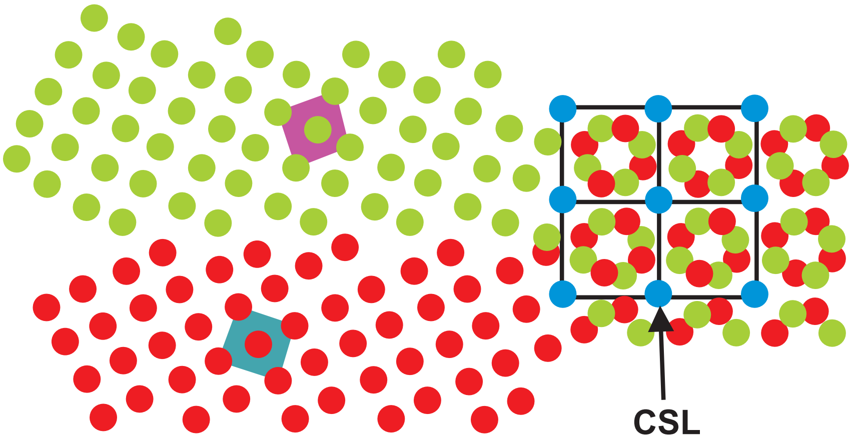

Figure 5.3: Schematic illustration showing the formation of a coincidence site lattice by the interpenetration of two lattices of the same symmetry and different orientation. This is normally the case for high-angle grain boundaries. Courtesy: University of Kiel, Germany.

which correspond to lattice points at the interface which are common to both crystals. If the two lattices (with a common origin) are allowed to interpenetrate and fill all the space, then there exist lattice points (other than the origin) which are common to both the crystals. The formation of a coincidence site by the interpenetration of two lattice is shown schematically in Fig. 5.3. These sets of coincidence points form a coincidence site lattice (CSL) [114, 117]. This same concept was used to explain the experimental observations of epitaxial growth between highly dissimilar materials with huge misfit but smooth interfaces.

In heteroepitaxy a perfect coincidence between the epilayer lattice a_e and the substrate a_s would occur if $a_e/a_s = m/n$, where m and n are both integer. This situation is shown in Fig. 5.2 (c). In general, a heteroepitaxial system is not expected to be in perfect coincidence and the deviation from perfect coincidence is expressed by the coincidence lattice misfit F, which is defined by

$$F = \frac{ma_s - na_e}{ma_s}. \tag{5.1}$$

This coincidence lattice misfit is very small compared to the original lattice misfit. This favors epitaxial growth and the formation of a low-energy interface. This small misfit between the unit cells of the coincidence site lattice is released by defects called “secondary dislocations" which are discussed below.

Secondary dislocations The dislocations in case of semi-coherent interfaces [shown in Fig. 5.2 (b)] are called *primary dislocations* because they relieve the misfit with respect to the ideal single crystal. In large misfit heteroepitaxial systems with a low energy interface due to the coincidence site lattice, a small deviation from the exact coincidence site lattice orientation can be accommodated by a set of interface dislocations. This allows a perfect coincidence site lattice to exist in most of the interface area. These intrinsic interface dislocations [118, 119] are called *secondary dislocations* because they accommodate the misfit with respect to the coincidence site lattice. The cores of the secondary dislocations may be widely extended (core delocalization) in the plane of the interface.

On the other hand, the coincidence lattice misfit F can also be accommodated by the presence of additional planes or missing planes inside the coincidence unit depending on the sign of the coincidence lattice misfit F. The occurrence of secondary dislocations in terms of additional planes in coincidence site lattice units is shown by the shaded region in Fig. 5.2 (d). One can imagine that this kind of defect will be more likely generated in systems with a larger deviation from perfect coincidence. Finally, the actual kind of secondary defect that is responsible for accommodating the coincidence lattice misfit will generally depend on the symmetry of the interface, the bonding type, and the amount of the coincidence lattice misfit [120].

Transmission Electron Microscopy studies The MnAs/GaAs interfacial structure was studied by transmission electron microscopy (TEM)[67, 107, 120]. The 7.5% misfit between the a spacing (in the hexagonal plane) of MnAs and GaAs (1 1 0) is released by a periodic array of misfit dislocations. The misfit along the c axis of MnAs amounts to about 30% a value that is enormously large for epitaxial growth. The epitaxy is possible because four MnAs (0 0 0 2) lattice spacings are nearly equal to six GaAs (2 2 0) lattice spacings. A more detailed investigation of this interface with GID is presented here that covers many other aspects of the interface.

5.1 Interface structure along the a axis of MnAs/GaAs (0 0 1)

Misfit dislocations in most semiconductor heterostructures are irregularly distributed at the heterointerface. This is because the dislocation glide planes are usually inclined to the heterointerface and dislocations are generated by extrinsic nucleation [121]. The dislocations are rather immobile in the interface plane and their lateral distribution is mostly determined by the random distribution of the nucleation sources. In contrast to this usually observed behavior, ordered array of misfit dislocations have been found by TEM [67] and by GID at the MnAs/GaAs (0 0 1) interface [76]. Periodic dislocation arrays can be formed if the dislocation glide plane is parallel to the interface. This would imply a high dislocation mobility along the interface. Repulsive dislocation interaction gives rise to equal spacings between the dislocations. Periodic arrangements of misfit dislocations are found in several other systems [Ag/MgO, [122] Fe/W, [123] PbTe/PbSe, [124] GaSb/GaAs, [125, 126] AlN/Si (1 1 1) [127]] with high lattice mismatch. These conditions are also met for the MnAs/GaAs heterostructures and a highly periodic array of misfit dislocations is formed at the interface.

5.1.1 Observation and orientation of the dislocation array

The interface is probed by recording in-plane x-ray diffraction profiles along the a axis in grazing incidence—grazing exit geometry. The scan geometry is shown schematically in Fig. 5.4. The reference frame is chosen such that the in-plane h and k axes are along GaAs [1 0 0] and GaAs [0 1 0], respectively. In this sketch, the large circles represent the integer-order GaAs reflections. The arrow indicates the scan direction. The solid circles correspond to satellite reflections due to the dislocation array observed in the measurements and are discussed below in detail. The squares represent the reflections of the

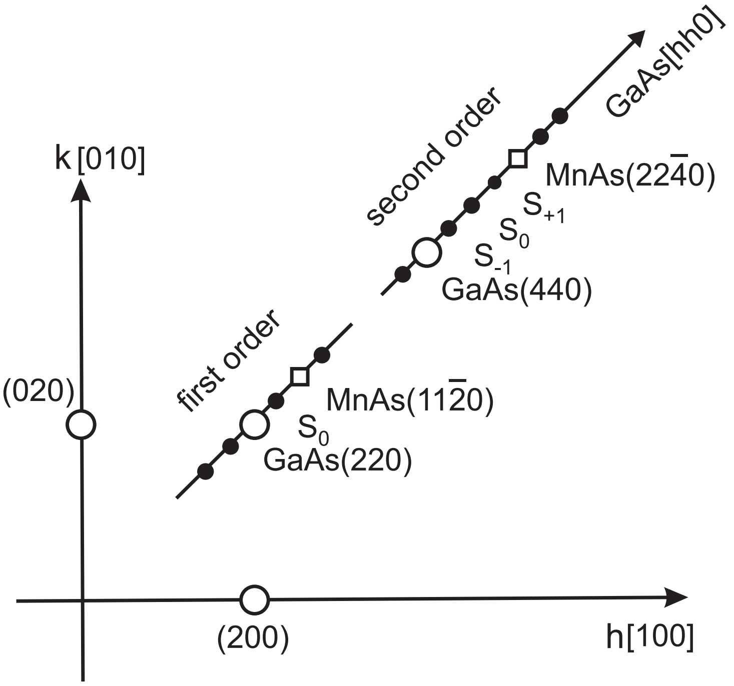

Figure 5.4: Schematic representation of the $(h\,k\,0)$ reciprocal space plane of MnAs/GaAs (0 0 1) with an array of misfit dislocations at the interface. The large open circles and the squares correspond to the GaAs and MnAs Bragg peaks, respectively. The filled circles represent the position of observed satellite reflections from the dislocation array along GaAs [0 0 1]. Two orders of scans with all observed reflections are included.

relaxed MnAs film. All reflections are extended in the surface normal direction due to the finite film thickness [13].

To study the MnAs/GaAs (0 0 1) interface, depth-tunable GID was applied [17, 128]. We varied the penetration depth of the x-rays by changing the incidence angle α_i of the 10 keV primary beam. For this energy, the critical angle for total external reflection of MnAs is $\alpha_c = \lambda\sqrt{(r_e\bar{\rho}_e/\pi)} = 0.27\,^\circ$, where $\bar{\rho}_e$ is the mean electron density and r_e the electron radius. We vary the grazing incidence angle through a range from below α_c to about $2.5\alpha_c$. The structural configuration of the interface is probed by measuring in in-plane geometry, $L = 0.05$ reciprocal lattice units (r.l.u.). Here, L is the (continuous) Miller index of the Bragg reflection $[h\,k\,L]$. We measure at non-zero Bragg angle, which is necessary to provide large momentum transfer parallel to the interface. The scans were performed at room temperature, after a high-temperature anneal of the sample at 400 °C.

The GID profiles measured through the first-order reflection (see schematics in Fig. 5.4) along the MnAs $[1\,1\,\bar{2}\,0]$ direction are shown in Fig. 5.5 (a). The grazing incidence angles are given to the right of each profile. Clearly visible are the GaAs (2 2 0) reflection and a split MnAs $(1\,1\,\bar{2}\,0)$ peak. The satellite reflections, S_i, are first observed at a grazing incidence angle of $0.3\,^\circ$ that is larger than α_c. The intensities of the satellite reflections increase with incidence angle, which means with increasing penetration depth of the x-rays. Higher-order satellites (S_{-3}, S_{+4}) are detected at $\alpha_i > 0.4\,^\circ$. We conclude that they are not originating from the surface or the near-surface region of the film but rather from the buried interface between MnAs and GaAs. The satellite S_0 is located exactly halfway between the substrate and the layer (middle of α and β MnAs peak) reflection.

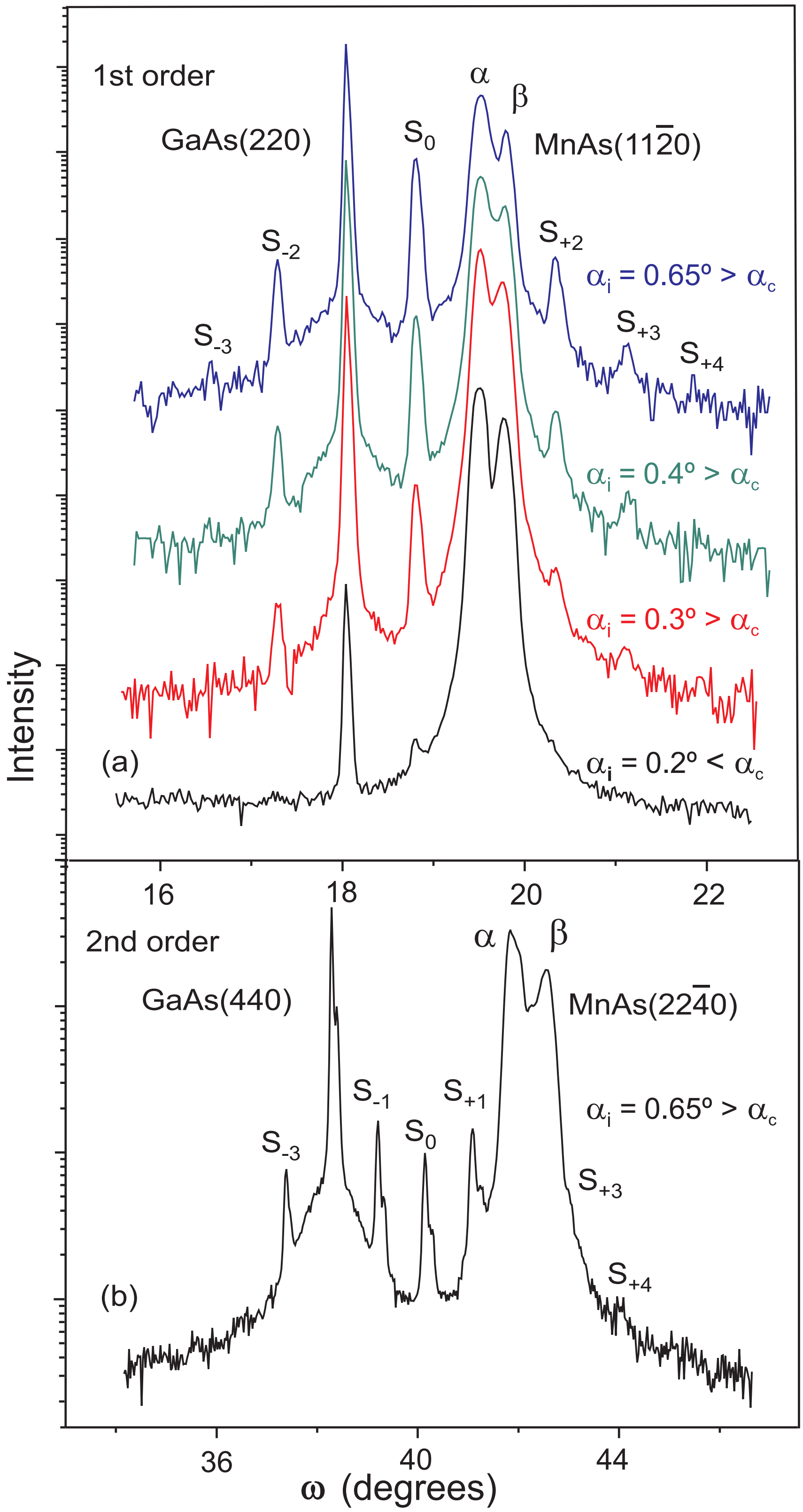

Figure 5.5: Radial ($\omega - 2\theta$) scans recorded along the MnAs [1 1 $\bar{2}$ 0] direction of the MnAs/GaAs (0 0 1) heterostructure for different grazing incidence angles α_i. (a) 1st and (b) 2nd order reflection. S_i indicates the satellites originating from the periodic array of misfit dislocations. The scans are measured at room temperature. Peaks labelled as α and β refer to the different phases of MnAs. The curves are shifted vertically for clarity. X-ray energy, 10 keV.

All observed satellite reflections are equally spaced.

MnAs is thermodynamically stable on GaAs [8, 129]. The possibility of another layer at the interface forming with a different lattice constant can therefore be ruled out. We attribute the equally spaced satellite reflections to the regularly spaced misfit dislocations formed at the interface. These results agree well with TEM studies on the same material system [67, 107]. The diffraction measurement averages over a much larger real-space distance than TEM and is representative of a large area of the sample. The appearance of the satellites in the radial scans along MnAs $[1\,1\bar{2}\,0]$ proves that the misfit dislocations are periodic in that direction.

The width of the satellite reflection S_0 in the $\omega - 2\theta$ scan at $\alpha_i = 0.65\,^\circ$ in Fig. 5.5 (a) is almost half the width of both the α and β MnAs peaks. Therefore, the width of the satellite reflections from the dislocation array is not limited by nonuniform strain of the layer, but determined by the much higher order of the GaAs substrate. A factor of 2 difference in the width of the satellite reflection and the layer reflection is also measured in the transverse scans. This demonstrates that the dislocation array is generally better ordered than the film itself.

5.1.2 Period and Burgers vector of the dislocation array

From the period of the satellites in Fig. 5.5 (a), we find a lateral period of the dislocation array, $\Lambda = 4.95 \pm 0.05$ nm. This compares favorably to the TEM result of $\Lambda = 4.5 \pm 0.5$ nm [67]. One dislocation in every 4.95 nm is sufficient to release the misfit $f = 7.5\%$ between the layer and the substrate. The in-plane component of the Burgers vector is $b = \Lambda f = 3.71\,\text{Å}$. Its length is equal to the spacing along a axis of MnAs, and is given by $\mathbf{b} = \frac{1}{3}[1\,1\,\bar{2}\,0]$. This is the shortest possible perfect dislocation Burgers vector in hexagonal close-packed structures. The line direction of the dislocations is along MnAs $[0\,0\,0\,1]$, so that the dislocation slip direction is $[1\,1\,\bar{2}\,0]$, [130] i.e. it lies in the plane of the interface. In terms of the GaAs lattice, the Burgers vector is equal to GaAs $[1\,1\,0]$.

The number of satellite reflections between the substrate and the layer reflections have a direct relation to the Burgers vector. The distance between the substrate and the satellite peaks is $\Delta Q{=}(2\pi/d)f$, where d is the lattice spacing for the reflection under consideration. The distance between the satellites is $\Delta q = 2\pi/\Lambda$. Dividing these two quantities and keeping in mind that $\Lambda = b/f$, we obtain:

$$\Delta Q/\Delta q = b/d. \tag{5.2}$$

For the MnAs $(1\,1\bar{2}\,0)$ reflection, only one satellite, S_0, is present halfway between the peaks, see Fig. 5.5 (a). We can then calculate $\Delta Q/\Delta q = 1/2$ and $b = 2d_{(1\,1\,\bar{2}\,0)}$. If the Burgers vector would be reduced to half, the satellite spacing would double and the satellites in the first order reflection would coincide with the main reflections from layer and substrate. The satellite reflections could then be observed outside of the main reflections, with the spacing equal to the separation of main reflections. This situation is actually realized at the MnAs/GaAs $(1\,1\,3)$A interface and discussed in chapter 6. The x-ray diffraction curve along the second-order reflection MnAs $(2\,2\,\bar{4}\,0)$ also reveals equally spaced satellite reflections, Fig. 5.5 (b). In this case three satellites are present between the main reflections. Equation (5.2) gives the same Burgers vector $b = 4d_{(2\,2\,\bar{4}\,0)} = 2d_{(1\,1\,\bar{2}\,0)}$.

Thus, the MnAs/GaAs $(0\,0\,1)$ interface is suitable for the formation of a periodic dislocation array. The main reasons for the periodic dislocation configuration are:

- The dislocation density is high due to the large misfit (~ 7.5% along the a axis of MnAs).

- The Burgers vector lies in the interface plane with the slip direction parallel to the interface. This facilitates the glide of the dislocations along the interface. At the growth temperature of 250 °C, the misfit dislocations are mobile enough to glide along the interface to form a regular structure to minimize the elastic energy of the system.

- The dislocations nucleate directly at the interface during growth and form a periodic structure even before coalescence (see Fig. 3.16).

- There exists a strong repulsive force between the dislocations.

Splitting of dislocation satellites The split of the MnAs film peaks due to the strain-mediated coexistence of the α and β MnAs phases at room temperature [110, 131] is observed in both reflection orders, namely the $(1\,1\,\bar{2}\,0)$ and $(2\,2\,\bar{4}\,0)$ reflections, see Fig. 5.5 (a, b). This is discussed in more detail in section 5.4. In addition, the second-order substrate GaAs $(4\,\bar{4}\,0)$ peak and the satellite peaks are split. The α MnAs and β MnAs domains arrange themselves in a stripe pattern to minimize the elastic energy [132] [see Fig. 5.18 (a)]. The α and β MnAs differ in their in-plane lattice constant by 1.2%. Therefore, the substrate lattice is strained underneath each α and β domain. This modulation leads to two different lattice parameters, which splits the GaAs $(4\,4\,0)$ reflection in Fig. 5.5 (b). The GaAs $(2\,2\,0)$ peak is also split. It is not resolved by the available resolution.

The splitting is therefore due to the epilayer exerting strain on the substrate. This strain decreases rapidly away from the interface. The penetration of the strain field into the substrate is comparable with the period of the α and β domain stripes, which is about 5 times larger than the film thickness[131, 132]. Since the dislocation array is also differently strained by the formation of the domain pattern, the spacing of the dislocations under the α and β domains are slightly different. Therefore even the satellite reflections are split. The amount of spliting of the satellite reflections is comparable to the amount of spliting of the substrate reflection. Hence, the complete interface structure is modulated by the formation of the α and β MnAs domains.

5.1.3 Crystal truncation rods of the dislocation satellites

Intensity in reciprocal space which is sharp in two dimensions and diffuse in one direction is refereed to as rod of scattering. Such rods must arise from a periodic object that is truncated in one dimension and extended in the other two dimension and known as crystal truncation rods (CTRs) [13, 14]. The MnAs/GaAs $(0\,0\,1)$ interface with its periodic misfit dislocations can be viewed as a thin layer at the interface with a non-homogeneous distribution of strain. The CTR of a satellite reflection arises from the periodic dislocations at the interface where the strain field due to the dislocations is distributed inhomogeneously. Therefore, the intensity distribution along the surface normal direction provides a direct measure of the layer thickness at the interface.

We have measured the intensity profiles along the crystal truncation rods (CTRs) of several satellite reflections $(h\,k\,L)$ as a function of L. During these measurements, the

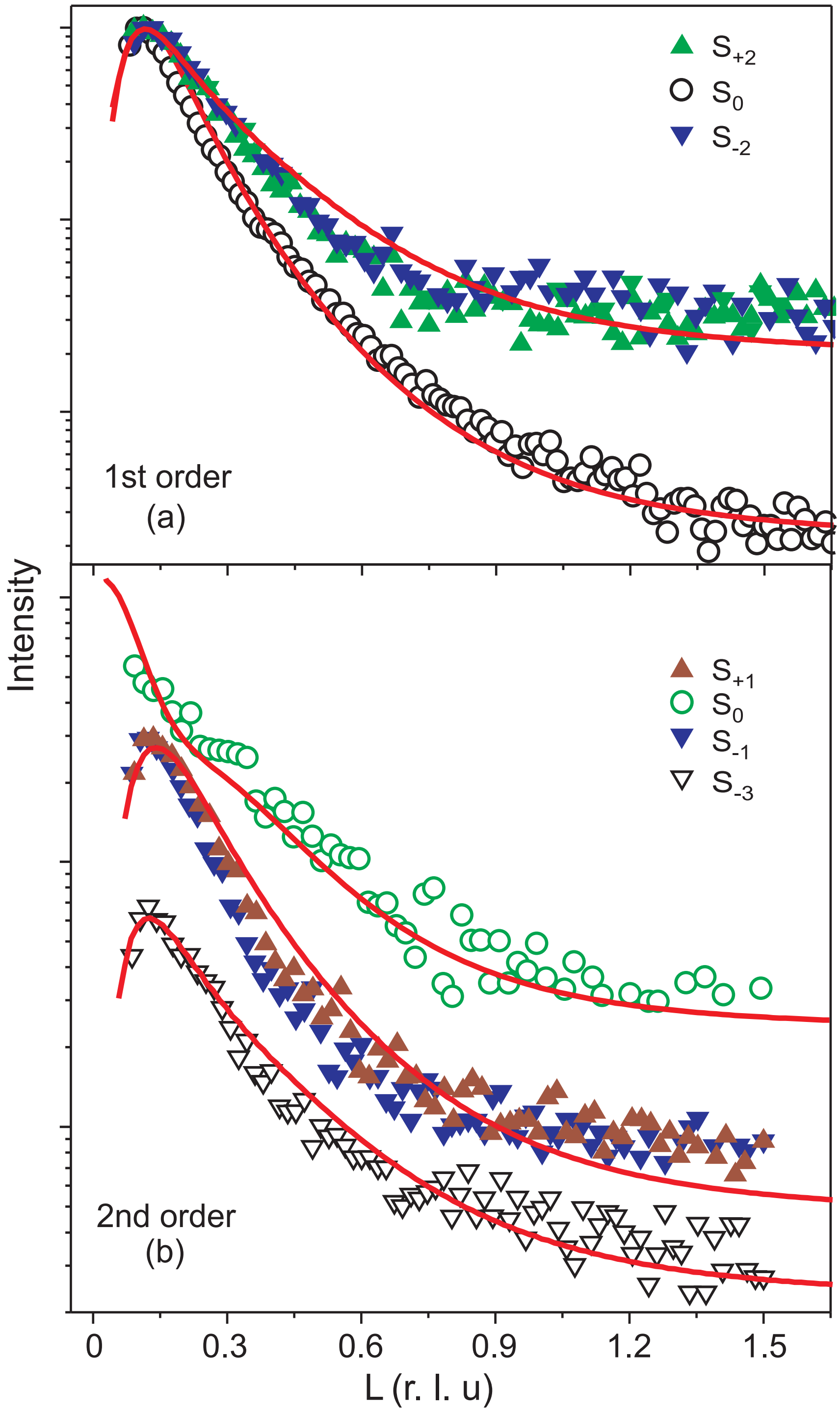

Figure 5.6: Intensity variation along the crystal truncation rods of different observed satellites at the 1st and 2nd order reflections shown in Fig. 5.5 (a) and (b). The continuous lines show the calculated CTRs of the different satellites. No fit parameters except a constant scaling factor are used to match the calculated CTRs with the measured intensity profiles. The x-ray energy is 10 keV.

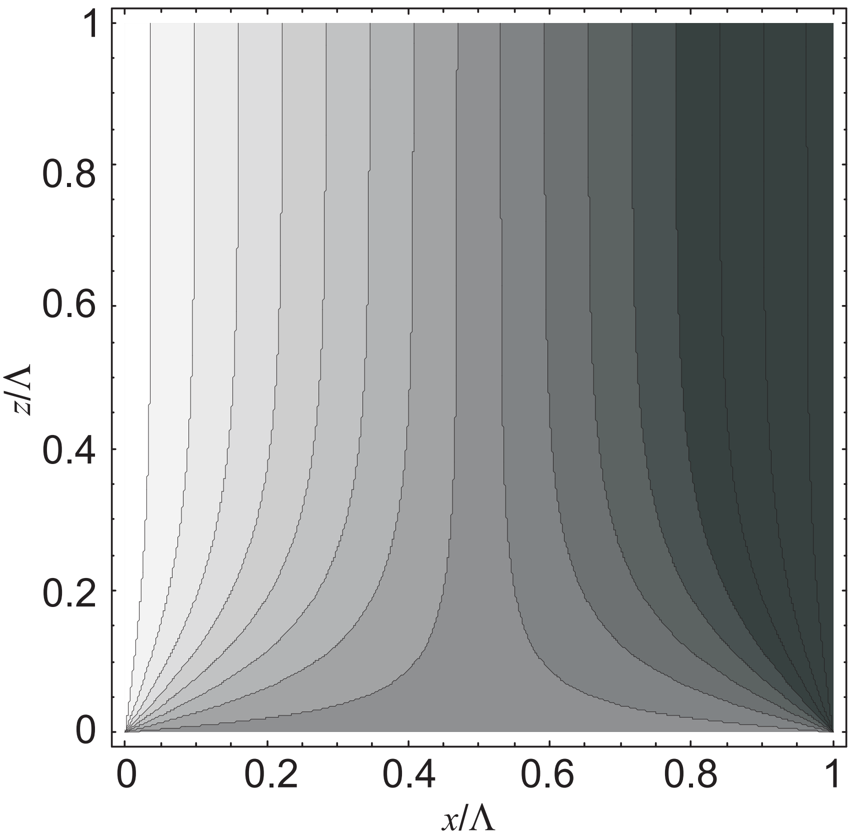

Figure 5.7: Contour plot of the displacement field due to the periodic dislocations at the interface. The distribution in the plane normal to the surface and normal to the dislocation lines is according to Eq. (5.7). The contour lines are almost parallel to each other for a thickness larger than Λ/π.

grazing incidence angle is fixed and the exit angle is varied. The crystal truncation rods of several satellite reflections in the first diffraction order [see Fig. 5.5 (a)] are shown in Fig. 5.6 (a). The measured intensity profiles along the CTRs of satellites S_{-2} and S_{+2} are very similar. The out-of-plane scattering along each CTR reflects the smoothing of the nonuniform strain when going along the interface normal.

The intensity distribution along a satellite rod is calculated in the kinematical approximation,

$$I_n(q) = \left| \int e^{iQ_n u_x(x,z) + iq_z z} dx dz \right|^2 . \tag{5.3}$$

Here the coordinate x is along the interface in the direction of periodicity and z is the coordinate along the interface normal, $u_x(x,z)$ is the in-plane component of the displacement field of the periodic dislocation array, $q_z = (2\pi/a_s)L$, and $Q_n = (2\pi/\Lambda)n$ (here n is the number of the satellite S_n).

Displacement field The displacement field due to a single edge dislocation along the dislocation line and in direction perpendicular to the dislocation line is given by [130]

$$U_z(x,z) = -\frac{b}{2\pi} \left[\frac{1-2\nu}{4(1-\nu)} \ln(x^2+z^2) + \frac{x^2-z^2}{4(1-\nu)(x^2+z^2)} \right] + C \tag{5.4}$$

$$U_x(x,z) = \frac{b}{2\pi}\left[-\arctan(x/z) + \frac{xz}{2(1-\nu)(x^2+z^2)}\right] + C \tag{5.5}$$

Where ν is the Poisson ratio. The coordinate z is along normal to the interface plane. The misfit dislocations at the interface is regularly arranged along x direction with an average spacing of Λ. To calculation of intensity along the CTR, we only consider the displacement along the plane of the interface. The resulting displacement field due the periodic array of dislocations is calculated by summing the displacements due to the individual dislocations:

$$u_x(x,z) \;=\; \frac{b}{2\pi}\sum_{n=-\infty}^{\infty}\left[-\arctan\left(\frac{x+n\Lambda}{z}\right) + \frac{(x+n\Lambda)z}{2(1-\nu)\{(x+n\Lambda)^2+z^2\}}\right]\;. \tag{5.6}$$

The analytical formulas for strain fields of various dislocation arrays can be found in the literature [130], but the displacement fields are not given. We therefore determined the displacement field, and the result is

$$\begin{aligned} u_x(x,z) \;&=\; \frac{b}{2\pi}\left\{\arctan\left[\frac{\tanh(\pi z/\Lambda)}{\tan(\pi x/\Lambda)}\right]\right. \\ &+\; \left.\frac{\pi z/\Lambda}{2(1-\nu)}\frac{\sin(2\pi x/\Lambda)}{\cosh(2\pi z/\Lambda)-\cos(2\pi x/\Lambda)}\right\}\;. \end{aligned} \tag{5.7}$$

In the limit $x, z \ll \Lambda$, this expression reduces to that of an individual dislocation. When $z \gg \Lambda/\pi$, Eq. (5.7) gives rise to a uniform strain $u_{xx} = (b/2\Lambda)\mathrm{sign}(z)$, while the nonuniform strain decays exponentially. Thus, the nonuniform strain is confined to a stripe $|z| < \Lambda/\pi$. The displacement $u_x(x,z)$ calculated by Eq. (5.7) is shown in Fig. 5.7. As seen from the Fig. 5.7, for $|z| > \Lambda/\pi$ the contour lines are almost parallel to each other indicating a constant displacement gradient.

The intensity profiles calculated by Eq. (5.3) for different satellite reflections are shown as solid lines in Fig. 5.6 (a). Since we are measuring in the regime of small perpendicular momentum transfer (L values below 1.6 r.l.u.), the correction factors to the measured intensity are almost constant in the range considered [25]. We obtain an excellent agreement between the measured and calculated intensities for different orders of the satellites without introducing any fit parameters (except for scale and background). Figure 5.6 (b) presents the intensity profiles along the CTRs of four satellites (S_0,$S_{\pm1}$, S_{-3}) of the second-order reflection, Fig. 5.5 (b). All the profiles show a similar intensity variation. This demonstrates that they originate from the same thin interfacial layer. The calculated intensity agrees well for the different order satellite reflections.

The thickness of the stripe at the interface with inhomogeneous strain ($|z| < \Lambda/\pi$) is directly proportional to the period of the dislocations. For a period of $\Lambda = 4.95$ nm, we estimate the thickness of the inhomogeneously strained layer of the film to Λ/π =1.6 nm. A very similar value can be obtained from the FWHM of the measured intensity of the satellite CTRs.

5.2 Interface configuration along the c axis of MnAs/GaAs (0 0 1)

5.2.1 GID profiles along the c axis

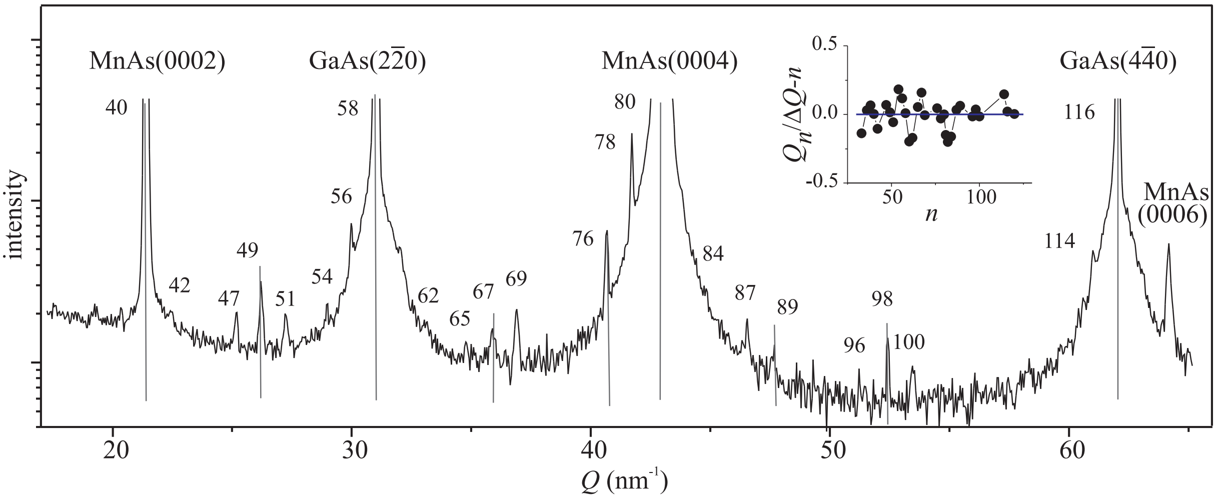

Figure 5.8: Grazing incidence x-ray diffraction ($\omega - 2\theta$ scan) of a MnAs epitaxial film on GaAs (0 0 1). The incidence angle $\alpha_i = 0.65° = 2.4\,\alpha_c$. The numbers at the peaks are $n = Q/\Delta Q$, with $\Delta Q = 0.5416$ nm^{-1}. The insert shows that the deviations from the integer values, $Q_n/\Delta Q - n$, are small and random.

A radial x-ray diffraction profile ($\omega - 2\theta$ scan) over a wide angular range, spanning over three reflection orders of MnAs, from (0 0 0 2) to (0 0 0 6), and two reflection orders of GaAs, (2 $\bar{2}$ 0) and (4 $\bar{4}$ 0) along the MnAs c axis is shown in Fig. 5.8. The measurements were done at an incidence angle of $\alpha_i = 0.65°$, which is more than two times the critical angle. The satellite reflections are clearly visible between the main peaks. But the spacing of the satellites are different in comparison to that seen along the a axis. Once again, TEM measurements show that interfacial misfit dislocations (i.e., singularities in the atomic displacements) are absent at the interface along the c axis [67]. Therefore the satellites are not due to periodic dislocations. The numbering of the satellites will become clear from the analysis below.

A part of the curve between the MnAs (0 0 0 2) and GaAs (2 $\bar{2}$ 0) reflections was measured at different incidence angles and is shown in Fig. 5.9. The satellites become more intense when the incidence angle is increased above the critical angle α_c and satellites vanish when the incidence angle is smaller than α_c. The dependence of the satellite reflection on the probing depth is a clear evidence that the satellites originate from the MnAs/GaAs heteroepitaxial interface; when the incidence angle is smaller than α_c, the radiation does not penetrate to the interface and its structure is not seen.

5.2.2 Origin of the satellites

The positions of the main MnAs and GaAs peaks are $Q_{\mathrm{MnAs}(0\,0\,0\,2)} = 21.665$ nm^{-1} and $Q_{\mathrm{GaAs}(2\,\bar{2}\,0)} = 31.416$ nm^{-1}. Their ratio is $Q_{\mathrm{MnAs}(0\,0\,0\,2)}/Q_{\mathrm{GaAs}(2\,\bar{2}\,0)} = 1.4501 \approx \frac{29}{20}$. Therefore a coincidence lattice of 29 GaAs (2 $\bar{2}$ 0) planes vs. 20 MnAs (0 0 0 2) planes at the interface is possible. Such units corresponding to the coincidence lattice period given by

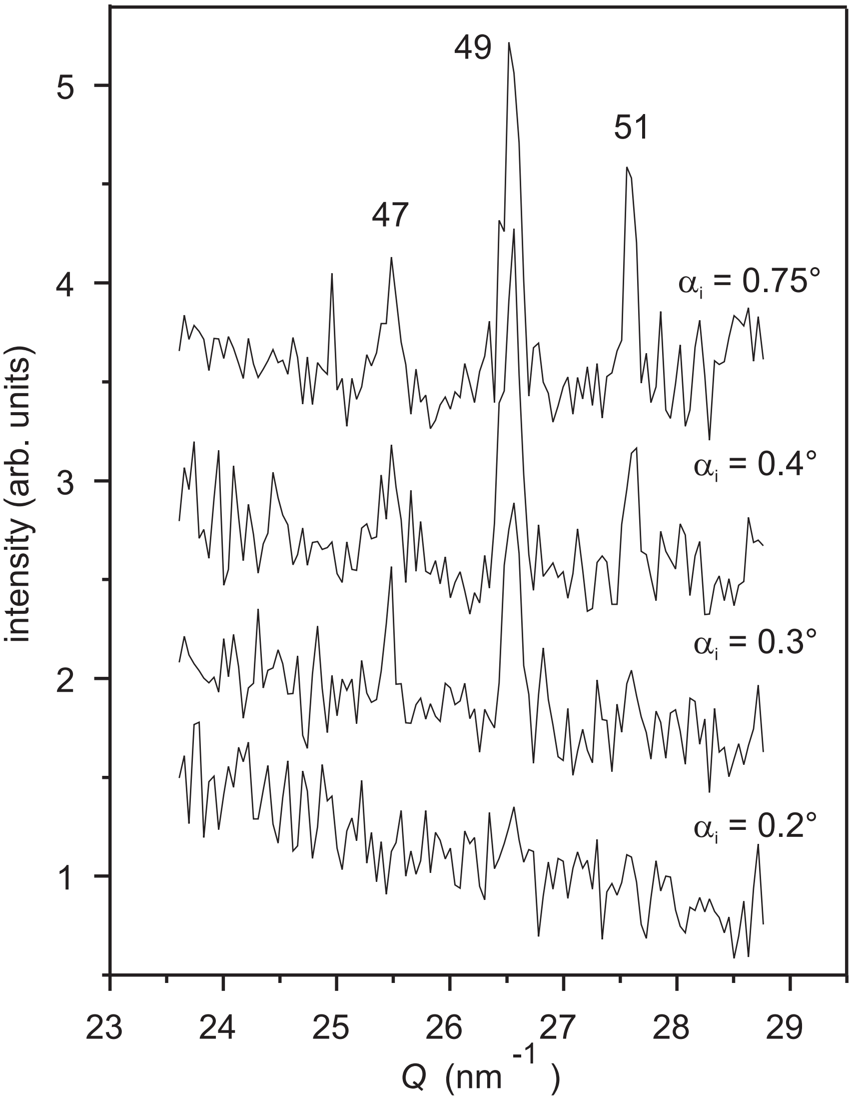

Figure 5.9: Grazing incidence x-ray diffraction ($\omega - 2\theta$ scans) at different incidence angles α_i. The critical angle of total external reflection is $\alpha_c = 0.27°$. The satellites only appear for $\alpha_i > \alpha_c$. The satellites have the same numbers as in Fig. 5.8.

the distance between satellites labelled as 49 and 51 in Fig. 5.8. However, the distance between the satellites labelled 51 and 54 is 1.5 times larger (also the distance between the MnAs (0 0 0 4) and the satellite 87 is 3.5 times the periodicity between 49 and 51). This half-integer number indicates that the period of the structure is in fact two times larger. We take $\Delta Q = 0.5416$ nm^{-1} as the unit distance between the satellites. Then, all peaks in Fig. 5.8 are at integer positions $Q_n = n\Delta Q$. The numbers n are shown at the peaks. We check the assignment by calculating the differences, $Q_n/\Delta Q - n$, for all peaks where the values Q_n are obtained from an independent fit of each peak. The results are shown in the inset of Fig. 5.8. We see the deviations from integer numbers are random and do not exceed 0.2. The period of the structure is $p = 2\pi/\Delta Q = 11.60$ nm. The numbering scheme is defined such that the peak number is equal to the number of the corresponding spacings in the period. Hence, the numbers 40 and 58 of the MnAs (0 0 0 2) and GaAs $(2\,\bar{2}\,0)$ peaks mean that the period of the interfacial structure consists of 40

MnAs (0 0 0 2) planes and 58 GaAs (2 $\bar{2}$ 0) planes, respectively.

The relatively strong satellites are separated by $9\Delta Q$. Satellite 49 is a clear example; it is at a distance of 9 from both the MnAs (0 0 0 2) and GaAs (2 $\bar{2}$ 0) peaks. Corresponding periods are marked by vertical gray lines in Fig. 5.8. We conclude therefore that the period consists of 9 almost equal subunits. These strong satellites, as well as the main reflections, have further satellites at a distance of 2 (as an example take satellite 47 and 51). Thus, a weaker modulation with a period equal to 1/2 of the period of the whole structure is present.

The separation of the relatively strong satellites (shown as vertical lines) $\Delta Q' = 4.819$ nm^{-1} corresponds to a real space distance of 1.3 nm. So the period of the structure (11.6 nm) contains 9 subunits. Like the common case of misfit dislocations, where n atomic planes on ones side of the interface fit into $n+1$ planes on the other side, we find that each subunit in the period consists of a non-integer number of atomic planes. When the period of 40 vs. 58 planes is subdivided in 9 units, each unit contains approximately 4.4 vs. 6.4 planes. The coincidence between 4.4 MnAs (0 0 0 2) planes and 6.4 GaAs (2 $\bar{2}$ 0) planes is sufficient to release all the misfit. However, the TEM micrographs of the MnAs/GaAs interface were interpreted as a match of 4 MnAs (0 0 0 2) planes to 6 GaAs (2 $\bar{2}$ 0) planes which releases 25% of the misfit. The remaining 5% is released by appearance of additional planes in the coincidence unit. The subunits with additional planes such as 6 to 8 match [67, 107] and 5 to 6 match [88] is reported. The formation of a coincidence lattice with a 4th to 6th plane match is more reasonable. Presumably, the fractional planes present in each subunit appears as extra planes in every third subunit. These units with additional plane matches are the secondary dislocations in the coincidence site lattice. However, for a detailed understanding and to resolve all the satellites measurements at synchrotron with high photon flux and improved signal to noise ratio is necessary. In conclusion, we find that that a basic unit exists at the interface with non-integer plane matches which releases most of the mismatch. One period at the interface consists of 9 basic units. The MnAs is weakly bonded to the GaAs substrate along the c axis.

5.3 Effect of in situ thermal annealing

We studied the effect of post-growth thermal annealing on the crystal quality of the MnAs layer as well as on the ordering of the dislocation array at the interface. The annealing was carried out *in situ* at 400°C for 10 minutes with heating and cooling rates of 15 °C min^{-1}. The annealing was done without cooling the sample to room temperature after growth and in an arsenic-rich ambient to prevent As desorption from the MnAs surface. Growth and annealing were therefore both carried out within the γ phase of MnAs. Radial scans along the MnAs [1 1 $\bar{2}$ 0] direction recorded during the annealing cycle are shown in Fig. 5.10. The thermal expansion coefficient of γ MnAs in the basal plane is 4.3×10^{-5}K^{-1} [46], which is almost one order in magnitude larger than that of GaAs (5.7×10^{-6} K^{-1}).

5.3.1 Effect on crystal quality

During heating, the MnAs (1 1 $\bar{2}$ 0) peak shifts towards lower angles. The temperature dependence of the in-plane lattice parameter a during annealing is deduced from the MnAs peak position and is shown in Fig. 5.11 (a). A net increase of 0.43% for the in-plane lattice

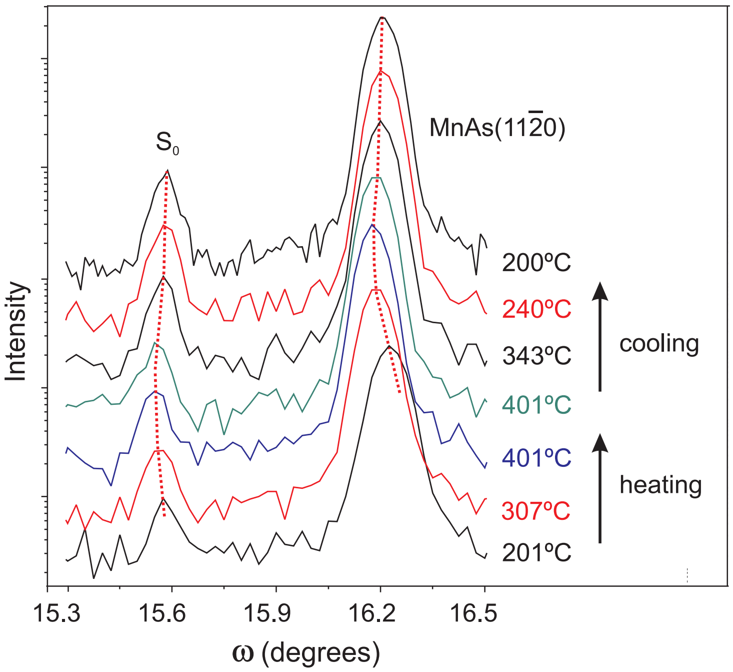

Figure 5.10: Radial ($\omega - 2\theta$) scans along the MnAs $[1\,1\,\bar{2}\,0]$ direction measured in grazing incidence geometry during *in situ* postgrowth annealing. The scans were recorded at an incidence angle of 0.3 °. The temperature is given at the right hand side of each curve. For clarity, the curves are shifted in the vertical direction. The dotted lines on the curves are guides to the eye for the peak position at different temperatures. X-ray energy, 12 keV.

spacing is observed during heating to 400 °C. The increase in lattice parameter due to only thermal expansion is calculated to be 0.18%. The remaining 0.25% can be attributed to the annealing-induced relaxation of the layer. We cannot rule out the intermixing of Mn and Ga, which was found in an annealing study of MnAs film on GaAs (0 0 1) without As-overpressure [133]. However, we note that the lattice spacings in our experiment approach the bulk MnAs values. This indicates the relaxation of residual strain from the MnAs layer during annealing.

To investigate the effect of annealing on the in-plane order of the MnAs layer, we analyze the MnAs $(1\,1\,\bar{2}\,0)$ peak widths in the radial scans along the *a* axis. The correlation length along MnAs $[1\,1\,\bar{2}\,0]$ as a function of annealing temperature is shown in Fig. 5.11 (b). It is obtained from the FWHM of the peaks (corrected for the instrumental resolution) using Scherrer's formula [11]. A net 20% increase of the in-plane correlation length is observed, indicating a clear improvement in the crystal quality of the layer. This presumably takes place by the removal of the defects present at domain boundaries and the coalescence of smaller domains during annealing. Also, the transverse scans through the MnAs peaks show a decrease in peak width from 0.43 ° before annealing to 0.24 ° after the thermal treatment. As discussed earlier in section 4.4, the width of the transverse scans can be completely attributed to the in-plane mosaic spread. Therefore, the mosaic spread of the layer is reduced by almost 50%. The grains are less twisted around the surface normal, which also implies annihilation of defects at the grain boundaries. The integrated intensity of the MnAs peak, which should remain the same according to kinematical theory, increases at the same time by a factor of 1.8 as shown in Fig. 5.11 (c). This

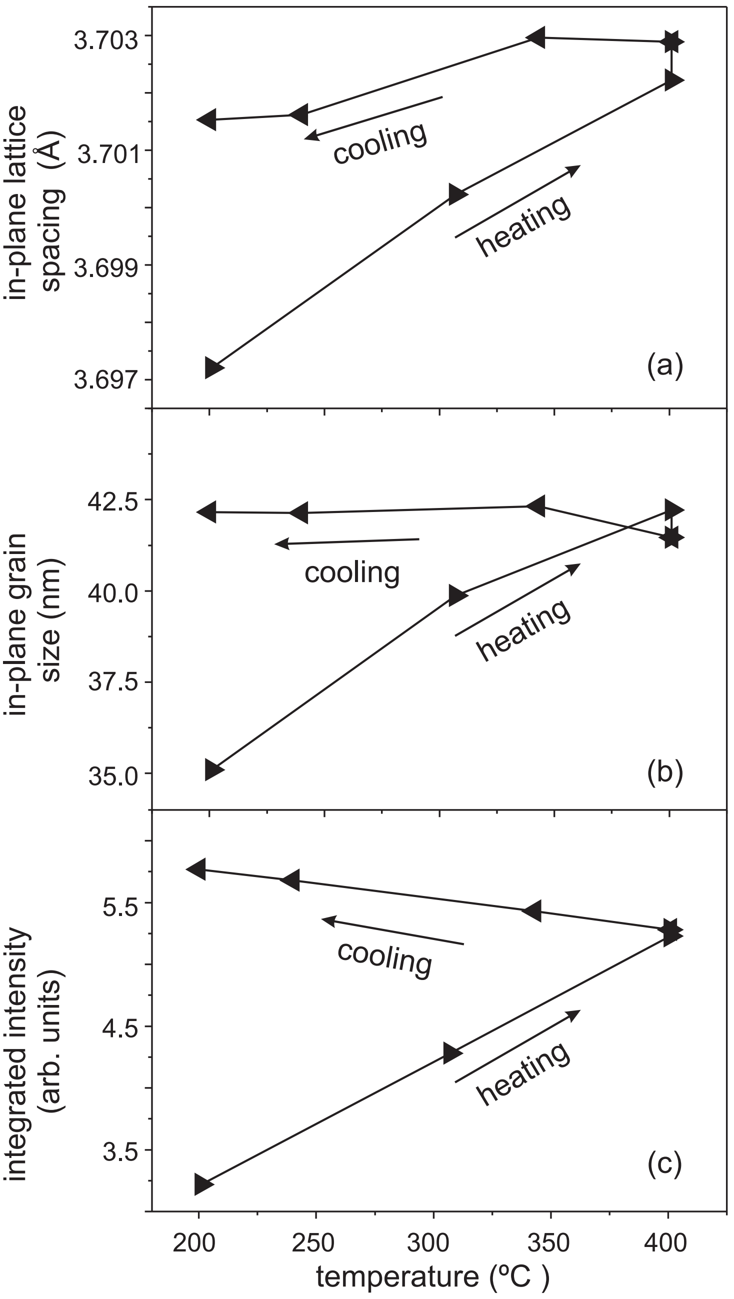

Figure 5.11: The evolution of in-plane lattice spacing (a), in-plane grain size (b) and integrated intensity (c) along the *a* axis during *in situ* postgrowth thermal annealing as a function of annealing temperature. The arrows indicate the direction of heating to 400 °C and subsequent cooling to 200 °C.

increase may be attributed to the enhancement of the crystal quality by the removal of lattice defects and distortions, which reduces the static Debye-Waller factor by increasing the order in the film.

5.3.2 Effect on interface structure

Since the thermal expansion coefficient of MnAs is notably larger than that of GaAs, the misfit decreases with rising temperature. The satellite peak, S_0, changes its position in the

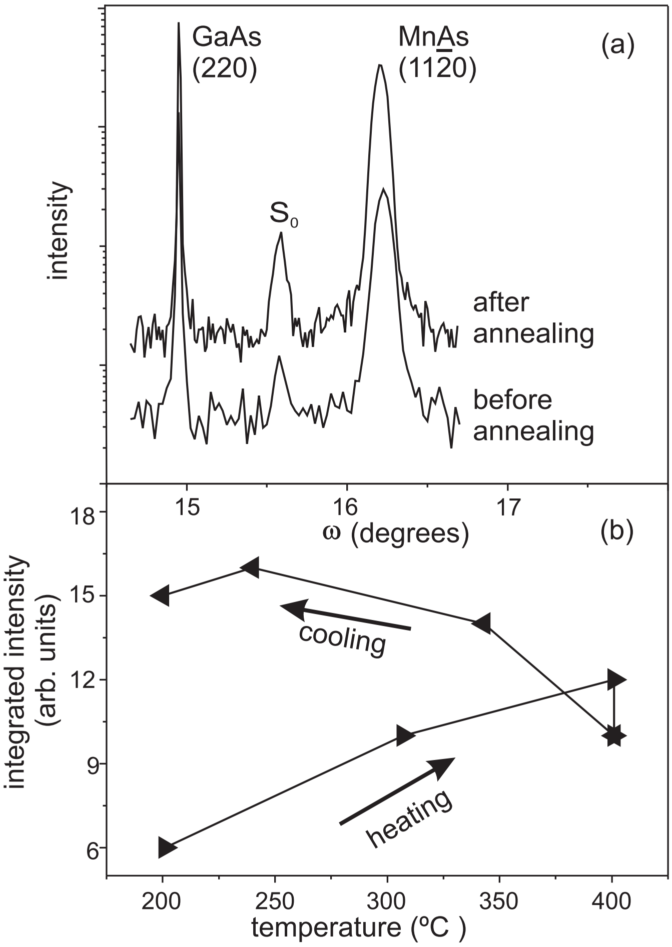

Figure 5.12: (a) Radial ($\omega/2\theta$) scans along the MnAs $[1\,1\bar{2}\,0]$ direction measured at 200 °C before and after annealing. (b) Evolution of integrated intensity of the S_0 satellite during annealing. The intensity increases 2.5 times during annealing. Arrows indicate heating and cooling sequence. The x-ray energy is 12 keV.

same way as the layer peak, as shown by the dotted lines in Fig. 5.10. The satellite peak always stays in the center between the layer and the substrate peak at all temperatures. Hence, the dislocation network changes its period to accommodate the lattice parameter misfit at any given temperature.

Figure 5.12 (a) shows two diffraction curves, before and after annealing, both at 200 °C. The integrated intensity of the satellite reflection S_0 is plotted as a function of annealing temperature in Fig. 5.12 (b). The increase in integrated intensity by a factor 2.5 clearly indicates an improvement in the periodicity of the dislocation array. Therefore, annealing has a positive impact on the dislocation array, and improves the ordering of dislocations. The term ordering means that the dislocation lines are more perfect, straight and regular with a smaller number of kinks.

5.4 Phase transitions in MnAs epitaxial films

MnAs films show a coupled magnetic and structural phase transition at 40 °C. An overview of the phase transitions in bulk MnAs as a function of temperature is shown in Fig. 5.13. The magnetic as well as structural phase transition in bulk MnAs proceeds abruptly. In contrast to bulk MnAs, the first order phase transition in epitaxial MnAs films at 40 °C does not proceed abruptly. Rather, the simultaneous existence of the α and β phases is observed over a temperature range starting from 40 °C to 15 °C [131, 132]. This appears to be a violation of Gibb's phase rule at first sight. This puzzle was solved by Kaganer *et al.* [110, 131]. They explained the origin of the phase coexistence as the result of epitaxial constraints imposed by the substrate on the film. It has also been shown that the magnetization increases continuously with the increase of the α MnAs phase until the whole system is in the ferromagnetic phase at around 15 °C [134]. The α/β phase transition is first order in nature and epitaxial constraints imposed by the substrate are also responsible for the change of various magnetic properties such as anisotropy and coercivity [135]. Here we present co-planar out-of-plane diffraction and grazing incidence in-plane x-ray diffraction measurements of the phase transition in MnAs films.

Figure 5.14 presents the temperature dependent out-of-plane x-ray diffraction curves measured in co-planner geometry near the phase transition temperature. The measurements are done using a laboratory x-ray source. The temperature was kept constant while recording each curve. The sample rotation angle θ was measured with respect to the position of the GaAs $(0\,0\,2)$ substrate peak, which was calibrated to zero. The single peak observed well below the transition temperature originates from the α MnAs $(1\,\bar{1}\,0\,0)$ reflection, and the one above the transition temperature originates from the β MnAs $(0\,2\,0)$ reflection. The β MnAs $(0\,2\,0)$ peak has a higher peak intensity and a larger integrated intensity than the α MnAs $(1\,\bar{1}\,0\,0)$ reflection. Near the transition temperature, a continuous transformation from one peak to the other is observed. Both the α and the β peaks coexist in a temperature interval of about 20 °C. The peaks are well fitted by sums of two Gaussians with each peak corresponding to one of the two phases. We successfully fitted the peak positions and the integrated intensities.

The temperature dependent in-plane diffraction curves measured in grazing incidence geometry are shown in Fig. 5.15. This measurements are done *in situ* using synchrotron radiation. The temperature is calibrated by comparing the phase composition of the in-plane and out-of-plane measurements. We estimate an error of about 5 °C in temperature measurement. Unlike the previous measurements, the presence of two peaks corresponding to hexagonal α MnAs and orthorhombic β MnAs is clearly seen in the phase coexistence regime. The measured profiles are fitted well with a sum of two Gaussians. Since the struc-

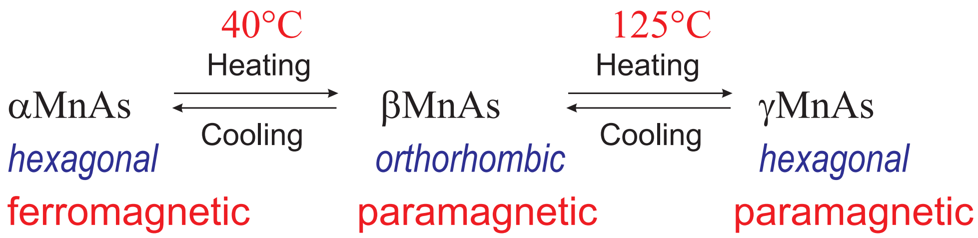

Figure 5.13: Overview of the bulk MnAs phases and their crystal structure as a function of temperature.

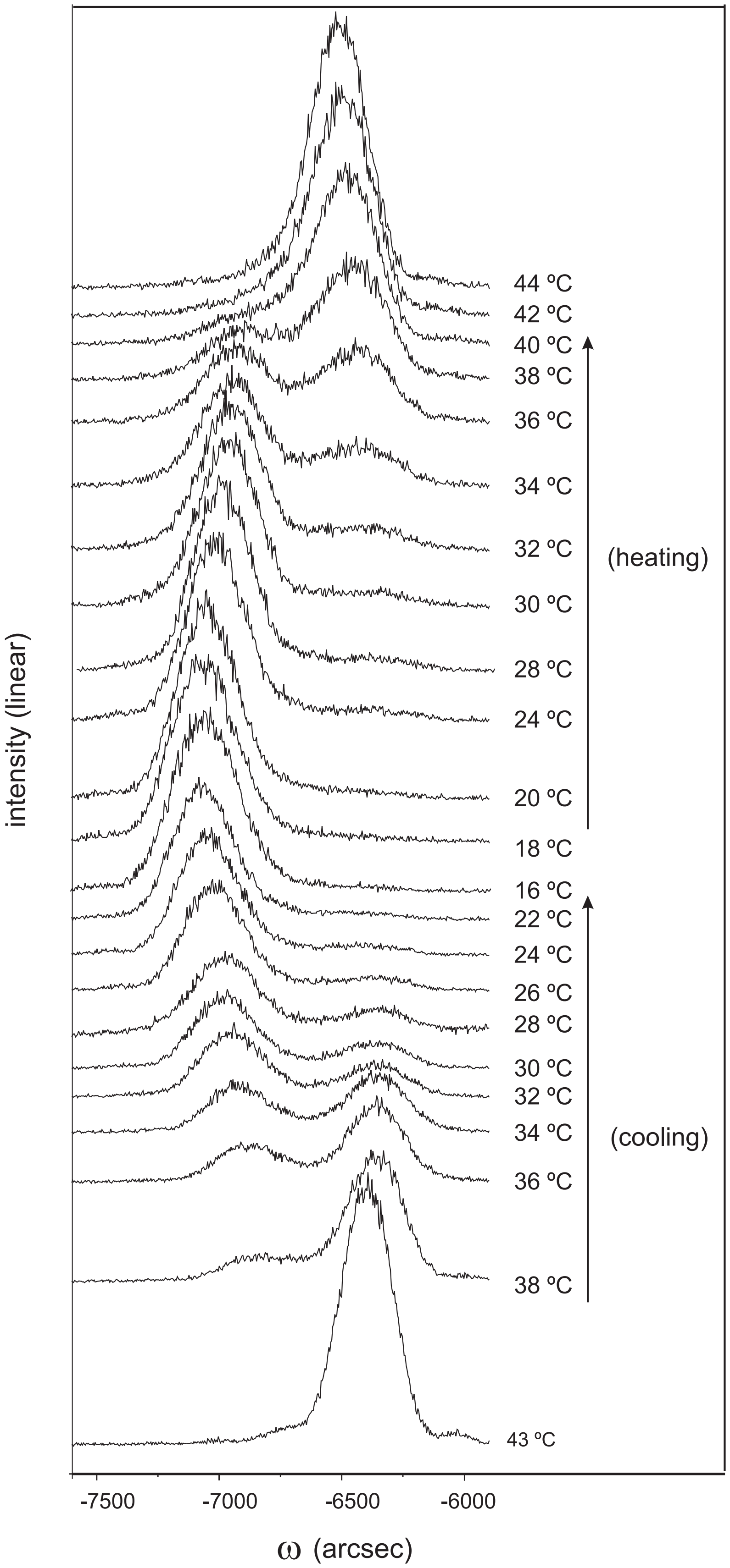

Figure 5.14: $\theta - 2\theta$ scans of MnAs samples during cooling and heating recorded in the co-planner geometry. The peak on the left side is the α MnAs peak and the peak on the right side is the β MnAs peak. The temperature corresponding to each measurement is given at the right hand side. For clarity, the curves are shifted vertically.

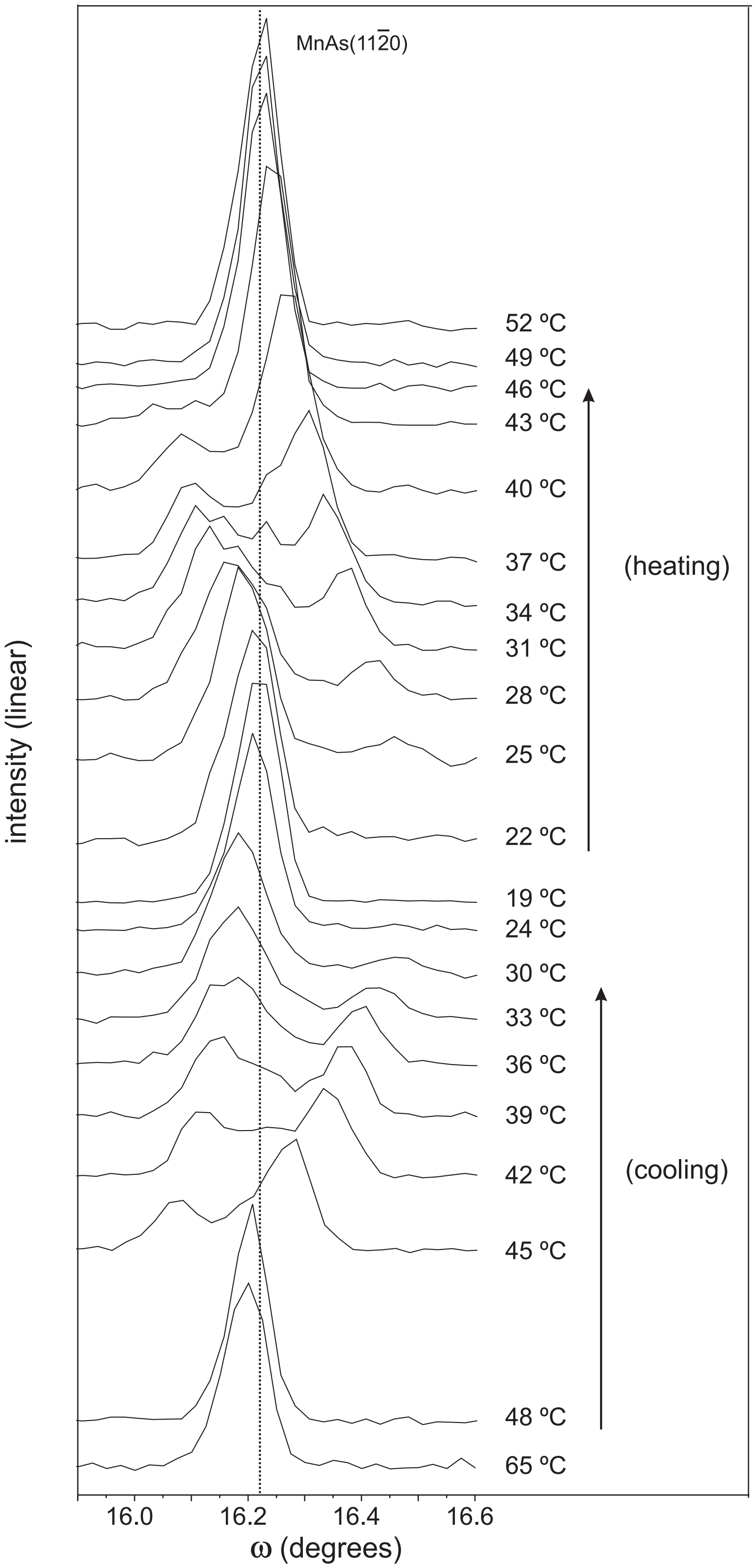

Figure 5.15: In-plane radial ($\omega - 2\theta$) scans of a MnAs $(1\,1\,\bar{2}\,0)$ reflection recorded in the GID geometry during a cooling and heating cycle. The peak on the left side is the α MnAs peak and the peak in the right side is the β MnAs peak. The temperature corresponding to each measurement is given at the right hand side. The curves are shifted vertically for clarity. The dotted line is a guide to eye to follow the peak shifts from the mean position.

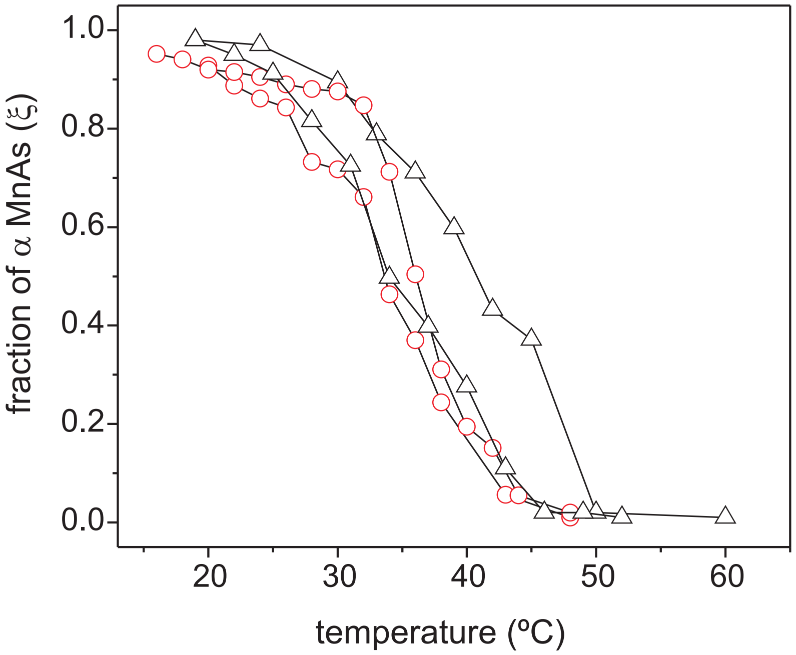

Figure 5.16: Temperature dependence of the fraction of α MnAs phase calculated from the integrated intensities of the α MnAs peak. The circles and triangles represent the alpha phase fraction measured from the x-ray diffraction profiles in Fig. 5.14 and Fig. 5.15, respectively. In both cases a hysteresis of the phase composition is observed.

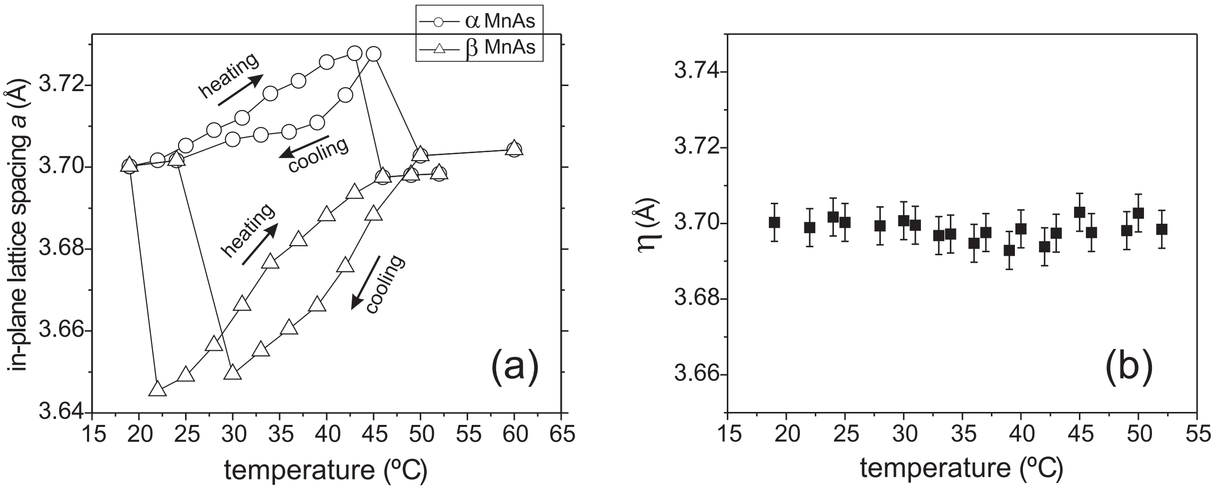

Figure 5.17: (a) In-plane lattice spacing of α and β MnAs calculated from the respective peak positions in Fig. 5.15 as a function of temperature. (b) Variation of mean lattice spacing of both phases shown as a function of temperature.

ture factors of both α and β MnAs reflections are almost equal, the ratio of the integrated intensities of α MnAs and β MnAs peaks are proportional to the volume fractions of the phases in the film. The phase fraction of α MnAs (ξ) is calculated from the fits and shown in Fig. 5.16. The fraction of the α MnAs phase increases almost linearly during cooling for the in-plane and out-of-plane measurement. The phase coexistence is accompanied by a temperature hysteresis. The thermal hysteretic behavior is a sample dependent effect and more pronounced in thicker samples [131, 134]. The change of the phase fraction proceeds without nucleation by a barrierless motion of the domain walls [131].

Figure 5.17 (a) shows the variation of the in-plane spacing a of α and β MnAs. During cooling, at about 45 °C the α MnAs starts to form. This is confirmed by the sudden appearance of the α MnAs $(1\,\bar{1}\,0\,0)$ peak with a spacing of 3.727 Å. Upon further cooling the in-plane spacing of both phases decreases simultaneously, and around 22 °C the beta phase completely disappears. The lattice spacing approaches the equilibrium spacing of 3.7001±0.005 Å. An opposite behavior is observed during heating cycle. An abrupt decrease of the in-plane lattice parameter upon the formation of β MnAs is noticed at about 23 °C. We also observe a thermal hysteresis. The change of the in-plane lattice parameter is stronger in the β MnAs phase compared to the α MnAs phase.

The significant difference between the in-plane (Fig. 5.15) and out-of-plane (Fig. 5.14) diffraction profiles is noticed at well above and below the phase coexistence regime. The α and β MnAs peaks have different positions in out-of-plane measurements, whereas the positions are the same in in-plane measurements. Therefore, both α and β MnAs have the same in-plane lattice parameter as a single phase. We calculate the average in-plane lattice spacing in the phase coexistence regime. The average in-plane lattice constant of the whole film is defined by

$$\eta = \xi \, a_{\,\alpha\mathrm{MnAs}} \; + \; (1-\xi) \, a_{\,\beta\mathrm{MnAs}} \, . \tag{5.8}$$

Figure 5.17 (b) shows the variation of η as a function of temperature. It is practically constant throughout the temperature cycle. The value is calculated to 3.7001 ± 0.005 Å, which is an intermediate value between the reported bulk lattice parameter of α and β MnAs [46]. This proves that the mean spacing of both phases is always constant. This invariant in-plane spacing is a result of the epitaxial constraint the substrate exerts on the layer.

Domain period At the phase transition of MnAs/GaAs heterostructure, the unit cell shrinks in the hexagonal plane, while the height of the prism does not change. The phase coexistence is caused by the epitaxial constraint on the mean lateral lattice parameter and gives rise to periodic elastic domains of both phases. The lattice parameter in the hexagonal plane is discontinuous at the phase transition, and the spacing along the c axis remains constant. Since the c axis is oriented parallel to the GaAs $(0\,0\,1)$ surface, this results in a high degree of in-plane anisotropy in the film. Therefore, the elastic domains of both α and β MnAs form periodic stripes of alternating domains extend along the c axis as shown in the atomic force micrograph Fig. 5.18 (a). This is well documented in the literature [89, 132]. The presence of periodic domains also produces satellites in the transverse scan of the substrate GaAs $(0\,0\,4)$ reflection as shown in Fig. 5.18 (b). Two orders of equally spaced satellites corresponding to the periodic elastic domains are observed and denoted by “S". The satellites are only observed when the incident beam is

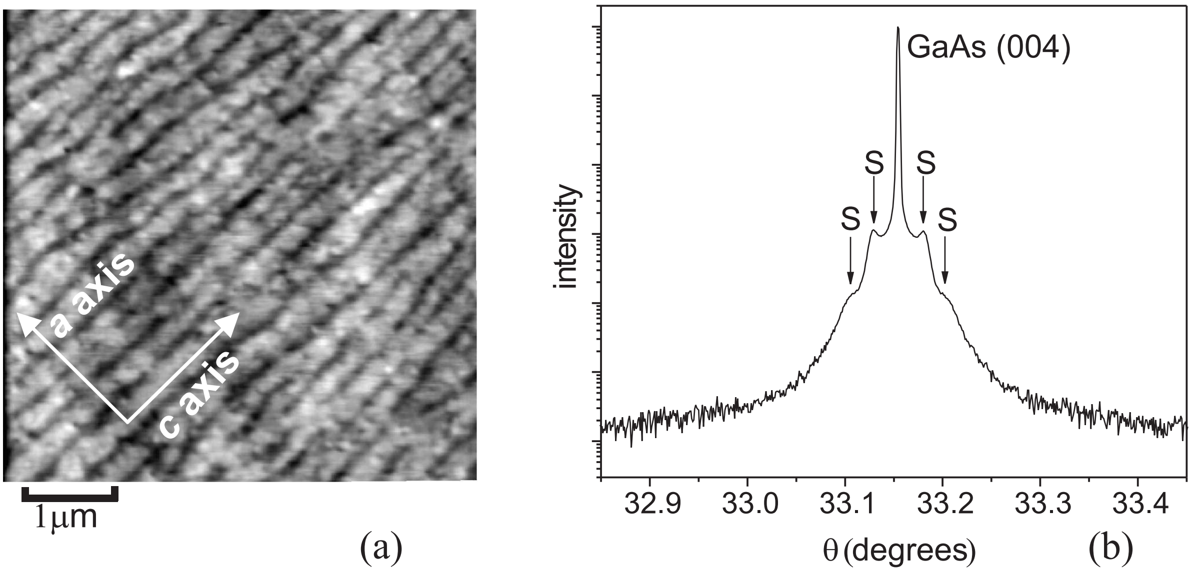

Figure 5.18: (a) Atomic force micrograph of a 51 nm thick MnAs film grown on GaAs (0 0 1). The α and β MnAs phases rearrange themselves to form stripe like patterns to minimize the elastic energy. The stripes run along the c axis. (b) Transverse x-ray scan of the GaAs (0 0 4) reflection. The incidence beam is perpendicular to the c axis. S denotes the satellites due to the periodic elastic domains of α and β MnAs.

perpendicular to the MnAs c axis. An azimuthal rotation of the sample by 90° results in the absence of the satellites (not shown). This proves that the satellites are generated by the periodic elastic domains. The lateral period of the domain structure (ψ) is determined from the spacing of the satellites using the formula $\psi = \lambda/(2\,\Delta\omega\,\sin\theta_B)$, where λ is the wavelength of x-rays, $\Delta\omega$ is the angular separation between the satellites and θ_B is the Bragg angle. The calculated value 305 ± 10 nm for the domain period, from the satellite spacing agrees well with the domain size measured from the AFM scans. The satellites are also seen in the transverse scans of the MnAs layer reflections [136].

5.5 Conclusions

In conclusion, depth-resolved grazing incidence diffraction reveals an ordered array of misfit dislocations at the MnAs/GaAs (0 0 1) interface. These dislocations are interfacial edge dislocations with dislocation lines along the MnAs [0 0 0 1] direction and the Burgers vector $\frac{1}{3}[1\,1\,\bar{2}\,0]$. The separation between the dislocations is 4.95±0.05 nm. The Burgers vector is equal to one lattice spacing along the MnAs $[1\,1\bar{2}\,0]$ direction and represents the shortest possible perfect-dislocation Burgers vector in the hexagonal system. The Burgers vector lies in the plane of the interface and hence is very efficient in strain relaxation by allowing lateral gliding of the misfit dislocations. The dislocations change their period according to the strain variation caused by the coexistence of the α and β phases of MnAs at room temperature. The intensity of the dislocation satellite along the CTR is measured and compared to model calculations. The inhomogeneous strain field of the misfit dislocation array is found to be confined at the interface within a thickness of 1.6 nm.

Grazing incidence diffraction was employed to investigate interface along the *c* axis, and we successfully resolved a small basic unit of non-integer plane matches as well as the large period of these basic units at the interface. The basic unit consists of 40/9 MnAs $(0\,0\,0\,2)$ spacings or 58/9 GaAs $(2\,\bar{2}\,0)$ spacings, so that the whole structure is repeated after 9 modulation periods. The MnAs film is very rigidly connected to the GaAs substrate along the *a* axis with the periodic misfit dislocations and very weakly (almost floating) bonded along the *c* axis.

During annealing, the crystal quality of the MnAs layer improves drastically and a 0.25% relaxation of the in-plane lattice parameter *a* is observed. We find an increase in the integrated intensity of the layer peak by a factor of 1.8, primarily due to the improved crystal quality. The mosaicity of the MnAs layer is reduced by almost 50%. The order of the dislocation array also improves due to annealing. The period of the dislocation network adjusts itself to the lattice parameter misfit at all temperatures investigated.

The strain-mediated coexistence of α and β MnAs phases is observed within a temperature interval of 20 °C. The two phases have the same lateral lattice spacing along the *a* axis at well above and below the phase transition temperature. The fraction of the low-temperature α MnAs phase is increasing almost linearly during cooling. The in-plane spacing of α MnAs increases abruptly at the phase transition temperature and then continues to decrease with the increasing phase fraction. In the coexistence regime the two phases form elastic domains in the form of stripes running along the *c* axis. The period of the elastic domains calculated from the x-ray diffraction and atomic force microscopy are in good agreement.

Chapter 6

Growth of MnAs on the GaAs (1 1 3)A surface

Most studies of semiconductor heterostructures are performed on (0 0 1) oriented substrates and other high symmetry substrates like (1 1 0) and (1 1 1). Nevertheless, studies of semiconductor heterostructures on lower symmetry substrate surfaces are well documented in the literature. The growth, as well as the structural, optical, and electronic properties of semiconductor heterostructures have been investigated both theoretically and experimentally for the (2 1 1) [137], (3 1 1) [138, 139], (5 1 1) [140], (2 2 1) [141] and (3 3 1) [142] surfaces. These studies show the dependence of many physical properties including surface reconstruction during growth, surface morphology, lattice deformation, incorporation of impurity atoms (dopants), bonding configuration and the sticking coefficient on the substrate orientation. In this chapter we will discuss the growth mechanisms, magnetic properties, and interface structure of MnAs films grown on GaAs (1 1 3) oriented substrates. Our main aim of using high-Miller-index GaAs (1 1 3) oriented substrates for the growth of MnAs is to study the effect of the starting templates on the growth mode, film orientation and the interface configuration. Depending on the termination, the GaAs surface is divided into two surfaces: GaAs (1 1 3)A and GaAs (1 1 3)B. From previous chapters, we know that an As-rich environment is favorable for MnAs growth on GaAs (0 0 1) substrates. Therefore, we choose the GaAs (1 1 3)A surface which is As terminated and contains threefold-coordinated Ga atoms and twofold-coordinated As atoms [143]. A model for the surface structure based on STM investigations was proposed by Wassermeier *et al.* [144]. The model proposes a (8×1) reconstruction of the surface with a lateral periodicity of 32 Å and a depth modulation of 3.4 Å. This model is also supported by a kinematical RHEED simulation study [145]. The GaAs (1 1 3)A surface is a non-polar surface compared to the (0 0 1) surface.

6.1 Nucleation and growth of MnAs on GaAs (1 1 3)A

The nucleation of MnAs is studied both by RHEED and *in situ* GID. A series of RHEED images with the electron beam parallel to GaAs $[1\,\bar{1}\,0]$ direction recorded during the nucleation of MnAs on GaAs (1 1 3)A substrate is shown in Fig. 6.1. The MnAs is grown at a substrate temperature of 250 °C and the growth rate is about 10 nm/hour. The GaAs surface has a 8×1 reconstruction at 260 °C which is stable over a large temperature

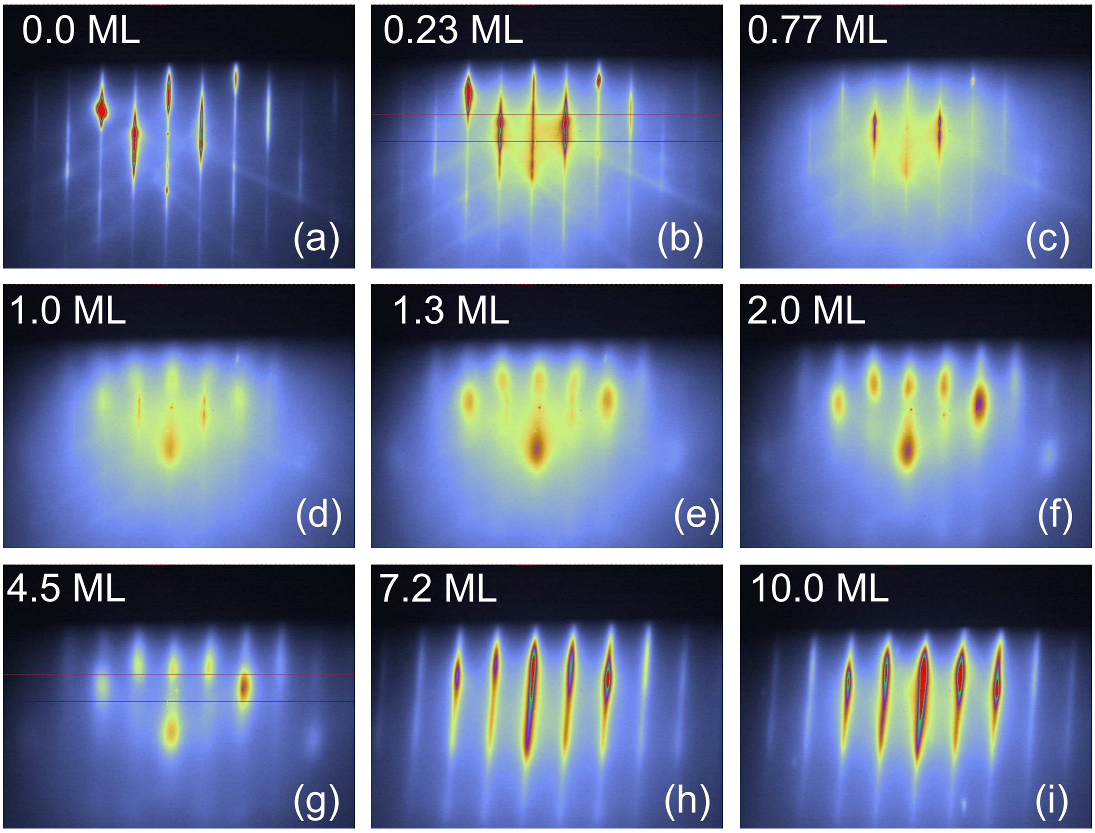

Figure 6.1: Static RHEED patterns recorded during the nucleation of MnAs on GaAs (1 1 3)A. The electron beam is parallel to the GaAs $[1\,\bar{1}\,0]$ direction.

range. The stability of the surface reconstruction over a wide temperature range simplifies the growth of MnAs. Figure 6.1 (a) shows the 1× RHEED pattern of GaAs (1 1 3)A just before starting the growth. The sharp distinct streaks and the presence of Kikuchi lines in the RHEED pattern give an indication of a well-ordered and smooth surface. Upon the deposition of MnAs no change in the RHEED pattern is visible until 0.77 ML [see Figs. 6.1 (b, c)], except for an increase in the background intensity. Since we have increased the electron beam current during growth, it is difficult to conclude that the increase in background intensity is due to the growth of MnAs. At 1 ML, the width of the streaks increases and the lattice spacing of MnAs appears. This confirms that stoichiometric MnAs already forms at a thickness of 1 ML. The lattice constant along the MnAs $[1\,1\,\bar{2}\,0]$ direction is calculated to be 3.61 ± 0.5 Å from Fig. 6.1 (d). Still a weak 1× RHEED pattern of GaAs is faintly visible, indicating that the whole surface is not yet covered with MnAs. This indicates the formation of islands on the surface. With increasing thickness, the intensity of the MnAs RHEED streaks increases and the GaAs streaks disappear. The spotty RHEED pattern shown in Figs. 6.1 (e-g) clearly indicates the formation of three-dimensional mounds on the surface. The RHEED pattern at a thickness of more than 7 ML [see Figs. 6.1 (h, i)] shows smooth streaks indicating the transition to a continuous smooth film . The tilt of the RHEED patterns in Figs. 6.1 (h, i) is related to the tilt of the unit cell and is discussed below.

The in-plane radial x-ray scans in grazing incidence geometry are performed by interrupting the growth of MnAs at different layer coverages and are shown in Fig. 6.2.

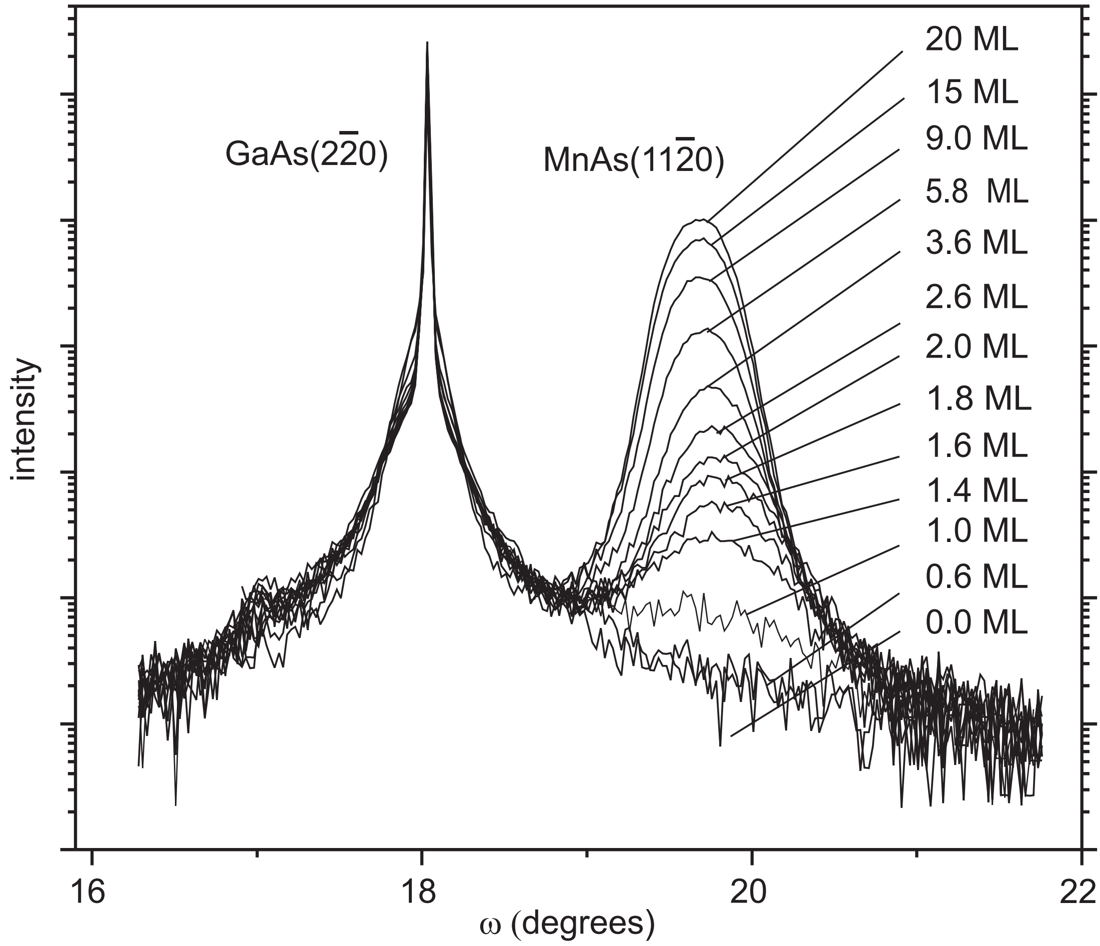

Figure 6.2: In-plane radial scans along the GaAs [1 $\bar{1}$ 0] direction during deposition of MnAs as a function of layer thickness. The scans were recorded at a grazing incidence angle of 0.25° with an x-ray energy of 10 keV. The number of monolayers deposited is indicated to the right of each scan.

The time required to take one scan is about 6 to 7 minutes. All scans were measured with a grazing incidence angle close to the critical angle for total external reflection, α_c, for MnAs. The GID measurements and RHEED patterns indicate that MnAs grows in a hexagon-on-cube epitaxy with the epitaxial relation MnAs [1 1 $\bar{2}$ 0] $\|$ GaAs [1 $\bar{1}$ 0] and $\sim$ MnAs [0 0 0 1] $\|$ GaAs [3 3 $\bar{2}$] [61]. The epitaxial match is shown schematically in Fig. 6.3. A 4° upward tilt of the unit cell along the MnAs [0 0 0 1] direction is measured by *ex situ* x-ray diffraction and from the tilt of the streaks in the static RHEED patterns shown in Figs. 6.1 (g, h).

The GaAs (2 $\bar{2}$ 0) peak is used as a reference to calculate the Bragg angle of the MnAs peak in each scan. A clear and separate MnAs peak appears at the high-angle side of the substrate peak already at a layer thickness of around 1 ML nominal coverage. This is consistent with the RHEED observations. It implies that almost relaxed MnAs islands are formed on the surface. Neither the appearance of the MnAs peak nor the change in the width of the substrate peak are seen until a coverage of about 1 ML.

The integrated intensity of the MnAs (1 1 $\bar{2}$ 0) peak as a function of layer thickness is shown in Fig. 6.4 (a). The integrated intensity, which is directly proportional to the amount of deposited material in kinematical theory, increases linearly with the layer

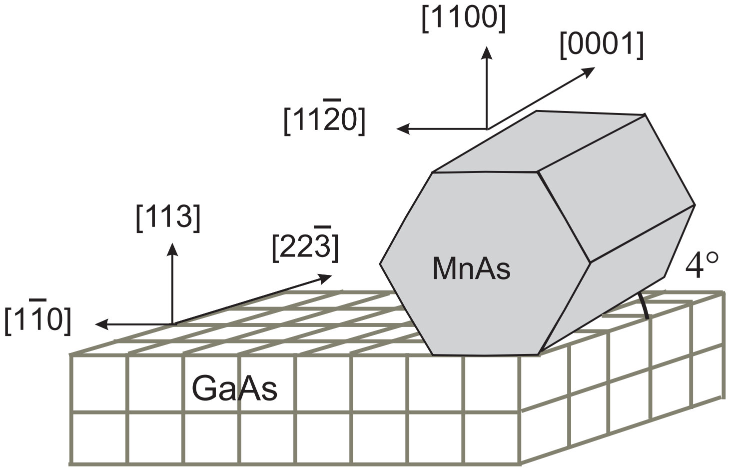

Figure 6.3: Scheme of epitaxy for MnAs/GaAs (1 1 3)A heterostructures. The unit cell is tilted along the [0001] direction by about 4°.

thickness. The slower increase after 20 ML can be attributed to the limited penetration depth of the x-rays. This indicates a constant growth rate. The MnAs peaks starting from 1.6 ML film thickness are well fitted by a Gaussian function, and the in-plane lattice parameter a is calculated from the peak position. The evolution of the in-plane lattice parameter as a function of thickness is shown in the Fig. 6.4 (b). The measured MnAs lattice spacing of 3.659 Å at 1.6 ML is smaller than its bulk value 3.701 Å [46] at 260°C. Hence, the MnAs lattice is not completely relaxed but compressively strained by 1.1 %. This is consistent with the RHEED observations during the nucleation phase. Upon further growth of MnAs, the lattice continues to relax. A net 0.6 % relaxation in the in-plane lattice spacing is seen at a layer thickness of 8 ML. The lattice spacing changes very little with further increases in layer thickness. Thus an almost relaxed layer of MnAs is formed at a thickness of 8 ML.

The full widths at half maximum (FWHM) of the peaks are obtained from the Gaussian fits to the MnAs $(1 1 \bar{2} 0)$ peak. The measured FWHM is corrected for instrumental resolution. Since we are measuring the first-order reflection with a small Bragg angle (18°), the contribution from strain in the layer to the broadening of the peak is relatively small. By using Scherrer's formula we estimate the in-plain grain size along the MnAs $[1 1 \bar{2} 0]$ direction from the FWHM of the MnAs peak as a function of layer thickness as shown in Fig. 6.4 (a). We see a clear two-stage increase in the in-plane lattice spacing and the grain size: a fast increase below 8 ML and a rather slow increase above 8 ML. The fast increase of the in-plane spacing is probably due to relaxation of MnAs islands by the introduction of misfit dislocations at the boundaries of the growing islands. The fast increase of the in-plane grain size in this model is due to lateral growth at the edges of the islands from deposition of more material during the early stage of growth. The slow increase after 8 ML can be attributed to the improvement of crystal quality and further ordering of the dislocations by coalescence of islands [146]. Finally, as the thickness increases, the islands form a continuous smooth film as indicated by the slower increase of the in-plane grain size.

No signature of the formation of a hexagonal structure is seen in RHEED patterns until 0.77 ML coverage [see Fig. 6.1 (c)]. We do not see the diffuse sphere of intensity

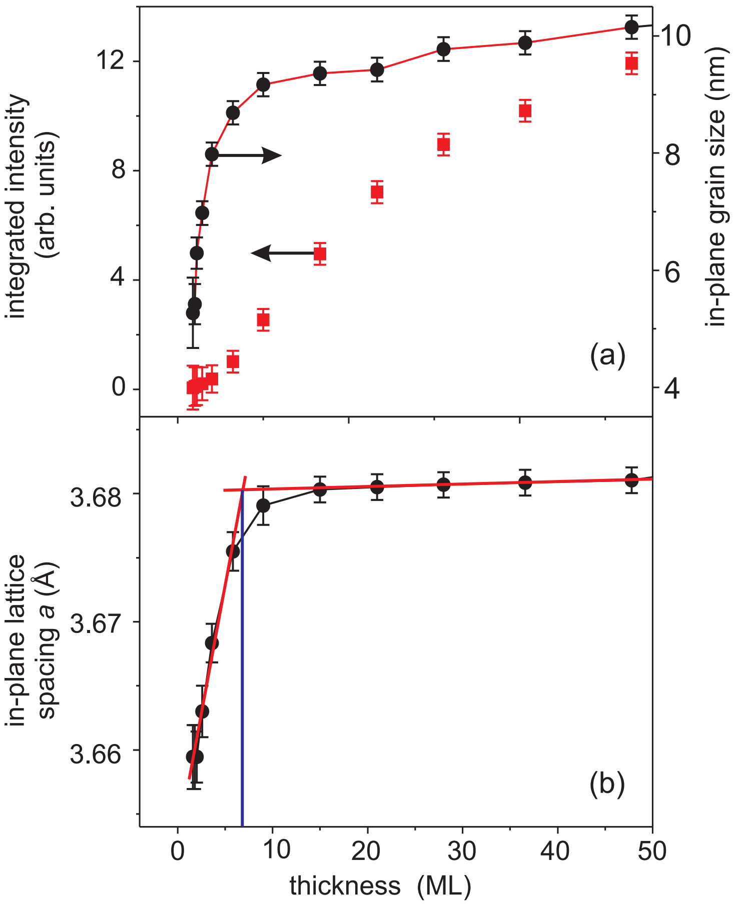

Figure 6.4: (a) Evolution of in-plane grain size (circles) along the a axis and increase of integrated intensity (squares) of the MnAs $(1\,1\,\bar{2}\,0)$ peak with layer thickness. (b) Evolution of the in-plane lattice spacing a during growth as a function of layer thickness. Straight lines are fits to the data. The vertical line passing through the intersection of the fits separates the region of fast increase of in-plane grain size and fast relaxation of in-plane lattice spacing from the region with slow increase. Error bars are indicated for each data point.

in reciprocal space corresponding to Mn-As bond length as in the GaAs (0 0 1) case (see chapter 3). The formation of MnAs with hexagonal structure is very abrupt and clearly seen at a thickness of 1 ML. It indicates that the misfit of 7.5 % along the a axis is already released by the formation of misfit dislocations. The misfit dislocations are introduced during the growth of the first monolayer directly at the interface. The appearance of the MnAs peak and the spotty RHEED pattern at 1 ML coverage rule out the formation of a wetting layer in the beginning of growth. This confirms the formation of three-dimensional relaxed MnAs islands. Therefore, the film is most likely growing in the Volmer-Weber growth mode. The overall behavior of MnAs growth on GaAs (1 1 3)A is similar to that on GaAs (0 0 1), except that the formation of three-dimensional islands with a hexagonal symmetry occurs at a lower thickness of about 1 ML.

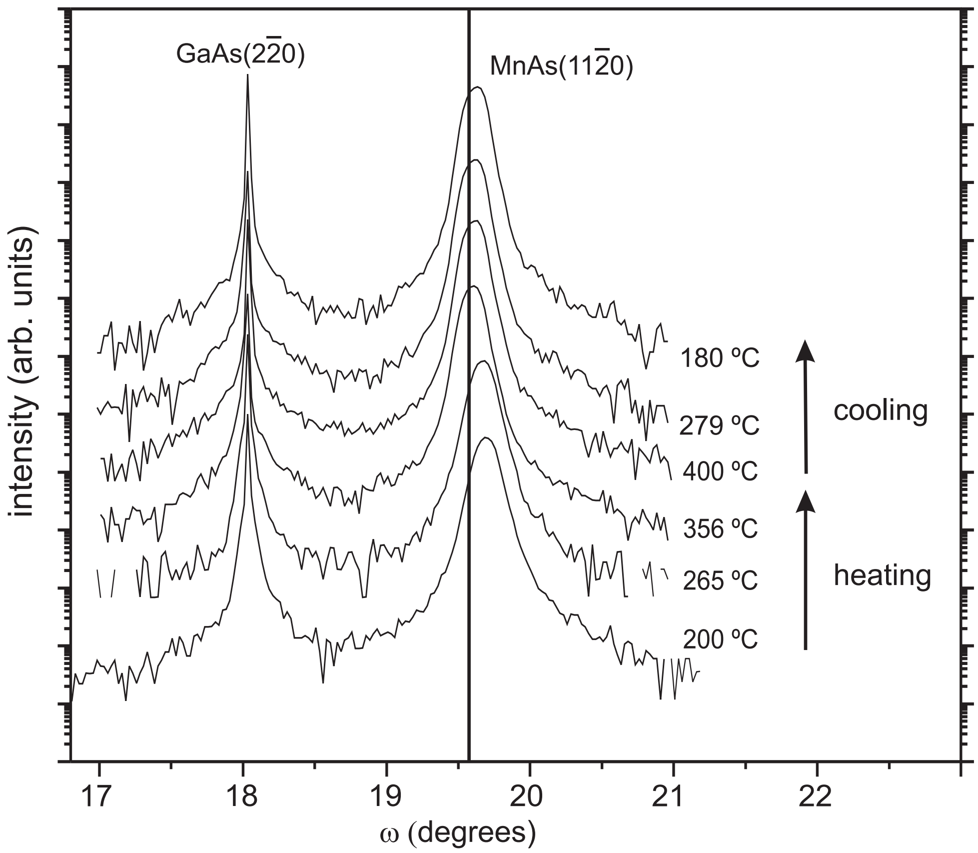

Figure 6.5: Radial scans along the MnAs [1 1 $\bar{2}$ 0] direction during *in situ* postgrowth annealing. The scans were recorded at a grazing incidence angle of 0.3 °. The temperature at which the measurement was performed is given on the right hand side. The GaAs (2 $\bar{2}$ 0) substrate peak is also recorded in each curve. The vertical line represents the position of the MnAs (1 1 $\bar{2}$ 0) reflection for the fully relaxed material at 180°C. For clarity, the curves are shifted in the vertical direction.

6.2 In situ post growth thermal annealing

Post-growth *in situ* thermal annealing was carried out in the MBE growth chamber while exposing the MnAs surface to the As_4 flux to prevent As desorption from the surface. The sample was not cooled down to room temperature after growth at 250 °C. Annealing was performed at a temperature of 400 °C for 10 minutes with a heating and cooling rate of 15 °C min^{-1}. The layer structure and morphology during annealing was monitored by recording RHEED patterns as well as GID profiles along the MnAs [1 1 $\bar{2}$ 0] direction. The radial scans recorded in grazing incidence geometry during the annealing are shown in Fig. 6.5. The measured curves are normalized to the substrate intensities. The vertical line in the figure marks the position that would be expected for bulk MnAs (1 1 $\bar{2}$ 0) at 180 °C [46].

A net increase of 0.35 % in the in-plane lattice spacing along the MnAs *a* axis occurs during annealing as shown in Fig. 6.6 (a). This is partly due to the relaxation of the in-plane strain by the ordering of misfit dislocations present at the interface (to be discussed below), and partly due to thermal expansion. The slight decrease in the in-plane lattice spacing during cooling is attributed to the thermal contraction of the layer. We find a 7 % increase of the in-plane grain size during heating as shown in Fig. 6.6 (b). The grain size

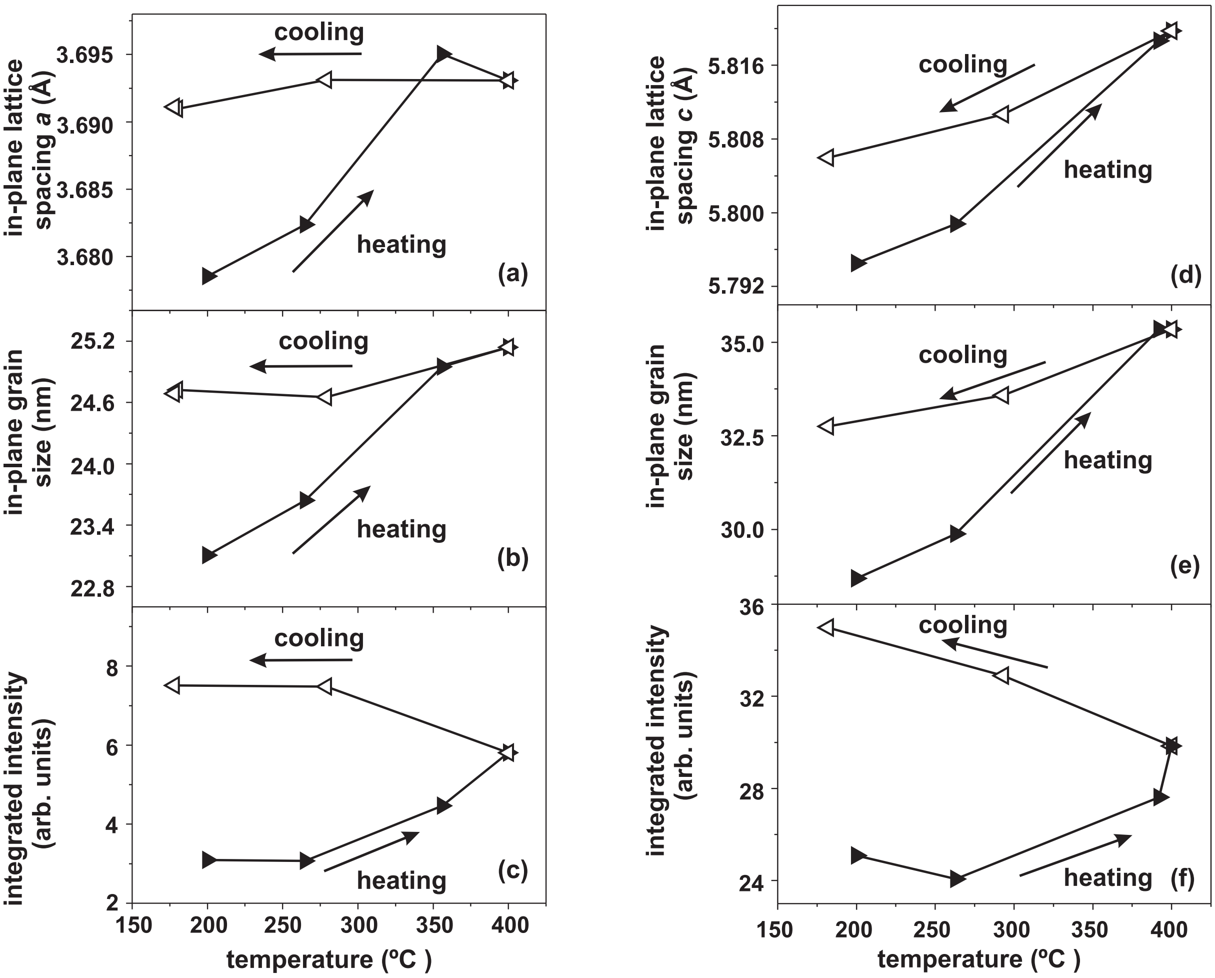

Figure 6.6: The evolution of in-plane lattice spacing, in-plane grain size and integrated intensity along the *a* axis (a, b, c) and *c* axis (d, e, f) during *in situ* postgrowth thermal annealing as a function of annealing temperature. The arrows indicate the direction of heating to 400 °C and cooling to 180 °C. The filled triangles represent the measurement during heating and the unfilled triangles represent the measurement during cooling.

reaches a final value of about 25 nm after annealing. This confirms the improvement of the crystal quality and homogeneity of the layer during annealing, which is probably due to the elimination of defects present at the grain boundaries and the coalescence of smaller islands into larger ones. The integrated intensity of the MnAs $(1 1 \bar{2} 0)$ peak increases by a factor of 2 as shown in Fig. 6.6 (c). According to kinematical theory, the integrated intensity should remain the same as long as a wide enough angular interval around the peak is considered. A deviation from this rule can be explained by the rearrangement of atoms, for example at the domain boundaries, from non-lattice or strongly disordered positions to film lattice positions. In this way, their scattered intensity is included in the peak after the annealing whereas before, it contributes to the background outside the measured interval. A significant increase of the intensity of the specular spot in the RHEED pattern during annealing was also reported for MnAs on GaAs (0 0 1) [147], which supports this conclusion also for the near-surface region. The increase of the integrated intensity during cooling is also seen in Fig. 6.6 (c). This may be due to the incomplete relaxation during the 10 minute anneal of the sample. Hence the relaxation process

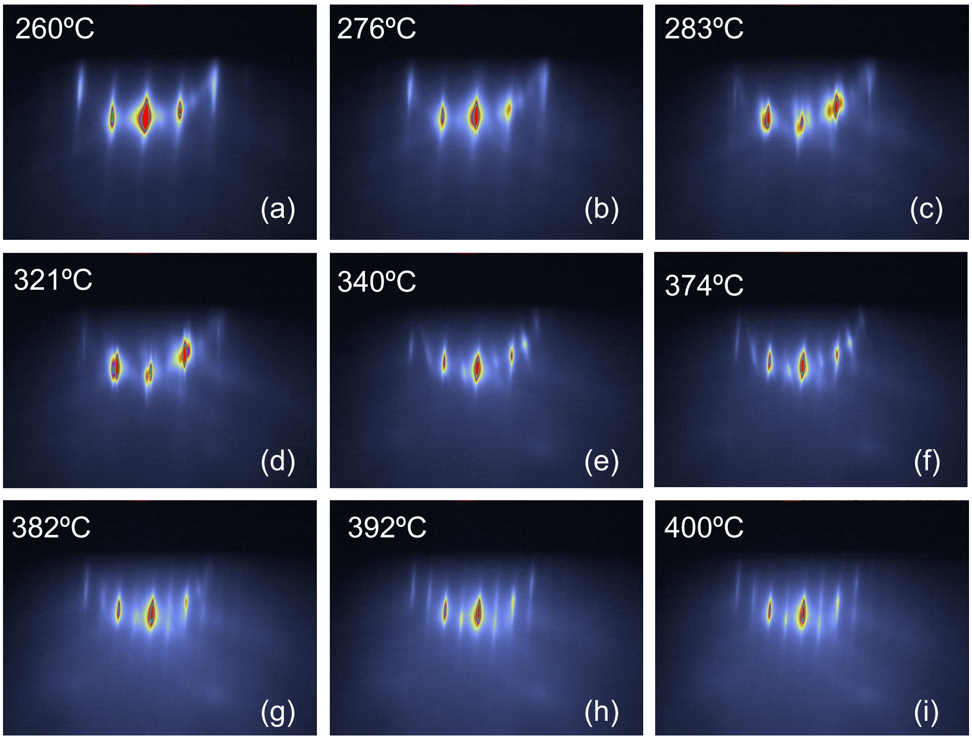

Figure 6.7: RHEED patterns recorded during heating of the sample to 400 °C. The electron beam is directed parallel to the GaAs $[1\,\bar{1}\,0]$.

continues during cooling.

We also studied the effect of the annealing on the structure along the *c* axis by measuring the MnAs $(0\,0\,0\,4)$ reflection on an identical sample grown under the same conditions as before as shown in Fig. 6.6 (d, e, f). The in-plane lattice parameter *c* increases by 0.2 %. A 12 % increase of in-plane grain size along the *c* axis is measured. We see a decrease in the in-plane grain size during cooling. The strain state of the film changes during cooling due to thermal contraction. This may be responsible for the decrease of the in-plane grain size. The enhancement of the integrated intensity and the reduction of the FWHM of the MnAs peak in both the *a* and *c* axis demonstrate a significant improvement of the surface morphology and crystal quality of the film.

6.2.1 Facet formation during annealing

The microscopic details of the change in the surface structure during annealing studied by RHEED are shown in Fig. 6.7. The figure displays a series of RHEED patterns recorded at different temperatures during the heating. The electron beam is directed parallel to the GaAs $[1\,\bar{1}\,0]$. Figure 6.7 (a) shows the previously discussed tilted RHEED pattern. The streaks are titled by 4°, therefore following the tilt of the unit cell. In that sense, the surface can be thought of as a vicinal surface.

We see a change in surface reconstruction at 400 °C during annealing. The MnAs surface shows a 2×1 reconstruction with 1× periodicity along the GaAs $[1\,\bar{1}\,0]$ direction [see Fig. 6.7 (a)] at 260 °C and 2× periodicity at 400 °C [Fig. 6.7 (i)]. The transition from 1× to 2× occurs through the formation of facets in the temperature range from

320 °C to 375 °C. The observation of additional tilted streaks between the 1× streaks in the RHEED patterns are shown in Figs. 6.7 (e, f). This confirms the formation of facets. These streaks are tilted by about 18° with respect to the 1× MnAs streaks. The facets are again absent at 400 °C and the surface becomes smooth. The process is reversible as seen from the RHEED pattern during the cooling (not shown) with a hysteresis of about 10 °C in temperature. The detailed mechanism of mass transport and formation of the facets is difficult to resolve only from RHEED observations and the reversibility of the process makes it even more complicated.

6.3 Interface structure

The misfit along the MnAs $[1\,1\,\bar{2}\,0]$ is the same for MnAs/GaAs (1 1 3)A as for the MnAs/GaAs (0 0 1) heterostructures. Therefore, the same interface configuration with a periodic array of misfit dislocations may be expected for this system. We again explored the interfacial configuration along the MnAs $[1\,1\,\bar{2}\,0]$ by depth-tunable GID. The GID profiles of the first-order and second-order reflections are shown in Fig. 6.8. The incidence angle is specified at the right of each curve. We observe satellites at both reflections. They appear when the incidence angle exceeds the critical angle, which confirms that they originate from the interface. A radial scan of the first-order reflection along the MnAs $[1\,1\,\bar{2}\,0]$ direction does not show any satellites between the main peaks. However, a weak satellite peak S_{-1} is visible at an incidence angle of 0.6° [see Fig. 6.8 (a)]. The distance between the satellite and the substrate peaks is equal to the separation of the main peaks. In the second-order measurements shown in Fig. 6.8 (b), we see only one satellite between the main peaks. This is in contrast to the MnAs/GaAs (0 0 1) case where three satellites are present [see Fig. 5.5 (b)]. The splitting of substrate, layer, and satellite peaks is again due to the coexistence of the α and β phases of MnAs as discussed in the previous section.

The presence of the satellite reflections confirms that the misfit at the MnAs/GaAs (1 1 3)A interface is again released by a regular array of misfit dislocations. The period of the satellites, which is two times larger compared to the MnAs/GaAs (0 0 1) case, gives half the spacing between the periodic misfit dislocations, $\Lambda = 2.45 \pm 0.05$ nm. The release of the same misfit by twice the number of dislocations implies a Burgers vector that is half as long. This means that the in-plane component of the Burgers vector at the MnAs/GaAs (1 1 3)A interface is $\frac{1}{6}[1\,1\,\bar{2}\,0]$, which is in agreement with Eq. (5.2). Referring to the GaAs lattice, the same Burgers vector is given by $\frac{1}{2}[1\,\bar{1}\,0]$, which is the smallest Burgers vector in the zincblende crystal structure [130].

The interfacial configuration along the MnAs [0 0 0 1] direction is completely different from the one of the MnAs/GaAs (0 0 1) heterostructures. The entire misfit along this interface is released by the 4° tilt of the layer. The 4° tilt from the singular MnAs $[1\,\bar{1}\,0\,0]$ growth direction, in the case of the MnAs/GaAs (1 1 3)A films, promotes the generation of a coherent interface, by improving the alignment of the $\{1\,\bar{1}\,0\,0\}$ lattice planes in MnAs with the $\{1\,1\,1\}$ lattice planes in GaAs. This is confirmed by the cross sectional high-resolution transmission electron microscopy (HRTEM) measurements [61].

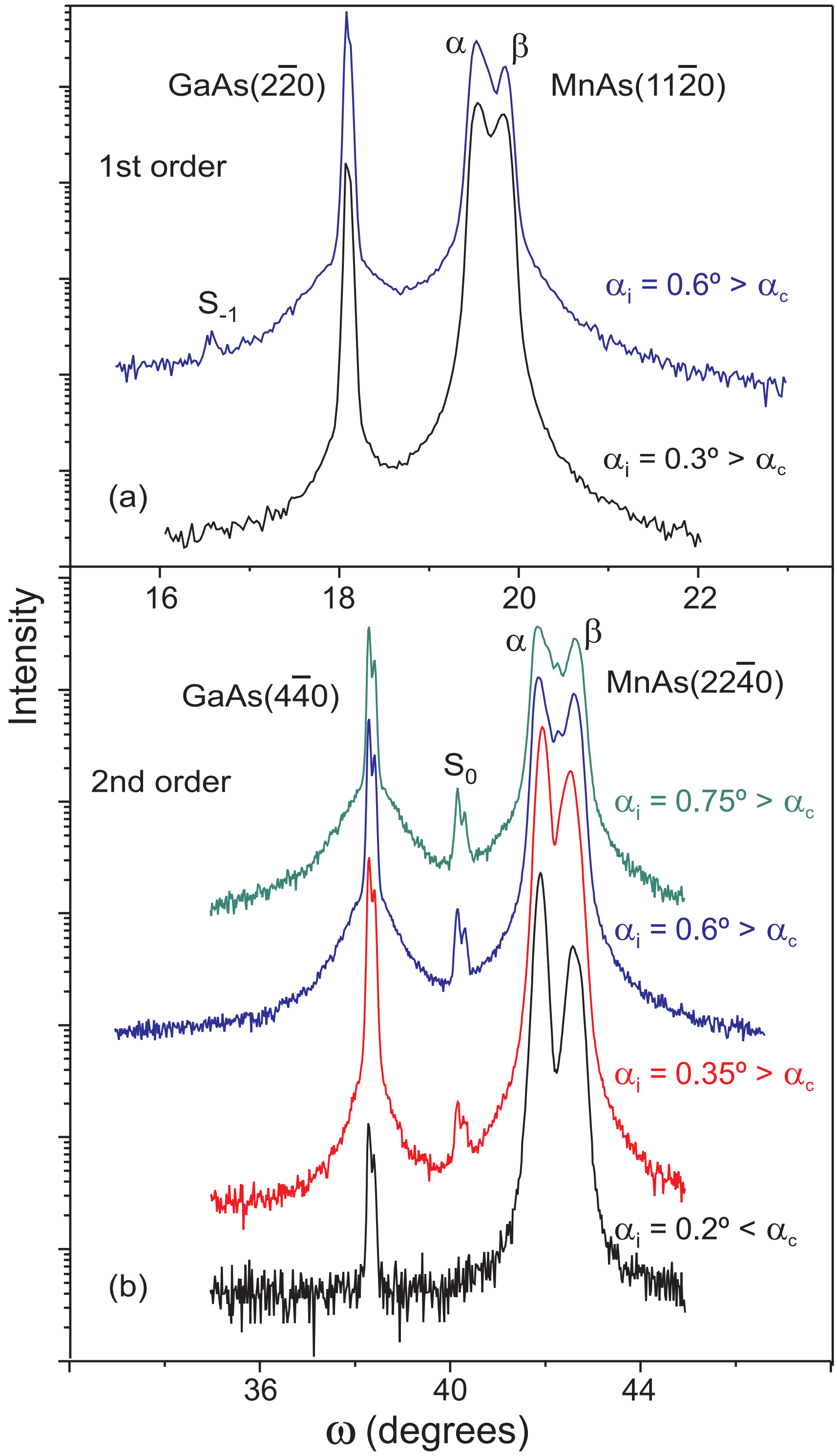

Figure 6.8: Radial scans recorded along the a axis of the MnAs/GaAs (1 1 3)A interface for different grazing incidence angles α_i. (a) First- and (b) second-order reflection. The S$_i$ indicate the satellites originating from the periodic array of misfit dislocations. The scans are recorded at room temperature. Peaks labelled α and β refer to the different phases of MnAs. The profiles are shifted vertically for clarity. X-ray energy is 10 keV.

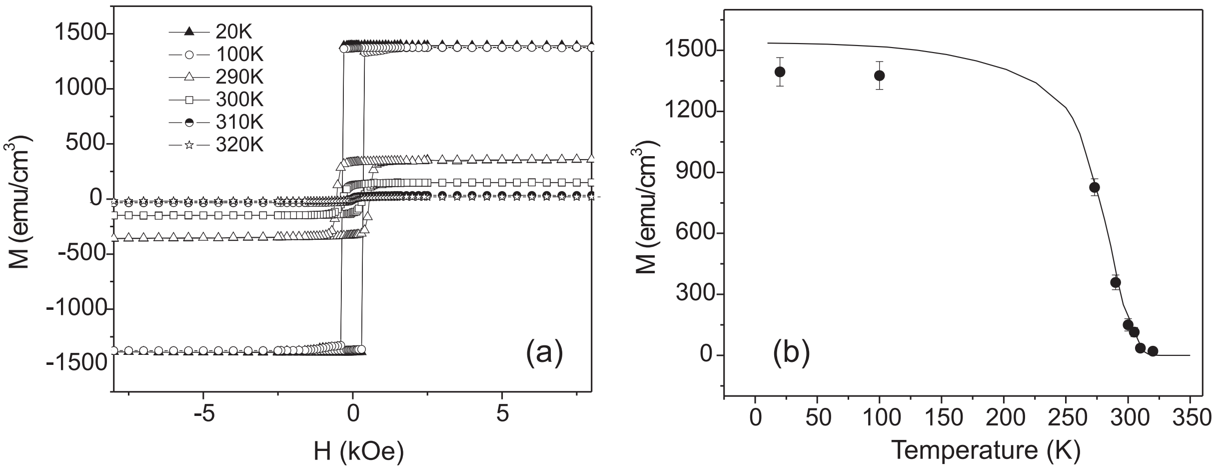

Figure 6.9: (a) Magnetization loops of the MnAs/GaAs (1 1 3)A heterostructure. The field is applied along the MnAs *a* axis. The data are corrected for the diamagnetic signal due to the substrate. (b) Magnetization as a function of temperature. The filled circles show the saturation magnetization measured from the hysteresis loop along with the corresponding error bars.

6.4 Magnetic Properties of MnAs/GaAs (1 1 3)A heterostructures

All measurements were performed on a MnAs sample of about 20 nm thickness with the external field applied along the MnAs *a* axis, which is the easy axis of magnetization [61]. The hysteresis loops were measured at different temperatures starting from 20-320 K and the data is presented in Fig. 6.9 (a). At first glance we notice that the saturation magnetization (M_{sat}) decreases with an increase in temperature. The reduction of M_{sat} reflects the decrease of the relative volume of the film on the ferromagnetic α MnAs phase at higher temperatures. M_{sat} could therefore be used as a magnetic probe of the α phase fraction. We note, however, that the magnetization value also includes a weak intrinsic temperature dependence due to thermal fluctuation effects. Furthermore, using M_{sat} as a magnetic probe of the α phase fraction mixes up two distinct effects: the temperature dependence of the fraction of α MnAs and the field-induced phase transition effect, since a variable magnetic field is required to obtain saturation as the film temperature is varied [134]. An abrupt square hysteresis loop is observed for low temperature measurements (at 20 and 100 K). But in the phase coexistence regime between 283 K and 315 K the abruptness disappears and a rounded shape is observed. This is probably due to the appearance of paramagnetic β MnAs stripes in the film and the resulting increase in the surface roughness [132]. With increasing β MnAs content, the separation between the ferromagnetic α MnAs stripes increases, and therefore the coupling between them reduces [61]. This may also be responsible for the change in the shape of the hysteresis loops. The measurements revealed that the MnAs *c* axis is the hard axis of magnetization.

The Curie temperature determined from the measurement of the magnetization as a function of temperature is shown in Fig. 6.9 (b). The points indicate the saturation magnetization value determined from the hysteresis loops at different temperatures. Both data sets show a reasonable agreement. The magnetization falls to zero at a temperature of around 320 K, similar to what is observed for MnAs films grown on GaAs (0 0 1). Although the interface structure and epitaxial relationships are different, the magnetic properties of the film appears to be very similar to the MnAs/GaAs (0 0 1) heterostructure.

6.5 Conclusions

We have successfully grown and analyzed the strain relaxation of MnAs films on GaAs (1 1 3)A. The MnAs layers grow via the formation of ∼ 1 ML thick islands. The MnAs lattice is about 1% compressed at the beginning of the growth and relaxes upon further growth. Finally, the islands coalesce and form a continuous smooth film. The in-plane grain size improves in two stages during growth. A fast increase before coalescence is due to the relaxation and growth near the edge of the islands. The slower increase after coalescence is attributed to the improvement of the crystal quality with increasing thickness. The post-growth thermal annealing results in a further relaxation of the layer. It also improves the in-plane grain size by 7% along the a axis. After annealing, an almost relaxed MnAs layer is formed. A change in surface reconstruction mediated by the formation of facets is also observed during annealing. We observe an ordered array of misfit dislocations at the interface along the MnAs $[1\,1\,\bar{2}\,0]$ direction with a period of 2.45±0.05 nm. Compared to MnAs/GaAs (0 0 1) heterostructures, the dislocation density is doubled when growing MnAs on GaAs (1 1 3)A surface. Despite the different interface structure and orientation of the MnAs/GaAs (1 1 3)A and MnAs/GaAs (0 0 1) heterostructures, they both show very similar magnetic properties.

Chapter 7

Summary

An *in situ* real-time study of nucleation, growth, microstructure and interface configuration of ferromagnetic MnAs films deposited on the semiconductor GaAs has been reported in this thesis. Scattering probes (GID and RHEED) are used to study the above mentioned phenomena. Owing to their high intensity, synchrotron x-rays are used to study the growth starting from the first monolayer. MnAs films are successfully grown on GaAs (0 0 1) and (1 1 3) A orientated surfaces by molecular-beam epitaxy.

The nucleation of hexagonal MnAs on the cubic semiconductor GaAs (0 0 1) surface is studied by RHEED azimuthal scans. This reveals four stages of the nucleation process of MnAs films. Below a coverage of 0.3 ML, a coherent adsorption or binding of the Mn adatoms to the GaAs substrate occurs. Randomly oriented structures with nearest neighbor distances of Mn-As form at coverages between 0.3 and 0.7 ML. In RHEED azimuthal scans, this appears as a ring of diffuse intensity. A dramatic improvement of the diffuse background intensity is seen at 0.8 ML. This is because of the increase in the random arrangement of the MnAs adunits that neither assume the structure of the substrate nor that of a MnAs film. The preferential arrangement of the MnAs adunits occurs due to the influence of the substrate at a thickness of about 1.8 ML. The epitaxial lock-in is established in two stages. First along the [1 1 0] direction, in which there is a strong interaction between film and substrate, then finally in the orthogonal $[1\,\bar{1}\,0]$ direction at a nominal coverage of 2 ML.

The evolution of strain in the layer beyond 2 ML thickness is studied by x-ray diffraction. MnAs film almost completely relaxes by the introduction of misfit dislocations directly at the interface during the growth. The misfit dislocations arrange themselves in an extremely periodic manner at a thickness of about 6 ML. This occurs even before the complete coalescence of the film. The remaining strain ($\leq 1\%$) is gradually released with increasing layer thickness. A compressive or tensile strain in the MnAs layer is found depending upon the growth rate. The observation of strain relaxation as a function of time reveals that the process is thermally activated. The MnAs growth has characteristics of both Stranski-Krastanov mode (coherent binding of Mn adunits below 0.3 ML) and Volmer-Weber mode (formation of three-dimensional islands above 2 ML that coalesces to form a continuous film). Therefore, although the STM investigations indicate Volmer-Weber nucleation and x-ray diffraction in later stages is consistent with this, the growth cannot be classified strictly into one of these two categories. The island size increases at a high rate up to 20 ML before coalescence, and more slowly afterwards. The average grain sizes reach a maximum value of about 32 nm along *c* axis and 27 nm along *a* axis at a layer thickness of about 160 ML. Therefore, the film contains many grain boundaries and related defects.

The microstructure of relaxed MnAs islands is studied by x-ray line profile analysis. The contributions of the finite size of the islands and the strain in these islands to the diffraction peak width are separated by a Willamson-Hall analysis. A nonuniform strain amounting to 0.66% along the c axis and 0.54% along the a axis is found . The twist of the MnAs islands about the surface normal decreases exponentially with increasing thickness. A high correlation of the defects along the a axis is determined from the calculation of the correlation parameters along the two orthogonal in-plane directions.

The interface is studied by depth-tunable grazing incidence diffraction. Equally spaced satellite reflections of both layer and substrate peak are observed in the x-ray diffraction profiles measured along the a axis. This confirms the formation of extremely periodic (highly correlated) array of misfit dislocations with a spacing of 4.95±0.05 nm along the a axis. The dislocation lines are along the c axis. The Burgers vector of these dislocations, $\frac{1}{3}[1\,1\,\bar{2}\,0]$, lies in the interfacial plane and is equal to one lattice spacing along the MnAs $[1\,1\,\bar{2}\,0]$. The inhomogeneous strain due to the dislocation array is confined to a thickness of about 1.6 nm at the interface. Along the c axis, the misfit is released by a coincidence site lattice without the discontinuities in the atomic spacing. We resolve the basic periodicity of the coincidence site lattice with a non-integer plane match of 4.4 MnAs planes to 6.4 GaAs planes. In addition to this, a superperiod of 9 basic units exists at the interface. The MnAs film is rigidly connected to the substrate along the a axis and only weakly bonded to the substrate along the c axis. An annealing of the film releases the residual strain in the layer and improves the ordering of the dislocation array as well as reduces the twist of the MnAs islands. We have observed an phase coexistence between hexagonal α MnAs and orthorhombic β MnAs phases of MnAs/GaAs(001) heteroepitaxial films. The fraction of the low-temperature phase α MnAs linearly increases upon cooling below the bulk phase transition temperature of 40 °C. The mean in-plane lattice spacing of both α and β MnAs phases is constant in the phase coexistence regime.

The growth of MnAs on the GaAs (1 1 3)A substrate proceeds through the formation three-dimensional islands at about 1 ML coverage. The islands are 1.1% compressively strained at a coverage of about 1.6 ML and relaxes upon further growth. Finally, the islands coalesce and form a continuous smooth film. The in-plane grain size improves in two stages, first a fast increase due to growth near the edge of the islands before coalescence, and a slower increase afterwards due to the improvement of the crystal quality with increasing thickness. The c axis of the unit cell is tilted by 4° along the growth direction. On MnAs/GaAs (1 1 3)A, the same mismatch (7.5%) along the a axis is released again by periodic misfit dislocations, but with a twice smaller Burgers vector and twice smaller spacing, compared to MnAs/GaAs (0 0 1). An *in situ* post-growth thermal annealing again shows a positive impact on the crystal quality and on the ordering of dislocations. The in-plane grain size increases by 7% and 12% along the a and c axis, respectively. A strong reversible faceting of the film is seen during the annealing.

Bibliography

[1] G. A. Prinz. *Science*, 250:1092, 1990.

[2] S. Datta and B. Das. *Appl. Phys. Lett*, 56:665, 1990.

[3] G. A. Prinz. *Science*, 282:1660, 1998.

[4] S.A. Wolf, D.D. Awschalom, R.A. Buhrman, J.M. Daughton, S. von Molnar, M.L. Roukes, A.Y. Chtchelkanova, and D.M. Treger. *Science*, 294:1488, 2001.

[5] M. Ramsteiner, H. Y. Hao, A. Kawaharazuka, H. J. Zhu, M. Kästner, R. Hey, L. Däweritz, H. T. Grahn, and K. H. Ploog. *Phys. Rev. B*, 66:081304, 2002.

[6] S. H. Chun, S. J. Potashnik, K. C. Ku, P. Schiffer, and N. Samarth. *Phys. Rev. B*, 66:100408, 2002.

[7] I. Žutić, J. Fabian, and S. Das Sarma. *Rev. Mod. Phys.*, 76:323, 2004.

[8] M. Tanaka, J. P. Harbison, T. Sands, T. L. Cheeks, V. G. Keramidas, and G. M. Rothberg. *J. Vac. Sci. Technol. B*, 12:1091, 1994.

[9] Masaaki Tanaka. *Semicond. Sci. Technol.*, 17:327, 2002.

[10] John M. Cowley. *Diffraction Physics.* North-Holland Publishing Company, Amsterdam, 1981.

[11] B. E. Warren. *X-Ray Diffraction.* Dover, New York, 1990.

[12] I. K. Robinson and D. J. Tweet. *Rep. Prog. Phys.*, 55:599, 1992.

[13] I. K. Robinson. *Phys. Rev. B*, 33:3830, 1986.

[14] S R Andrews and R A Cowley. *J. Phys. C: Solid State Phys.*, 18:6427, 1985.

[15] R. Feidenhans'l. *Surf. Sci. Rep.*, 10:105, 1989.

[16] R. Renaud. *Surf. Sci. Rep.*, 32:1, 1998.

[17] H. Dosch, B. W. Batterman, and D. C. Wack. *Phys. Rev. Lett.*, 56:1144, 1986.

[18] U. Pietsch. *Curr. Sci.*, 78:1484, 2000.

[19] J. D. Jackson. *Classical Electrodynamics.* John Wiley & Sons, New York, 1975.

[20] `http://doc.cern.ch/tmp/convert_p409.pdf`.

[21] G. Margaritondo. *J. Synchrotron Rad.*, 2:148, 1995.

[22] P. Duke. *Introduction to Synchrotron Radiation: Production and Properties.* Oxford University Press, UK, 2000.

[23] H. Sahito and Y. Gohshi, editors. *Applications of Synchrotron Radiation to Materials Analysis.* Elsevier Publication, Amsterdam, 1996.

[24] Bernd Jenichen, Wolfgang Braun, Vladimir M. Kaganer, Alexander G. Shtukenberg, Lutz Däweritz, Carl-Günther Schulz, Klaus H. Ploog, and Alexei Erko. *Rev. Sci. Instrum.*, 74:1267, 2003.

[25] E. Vlieg. *J. Appl. Cryst.*, 30:532, 1997.

[26] A. Cho. *J. Vac. Sci. Technol.*, 8:31, 1971.

[27] A. Cho and J. Arthur. *Prog. Solid-State Chem.*, 10:157, 1975.

[28] M. A. Herman and H. Sitter. *Molecular Beam Epitaxy, Fundamentals and Current Status*, volume 7 of *Springer Series in Material Science.* Springer, Berlin, 1989.

[29] K. H. Ploog. *Annu. Rev. Mater. Sci.*, 11:171, 1981.

[30] Ayahiko Ichimiya and Philip I. Cohen. *Reflection High-Energy Electron Diffraction.* Cambridge University Press, UK, 2004.

[31] Wolfgang Braun. *Applied RHEED*, volume 154 of *Springer Tracts in Modern Physics.* Springer, Berlin, 1999.

[32] Safire, by vts createc/fhg erlangen.

[33] B. A. Joyce, J. H. Neave, P. J. Dobson, and P. K. Larsen. *Phy. Rev. B*, 29:814, 1984.

[34] P. I. Cohen, P. R. Pukite, J. M. Van Hove, and C. S. Lent. *J. Vac. Sci. Technol. A*, 4:1251, 1986.

[35] J. M. Van Hove, P. Pukite, P. I. Cohen, and C. S. Lent. *J. Vac. Sci. Technol. A*, 1: 609, 1983.

[36] C. S. Lent and P. I. Cohen. *Phys. Rev. B*, 33:8329, 1986.

[37] E. Bauer. *Z. Kristallogr.*, 110:372, 1958.

[38] J. W. Matthews, Edited by J. W. Matthews. *Epitaxial Growth.* Academic, New York, 1975.

[39] Y.-W. Mo, D. E. Savage, B. S. Swartzentruber, and M. G. Lagally. *Phys. Rev. Lett.*, 65:1020, 1990.

[40] C. W. Synder, B. G. Orr, D. Kessler, and L. M. Sander. *Phys. Rev. Lett.*, 66:3032, 1991.

[41] John. A. Venables. *Introduction to Surface and Thin Film Processes.* Cambridge University Press, UK, 2000.

[42] J. Clarke. *Scientific American*, 271:46, 1994.

[43] `http://www.qdusa.com/products/mpms.html`.

[44] F. Heusler. *Z. Angew. Chem.*, 17:260, 1904.

[46] B. T. M. Willis and H. P. Rooksby. *Proc. Phys. Soc. London. Sect. B*, 67:290, 1954.

[45] R. H. Wilson and J. S. Kasper. *Acta Crystallogr.*, 17:95, 1964.

[47] H. Okamoto. In T. B. Massalski, H. Okamoto, P. R. Subramanian, and L. Kacpkzak, editors, *Binary Alloy Phase Diagrams*, volume 1, page 293, Metals Park, OH, 1990. American Society of Metals.

[48] S. Hilpert and T. Dieckmann. *Ber. Dtsch. Chem. Ges. A*, 44:2378, 1911.

[49] A. Serres. *J. Phys. Radium*, 8:146, 1947.

[50] C. Guillaud. *J. Phys. Radium*, 12:223, 1951.

[51] C.P. Bean and D. S. Rodbell. *Phys. Rev.*, 126:104, 1962.

[52] R. W. de Blois and D. S. Rodbell. *Phys. Rev.*, 130:1347, 1963.

[53] N. Menyuk, J. A. Kafalas, K. Dwight, and J. B. Goodenough. *Phys. Rev.*, 177:942, 1969.

[54] S. Haneda, N. Kazama, Y. Yamaguchi, and H. Watanabe. *J. Phys. Soc. Jpn.*, 42: 1201, 1977.

[55] A. K. Das, C. Pampuch, A. Ney, T. Hesjedal, L. Däweritz, R. Koch, and K. H. Ploog. *Phys. Rev. B*, 69:081306, 2004. and references therein.

[56] M. Tanaka, J. P. Harbison, M. C. Park, Y. S. Park, T. Shin, and G. M. Rothberg. *Appl. Phys. Lett.*, 65:1964, 1994.

[57] M. Tanaka, J. P. Harbison, M. C. Park, Y. S. Park, T. Shin, and G. M. Rothberg. *J. Appl. Phys.*, 76:6278, 1994.

[58] F. Schippan, A. Trampert, L. Däweritz, and K. H. Ploog. *J. Vac. Sci. Technol. B*, 17:1716, 1999.

[59] L. Däweritz, F. Schippan, A. Trampert, M. Kästner, G. Behme, Z.M. Wang, M. Moreno, P. Schützendübe, and K. H. Ploog. *J. Cryst. Growth*, 227–228:834, 2001.

[60] M. Kästner, L. Däweritz, and K.H. Ploog. *Surf. Sci.*, 511:323, 2002.

[61] L. Däweritz, L. Wan, B. Jenichen, C. Herman, J. Mohanty, A. Trampert, and K. H. Ploog. *J. Appl. Phys.*, 96:5056, 2004.

[62] D. Kolovos-Vellianitis, C. Herrmann, L. Däweritz, and K. H. Ploog. *Appl. Phys. Lett.*, 87:092505, 2005.

[63] K. Akeura, M. Tanaka, M. Ueki, and T. Nishinaga. *Appl. Phys. Lett.*, 67:3349, 1995.

[64] F. Schippan, M. Kästner, L. Däweritz, and K. H. Ploog. *Appl. Phys. Lett.*, 76:834, 2000.

[65] C. J. Palmstrom. *Annu. Rev. Mater. Sci.*, 25:389, 1995.

[66] N. Fletcher and K. W. Lodge. In W. Matthews, editor, *Epitaxial Growth, Part B*, page 529, New York, 1975. Academic.

[67] A. Trampert, F. Schippan, L. Däweritz, and K. H. Ploog. *Appl. Phys. Lett.*, 78: 2461, 2001.

[68] M. Tanaka, J. P. Harbison, and G. M. Rothberg. *J. Cryst. Growth*, 150:1132, 1995.

[69] I. Hernández-Calderón and H. Höchst. *Phys. Rev. B.*, 27:4961, 1983.

[70] W.Braun, H.Möller, and Y. H. Zhang. *J. Vac. Sci. Tech. B*, 16:1507, 1998.

[71] M. Henzler. *Appl. Surf. Sci.*, 11–12:450, 1982.

[72] M. Sauvage-Simkin, R. Pinchaux, J. Massies, P. Claverie, N. Jedrecy, J. Bonnet, and I. K. Robinson. *Phys. Rev. Lett.*, 62:563, 1989.

[73] W. Braun, D. K. Satapathy, and K. H. Ploog. *Surf. Sci.* Accepted.

[74] Jason T. Drotar, T.-M. Lu, and G.-C. Wang. *J. Appl. Phys.*, 96:7071, 2004.

[75] Jason T. Drotar, B. Q. Wei, Y.-P. Zhao, G. Ramanath, P. M. Ajayan, T.-M. Lu, and G.-C. Wang. *Phys. Rev. B*, 64:125417, 2001.

[76] D. K. Satapathy, V. M. Kaganer, B. Jenichen, W. Braun, L. Däweritz, and K. H. Ploog. *Phys. Rev. B*, 72:155303, 2005.

[77] V. M. Kaganer, D. K. Satapathy, W. Braun, B. Jenichen, and K. H. Ploog. unpublished.

[78] M. Kästner, F. Schippan, P. Schützendübe, L. Däweritz, and K. Ploog. *J. Vac. Sci. Technol. B*, 18:2052, 2000.

[79] M. Yakimov, V. Tokranov, G Agnello, and J. van Eisden. *J. Vac. Sci. Tech. B*, 23: 1221, 2005.

[80] L. G. Parratt. *Phys. Rev.*, 95:359, 1954.

[81] M. Born and E. Wolf. *Principles of Optics.* Pergamon, New York, 1980.

[82] B. Jenichen, D. K. Satapathy, W. Braun, V. M. Kaganer, L. Däweritz, and K. H. Ploog. *J. Phys. D: Appl. Phys.*, 38:A169, 2005.

[83] M. Dörfler and K. Bärner. *Phys. Stat. Sol. A*, 17:141, 1973.

[84] J. W. Matthews and A. E. Blakeslee. *J. Cryst. Growth*, 72:118, 1974.

[85] J. W. Matthews. *J. Vac. Sci. Tech. B*, 12:126, 1975.

[86] F. Iikawa, M. J. S. P. Brasil, O. D. D. Couto, C. Adriano, C. Giles, and L. Däweritz. *Appl. Phys. Lett.*, 85:2250, 2004.

[87] F. Schippan, G. Behme, L. Däweritz, K. H. Ploog, B. Dennis, K.-U. Neumann, and K. R. A. Ziebeck. *J. Appl. Phys.*, 88:2766, 2000.

[88] F. Schippan. PhD thesis, Humboldt Universität zu Berlin, 2000.

[89] L. Däweritz, F. Schippan, M. Kästner, B. Jenichen, V. M. Kaganer, K. H. Ploog, B. Dennis, K.-U. Neumann, and K. R. A. Ziebeck. *Inst. Phys. Conf. Ser.*, 170:269, 2002.

[90] J. R. Mohanty. PhD thesis, Humboldt Universität zu Berlin, 2005.

[91] L. Däweritz, M. Kästner, T. Hesjedal, T. Plake, B. Jenichen, and K. H. Ploog. *J. Cryst. Growth*, 251:297, 2003.

[92] W. Friedrich, P. Knipping, and M. Laue. *Annalen der Physik*, 14:971, 1913.

[93] T. C. Huang and Willium Parrish. *Appl. Phys. Lett.*, 27:123, 1975.

[94] R. L Snyder, J. Fiala, and H. J. Bunge. *Defect and Microstructure Analysis by Diffraction.* IUCr Monographs on crystallography 10 (Oxford University Press Inc), New York, 1999.

[95] C. N. J Wagner. In J. B. Cohen and J. B. Hilliard, editors, *Local Atomic Arrangements Studied by X-ray Diffraction*, New York, 1966. Gordon and Breach.

[96] E. J. Mittemeijer and P. Scardi. *Diffraction Analysis of the Microstructure of Materials.* Springer series in materials science (Springer-Verlag), Berlin, Heidelberg, 2004.

[97] G. K. Williamson and W. H. Hall. *Acta Metall.*, 1:22, 1953.

[98] B. E. Warren and B. L. Averbach. *J. Appl. Phys.*, 21:595, 1950.

[99] H. P. Klug and L. E. Alexander. *X-Ray Diffraction Procedures.* John Wiley, New York, 1974.

[100] M. J. Hordon and B. L. Averbach. *Acta Metall.*, 9:237, 1961.

[101] J. E. Ayers. *J. Cryst. Growth*, 135:71, 1994.

[102] T. C. Huang, M. Hart, W. Parrish, and N. Masciocchi. *J. Appl. Phys.*, 61:2813, 1987.

[103] J. I. Langford. In F. H. Chung and D. K. Smith, editors, *Industrial Applications of X-Ray Diffraction*, page 751, New York, 2000. Marcel Dekker Inc.

[104] B. Jenichen, D. Satapathy, W. Braun, L. Däweritz, and K. H. Ploog. *J. Appl. Phys.*, 96:6103, 2004.

[105] V. M. Kaganer, R. Köhler, M. Schmidbauer, R. Optiz, and B. Jenichen. *Phys. Rev. B*, 55:1793, 1997.

[106] D. K. Satapathy, B. Jenichen, V. M. Kaganer, W. Braun, L. Däweritz, and K. H. Ploog. *J. Vac. Sci. Technol. B*, 22:2079, 2004.

[107] A. Trampert. *Physica E*, 13:1119, 2002.

[108] V. Srikant, J. S. Speck, and D. R. Clarke. *J. Appl. Phys.*, 82:4286, 1997.

[109] G. Renaud, A. Barbier, and O. Robach. *Phys. Rev. B*, 60:5872, 1999.

[110] V. M. Kaganer, B. Jenichen, F. Schippan, W. Braun, L. Däweritz, and K. H. Ploog. *Phys. Rev. Lett.*, 85:341, 2000.

[111] B. Jenichen, V. M. Kaganer, F. Schippan, W.Braun, L. Däweritz, and K. H. Ploog. *Mater. Sci. and Eng. B*, 91-92:433, 2002.

[112] Klaus. H. Ploog. *J. Cryst. Growth*, 237–239:2028, 2002.

[113] H. Gleiter. *Mater. Sci. Eng.*, 52:91, 1982.

[114] M.L. Kronberg and F.H. Wilson. *Trans. Am. Inst. Min. Engrs.*, 185:501, 1949.

[115] D. G. Brandon, B. Ralph, S. Ranganathan, and M. S. Wald. *Acta. Metall.*, 12:813, 1964.

[116] W. Bollmann. *Crystal Defects and Crystalline Interfaces.* Springer-Verlag, Berlin, 1970.

[117] H. K. D. H. Bhadeshia. The Institute of Metals, London, 1987. ISBN 0 904357 94 5.

[118] W. T. Read and W. Shockley. *Phys. Rev.*, 78:275, 1950.

[119] D. G. Brandon, B. Ralph, S. Ranganathan, and M. S. Wald. *Acta Metall.*, 12:813, 1964.

[120] A. Trampert and K. H. Ploog. *Cryst. Res. Technol.*, 35:793, 2000.

[121] R. Hull and J. Bean. *Crit. Rev. Solid State Mater. Sci.*, 17:507, 1994.

[122] G. Renaud, P. Guéard, and A. Barbier. *Phys. Rev. B*, 58:7310, 1998.

[123] R. Popescu, H. L. Meyerheim, D. Sander, J. Kirschner, P. Steadmann, O. Robach, and S. Ferrer. *Phys. Rev. B*, 68:155421, 2003.

[124] G. Springholz and K. Wiesauer. *Phys. Rev. Lett.*, 88:015507, 2002.

[125] A. Bourret and P.H. Fuoss. *Appl. Phys. Lett.*, 61:1034, 1992.

[126] A. Yu. Babkevich, R. A. Cowley, N. J. Mason, S. Weller, and A. Stunault. *J. Phys. Condens. Matter*, 14:13505, 2002.

[127] R. Liu and F. A. Ponce. *Appl. Phys. Lett.*, 83:860, 2003.

[128] W. C. Marra, P. Eisenberger, and A. Y. Cho. *J. Appl. Phys.*, 50:6927, 1979.

[129] M. Tanaka. *Physica E*, 2:372, 1998.

[130] J. P. Hirth and J. Lothe. *Theory of Dislocations.* Wiley, New York, 1982.

[131] V. M. Kaganer, B. Jenichen, F. Schippan, W. Braun, L. Däweritz, and K. H. Ploog. *Phys. Rev. B*, 66:045305, 2002.

[132] T. Plake, M. Ramsteiner, V. M. Kaganer, B. Jenichen, M. Kästner, L. Däweritz, and K. H. Ploog. *Appl. Phys. Lett.*, 80:2523, 2002.

[133] L. Däweritz, C. Herrmann, J. Mohanty, T. Hesjedal, K. H. Ploog, E. Bauer, A. Locatelli, S. Cherifi, R. Belkhou, A. Pavlovska, and S. Heun. *J. Vac. Sci. Tech. B*, 23: 1759, 2005.

[134] F. Iikawa, M. Knobel, P. V. Santos, C. Adriano, O. D. D. Couto, M. J. S. P. Brasil, C. Giles, R. Magalhões-Paniago, and L. Däweritz. *Phys. Rev. B*, 71:045319, 2005.

[135] A. Ney, T. Hesjedal, C. Pampuch, A. K. Das, L. Däweritz, R. Koch, and K. H. Ploog. *Phys. Rev. B*, 69:081306, 2004.

[136] B. Jenichen, V. M. Kaganer, C. Herrmann, L. Wan, L. Däweritz, and K. H. Ploog. *Z. Kristallogr.*, 219:201, 2004.

[137] Seshadri Subbanna, Herbert Kröemer, and James L. Merz. *J. Appl. Phys.*, 59(2): 488, 1986.

[138] R. Nötzel, Z. C. Niu, M. Ramsteiner, H.-P. Schönherr, A. Trampert, L. Däweritz, and K. H. Ploog. *Nature*, 392:56, 1998.

[139] W. I. Wang, E. E. Mendez, Y. Iye, B. Lee, M. H. Kim, and G. E. Stillman. *J. Appl. Phys.*, 60(5):1834, 1986.

[140] E. Towe, C. G. Fonstad, H. Q. Le, and J. V. Hryniewicz. *J. Vac. Sci. Technol. B*, 7(2):395, 1989.

[141] P. N. Uppal, J. S. Ahearn, S. P. Svensson, and R. Herring. *J. Cryst. Growth*, 95: 281, 1989.

[142] P. N. Uppal, J. S. Ahearn, and D. P. Musser. *J. Appl. Phys.*, 62(9):3766, 1987.

[143] C. B. Duke, C. Mailhiot, A. Paton, A. Kahn, and K. Stiles. *J. Vac. Sci. Tech. A*, 4 (23):947, 1986.

[144] M. Wassermeier, J. Sudijono, M. D. Johnson, K. T. Leung, B. G. Orr, L. Däweritz, and K. Ploog. *Phys. Rev. B*, 51:14721, 1995.

[145] W. Braun, O. Brandt, M. Wassermeier, L. Däweritz, and K. Ploog. *Appl. Surf. Sci.*, 104–105:35, 1985.

[146] D. K. Satapathy, B. Jenichen, , W. Braun, V. M. Kaganer, L. Däweritz, and K. H. Ploog. *J. Phys. D: Appl. Phys.*, 38:A164, 2005.

[147] R. Nakane, S. Sugahara, and M. Tanaka. *J. Appl. Phys.*, 95:6558, 2004.

Acknowledgments

First of all, I would like to thank God for creating our beautiful world, and for allowing us to explore a small portion of it.

This thesis could not have been performed without the support of many people. I am grateful to those I have worked with and learned from. At this point, I would especially like to thank all of them...

... Prof. Dr. Klaus H. Ploog for giving me a chance to carry out my doctoral research at PDI. Especially, I would like to thank him for giving me the opportunity to attend the conference, and for his comments and suggestions about the manuscript. His continuous support is very much appreciated.

... Prof. Dr. W. T. Masselink and Prof. Dr. A. D. Wieck for taking their time to review this work.

... Dr. Wolfgang Braun for his consistent help, encouragement and excellent guidance throughout the work. I will never forget his support and real-time explanations during the experiments. I have never seen such a person who is so excellent in an area of science and who has such a wonderful personality. Words are not enough to describe his infinite patience, insight, and dedication for work. His tremendous enthusiasm and tenacity are great inspirations of my life.

... Dr. Bernd Jenichen for introducing me to the world of x-ray diffraction. I greatly benefited from his indispensable support. We have spent many late evening measurement shifts together sharing some hot coffee. The freedom I have enjoyed working with him can never be forgotten. He provided a nice example for me both as a good scientist and as a generous person.

... Dr. Vladimir Kaganer for his thoughtful suggestions for understanding the experimental results and many fruitful discussions. He was very supportive through out the work. I will always be impressed by his quick intellect, deep knowledge of physics and humble behavior. Working with him sharing the same office space has been a true pleasure which I will definitely miss.

... Dr. L. Däweritz for all his suggestions, comments and careful reading of the thesis.

... Dr. Brad Tinkham for many late evening discussions and for his comments, and

careful proofreading of the thesis.

... Dr. Xiangxin Guo and Mr. Stefen Behnke for their helps during the experiments at PHARAO beamline.

... Dr. M. Takahasi for reading the thesis and many discussions.

... Dr. Jens Herfort for his help during SQUID measurements.

... Mr. H. P. Schönherr for preparing the cleaving equipment for GaAs (1 1 3) substrate, and many other things.

... Mrs. C. Herrmann for her help in AFM measurements.

... Mrs. I. Schuster for her help with printing the posters.

... Mrs. P. Grasnick for her help in all official matters starting from my arrival until now.

... Mrs. D. Dormeyer, Mrs. S. Räther for their help in getting old articles and books. Both of them were very kind, also in cases where I forget to return the books in time.

... Dr. Denis Kolovos-Vellianitis for his help during the shifting of my apartment.

... All my Ph. D. colleagues for many discussions during the Ph. D. seminars.

Also I want to thank my Indian friends who made my stay in Berlin comfortable and enjoyable. They include: Pranaba K. Muduli, Dr. Jyoti Mohanty, Pranob Misra, Devendra Negi, Dr. A. Das, Prasad Bhalerao, Sharvari B. Dixit, Dr. S. Dhar and family, Bishnubhai and family and Dr. Manoj. K. Mohapatra and family. I wish a good time to all of them.

Finally, I would like to express my deepest gratitude to my parents. Their unfailing love and support have proved valuable all the time during the course of the work. I dedicate this work to them.

Lebenslauf

Name:	Dillip Kumar Satapathy
Geburtstag:	10. Juli 1978
Geburtsort:	Nayagarh, Orissa (Indien)

5.9.2002	Promotionsstudent an der Humboldt-Universität zu Berlin und am Paul-Drude Institut für Festkörperelektronik in der Arbeitsgrupe unter Betreuung von Herrn Prof. Dr. K. H. Ploog
04. – 07.2002	Nuclear Science Center, New Delhi, Indien “Senior Research Fellow", Betreuer: Dr. R. G. Sharma
01.2002	Master of Technology (M. Tech.) Indian Institute of Technology, Delhi, Indien Thema: “Zinc oxide thin films for optoelectronics: Synthesis and characterization”
06.2000 – 12.2001	Studium der Festkörperphysik Indian Institute of Technology, Delhi, Indien
05.2000	Master of Science (M. Sc.) in Physik Utkal University, Orissa, Indien
06.1998 – 04.2000	Studium der Physik Utkal University, Orissa, Indien
05.1997	Bachelor of Science (B. Sc.) Utkal University, Orissa, Indien
03.1994 – 04.1997	Studium der Physik, Chemie und Mathematik Utkal University, Orissa, Indien

Selbständigkeitserklärung

Hiermit erkläre ich, die vorliegende Arbeit selbständig ohne fremde Hilfe verfaßt und nur die angegebene Literatur und Hilfsmittel verwendet zu haben.

Ich habe mich an keiner anderen Universität um einen Doktorsgrad beworben und besitze auch keinen entsprechenden Doktorsgrad.

Ich erkläre die Kenntnis der dem Verfahren zugrunde liegenden Promotionsordnung der Mathematisch-Naturwissenschaftlischen Fakultät I der Humboldt-Universität zu Berlin.

Dillip Kumar Satapathy
29. September 2005